BRNO UNIVERSITY OF TECHNOLOGY

VYSOKÉ UČENÍ TECHNICKÉ V BRNĚ

CENTRAL EUROPEAN INSTITUTE OF TECHNOLOGY BUT

STŘEDOEVROPSKÝ TECHNOLOGICKÝ INSTITUT VUT

FABRICATION AND CHARACTERIZATION OF NANOSTRUCTURES WITH FUNCTIONAL PROPERTIES IN THE FIELD OF PLASMONICS

PŘÍPRAVA A CHARAKTERIZACE NANOSTRUKTUR S FUNKČNÍMI VLASTNOSTMI V OBLASTI PLAZMONIKY

DOCTORAL THESIS
DIZERTAČNÍ PRÁCE

AUTHOR
AUTOR PRÁCE

Ing. Jiří Babocký

SUPERVISOR
ŠKOLITEL

prof. RNDr. Petr Dub, CSc.

BRNO 2020

Summary

This PhD thesis deals with fabrication and characterisation of plasmonic nanostructures. The first part begins with short introduction into plasmonics following with description of methods, that are nowadays used for plasmonic nanostrucuture fabrication and characterisation. The second part of the thesis focusses on experiments, that have been done. The first one explores possibilities for application of variable pressure electron beam lithography for fabrication of plasmonic nanostructures on non-conductive substrates which can be useful for easy prototyping structures for the visible region. The next section discusses some aspects of fabrication of large plasmonic microstructures in the terahertz region using Electron beam lithography. The last part is dedicated to functional properties of plasmonic nanostructures, especially to quantitative characterization of far-field phase induced by plasmonic nanostructures and their applications in the field of optical metasurfaces - artificially designed surfaces, that can be used as planar optical components. The characterization is done using off-axis holographic microscopy. Different experimental approaches with respect to this technique are demonstrated and discussed.

Keywords

Electron beam lithography, EBL, Holographic microscopy, CCHM, plasmonics, metasurfaces, nanoantennas

BABOCKÝ, Jiří. Fabrication and characterization of nanostructures with functional properties in the field of plasmonics . Brno, 2020. Available online: https://www.vutbr.cz/studenti/zav-prace/detail/120597. Doctoral thesis. Brno University of Technology, Central European Institute of Technology BUT. Supervisor of the doctoral thesis Petr Dub.

Abstrakt

Tato dizertční práce se zabývá výrbou a charakterizací plasmonických nanostruktur. Její první část začíná krátkým úvodem do plasmoniky s navazujícím přehledem metod, které jsou v dnešní době nejčastěji používány k výrobě a charakterizaci plasmonických nanostruktur. Druhá část se pak zaměřuje na samotný výzkum, který byl v rámci PhD studia realizován. Cílem prvních experimentů bylo prozkouat možnosti použití elektronové litografie za variabilního tlaku v procesní komoře pro výrobu plasmonických nanostruktur na nevodivých substrátech jako je např. sklo. Jelikož se jedná o materiály, které jsou velice často používány k přípravě plasmonických struktur pacujících v oblasti viditelného světla. Druhá sekce pak diskutuje některé specifické aspekty přípravy plasmonických mikrostruktur elektronovou litografií pro THz oblast. Poslední část se pak zaměřuje na funkční vlastnosti plasmonických nanostruktur, převážně pak na kvantitativní charakterizaci fáze dalekého pole indukovaného plasmonickými nanostrukturami a jejich aplikacemi v oblasti optických metapovrchů - uměle připravených povrchů, které mohou být použity jako planární optické komponenty. Práce demonstruje a diskutuje různé experimentální přístupy použití mimoosové holografické mikroskopie pro jejich charakterizaci.

Klíčová slova

Elektronová litografie, EBL, Holografická mikroskopie, CCHM, plazmonika, metapovrchy, nanoantény

BABOCKÝ, Jiří. Příprava a charakterizace nanostruktur s funkčními vlastnostmi v oblasti plazmoniky . Brno, 2020. Dostupné také z: https://www.vutbr.cz/studenti/zav-prace/detail/120597. Dizertační práce. Vysoké učení technické v Brně, Středoevropský technologický institut VUT, Středoevropský technologický institut VUT. Vedoucí práce Petr Dub.

Prohlašuji, že jsem dizertační práci Příprava a charakterizace nanostruktur s funkčními vlastnostmi v oblasti plazmoniky vypracoval samostatně pod odborným vedením prof. RNDr. Petra Duba, CSc. s použitím materiálů uvedených v seznamu literatury.

V Brně dne 27. 5. 2020 Ing. Jiří Babocký

Acknowledgements

At the beginning I would like to thank to my parents for support during my whole studies.

Another great thanks go to prof. Tomáš Šikola and prof. Petr Dub for development of the great research institute, without which the research like the one presented in this thesis would be impossible. I also thank them for advices and ideas, that emerged into interesting topics covered by this thesis. I also have to thank to my colleagues Miloš Hrabovský and Jakub Sadílek, who helped me and lot of others by establishing state of the art nanofabrication technologies at CEITEC labs. Other thanks go to my colleagues from the plasmonics group, namely to Petr Dvořák for helpful advices with the experimental design and cooperation during measurements, Filip Ligmajer for general advices for the research direction, Martin Hrtoň for theoretical support as his calculations made results presented in this thesis validated against the theory and my bachelor student Petra Binková, who contributed to the fabrication technology development. Special thanks go to my colleagues from the Experimental Biophotonics group led by prof. Radim Chmelík, who is the inventor of the Coherence-controlled holographic microscopy, which is heavily used in this thesis. Among the others, thanks go especially to Aneta Křížová, Lenka Štrbková, Zbyněk Dostál for help with CCHM measurements and to Petr Bouchal for providing an access and help with his Quantitative 4G Optical Microscope. I would also like to thank to Alexander Faßbender from University in Bonn for great collaboration in the field of metasurface research, and further to prof. Jiří Spousta, prof. Petr Dub, Zbyněk Dostál and Petr Dvořák for corrections of the thesis text.

Many thanks go to Tescan Orsay Holding for the financial support during my PhD studies and especially to my Tescan colleagues Jiří Fiala and Jan Bok for great scientific cooperation. I am also grateful to CEITEC Nano for providing access to their nanofabrication facilities and to Alexandra Elbakyan for great contribution to the open science.

Contents

1 Introduction

The interaction of light with matter has been studied from the old ancient ages going back to the Assyrians discovering that specially shaped quartz crystals can influence the light propagation. Together with the basic research, engineering disciplines trying to figure out, how to use these discoveries for construction of several optical devices, have emerged. For many centuries the framework of the classical optics, starting by simple ray optics assumptions slowly evolving into current wave description of the optical phenomena, was developed together with the establishment of traditional optical materials such as glasses or organic polymers. Upon the formation of classical electrodynamic theory, which allows to describe light as an electromagnetic wave, it becomes more and more evident, that light can be manipulated in much more fundamental way than the classical optics with its traditional materials allows. Such assumptions led to design of so called metamaterials – artificially engineered structures that manipulate with electromagnetic waves at the sub-wavelength scale allowing design of components with optical properties unachievable by the conventional optics. Unfortunately, due to limits of fabrication technology, these metasurfaces were for a long time limited to the THz region, where the main discoveries, such as a negative index of refraction, were firstly demonstrated. Luckily, the development of nanotechnologies allowed these principles to be applied to electromagnetic waves with shorter wavelengths approaching the optical frequencies in the recent years.

This PhD thesis focuses on the Plasmonics – a discipline describing the interaction of light with metal-dielectric interfaces and metallic nanoparticles, which nowadays serve as building blocks for metasurfaces in the visible and infrared regions. As first of the plasmonic metasurfaces find slowly their way to the market, two topics are becoming more and more discussed. The first one is precise and reproducible fabrication of plasmonic nanostructures, which must provide reliable and well understood process allowing any particular metasurface to be simply fabricated according to the calculated design. Another area is the development of robust techniques that allow a rapid characterization of the optical performance of fabricated nanostructures.

The thesis is divided into eight chapters. The second chapter provides an overview of the basic theoretical concepts of plasmonics together with brief introduction into applications of plasmonic nanostructures. The next chapter describes currently available fabrication techniques suitable for plasmonic nanostructure prototyping and mass production, trying to identify their main strengths and weaknesses. The fourth chapter provides an overview of available techniques for the plasmonic nanostructure characterization, focusing mainly on characterization of their optical properties. In the second part of the thesis our research that has been done in the field of plasmonic nanostructure fabrication and characterization is presented. It starts with description of some of the common technical problems of the currently used fabrication technology (Electron Beam Lithography) and proposes some solutions. The thesis finishes by characterization of the plasmonic nanostructure phase properties using digital holographic microscopy – a quantitative phase imaging technique, previously used mainly in biological applications – cell dry mass imaging.

2 Plasmonics

As mentioned in chapter 1 plasmonics [1] as a part of the nanophotonics explores the interaction of light with metallic nanostrucutres. As fundamentals of plasmonics are based on the classical theory of electromagnetic fields, optics and light-matter interaction described by the solid state physics, the first sections of this chapter provide overview of basic models describing the optical properties of metals and dielectrics – two main classes of materials, that nowadays form plasmonic devices. The chapter continues by description of the main concepts of plasmonics – surface plasmon polaritons. The chapter finishes by an overview of some industrial applications of plasmonics.

2.1 Optical properties of solids

The optical properties of solids [2] are described by the complex index of refraction $N = n+i\kappa$. The real part n describes the ratio of speed of light in a vacuum c and in a material v

$$n = \frac{c}{v}. \tag{2.1}$$

Differences of the light propagation speed in different materials lead to many effects such as a refraction. The imaginary part κ describes the absorption of light in the material and relates to the absorption coefficient α (with λ being the wavelength of the light)

$$\alpha = \frac{4\pi\kappa}{\lambda} \tag{2.2}$$

known from the Beer absorption law expressing the exponential decrease of the light intensity I when propagating in an absorbing material

$$I(z) = I_0 \mathrm{e}^{-\alpha z}. \tag{2.3}$$

The complex index of refraction is related to the complex dielectric function (relative permittivity) $\varepsilon = \varepsilon_1 + i\varepsilon_2$ by the formula

$$\varepsilon = \sqrt{N} \tag{2.4}$$

leading to

$$\varepsilon_1 = n^2 - \kappa^2, \tag{2.5}$$

$$\varepsilon_2 = 2n\kappa. \tag{2.6}$$

Note that the real and imaginary parts of ε and/or N are connected together by the Kramers-Kronig relations.

2.1.1 Drude model

Drude's free electron model [3] was one of the first models trying to describe properties of metals. In the Drude model it is supposed the electrons move on a positively charged background formed by ion cores. When applying an external electric field $E(t) = E_0 \mathrm{e}^{-i\omega t}$ electron oscillations are governed by the equation of motion

$$m\frac{\mathrm{d}^2x}{\mathrm{d}t^2} + \frac{m}{\tau}\frac{\mathrm{d}x}{\mathrm{d}t} = -eE_0\mathrm{e}^{-i\omega t}. \tag{2.7}$$

The stationary solution reads

$$x(t) = \frac{e}{m\left(\omega^2 + i\omega/\tau\right)}E_0(t), \tag{2.8}$$

where m and e are the mass and charge magnitude of electron, respectively, and τ is the relaxation time. This movement of electrons contributes to the polarization of the material

$$P = -n_\mathrm{e}ex, \tag{2.9}$$

where n_e is the electron concentration. Considering the electric displacement

$$D = \varepsilon_0\varepsilon E = \varepsilon_0 E + P, \tag{2.10}$$

the dielectric function of the Drude metal becomes

$$\varepsilon = 1 - \frac{\omega_\mathrm{p}^2}{\omega^2 + i\omega/\tau} \tag{2.11}$$

with plasma frequency

$$\omega_\mathrm{p} = \sqrt{\frac{n_\mathrm{e}e^2}{\varepsilon_0 m_0}}. \tag{2.12}$$

2.1.2 Lorentz model

For description of dielectrics many different models have been presented. First models (Cauchy's or its improved variant - Sellmier's model [4]) were empirical without any efforts to describe dielectrics by their structure. These models are valid in the visible region and are nowadays still used in conventional optics, but for applications in electrodynamics and plasmonics more robust models are needed. The Lorentz model [5] describes the dielectric in similar way as Drude's one describes metals. The main difference is that the electrons in dielectrics are bound to their corresponding ion cores by retractive force, as if they were stitched together using springs (note that this also applies to real metals at higher energies due to interband transitions). Thus we have to supplement eq. 2.7 with this retractive force

$$m\frac{\mathrm{d}^2x}{\mathrm{d}t^2} + \frac{m}{\tau}\frac{\mathrm{d}x}{\mathrm{d}t} + m\omega_0^2 x = -eE_0\mathrm{e}^{-i\omega t}, \tag{2.13}$$

where ω_0 corresponds to the eigen-frequency of the oscillator and in case of the spring model would be $\omega_0 = \sqrt{k/m}$ with the spring stiffness constant k. Using similar mathematics as in the Drude model, we can easily derive the dielectric function of a dielectric material as

$$\varepsilon = 1 - \sum_{j=0}^{N} \frac{f_j\omega_j^2}{(\omega^2 - \omega_j^2) + i\omega/\tau_j} \tag{2.14}$$

2.2 Surface plasmons-polaritons (SPP)

Surface plasmon polaritons [1] are evanescent electromagnetic waves propagating along the metal-dielectric interface. As the electromagnetic waves are governed by Maxwell's equations, let the description of surface plasmon polaritons begin there.

Maxwell's equations describe the relation between dielectric displacement $\overrightarrow{D}$, magnetic induction $\overrightarrow{B}$, electric field $\overrightarrow{E}$ and magnetic field $\overrightarrow{H}$

$$\nabla \cdot \overrightarrow{D} = \rho_{\mathrm{ext}}, \tag{2.15}$$

$$\nabla \cdot \overrightarrow{B} = 0, \tag{2.16}$$

$$\nabla \times \overrightarrow{E} = -\frac{\partial \overrightarrow{B}}{\partial t}, \tag{2.17}$$

$$\nabla \times \overrightarrow{H} = \vec{J}_{\mathrm{ext}} + \frac{\partial \overrightarrow{D}}{\partial t}, \tag{2.18}$$

with ρ_{ext} representing the external charges and $\vec{J}_{\mathrm{ext}}$ representing the external current densities. For the field inside matter two other relations hold

$$\overrightarrow{D} = \varepsilon_0\overrightarrow{E} + \vec{P}, \tag{2.19}$$

$$\overrightarrow{H} = \frac{1}{\mu_0}\overrightarrow{B} - \overrightarrow{M}, \tag{2.20}$$

where $\vec{P}$ and $\overrightarrow{M}$ are polarization and magnetization of the material, respectively, ε_0 and μ_0 are the permittivity and permeability of vacuum, respectively.

In order to make the description complete, fields at material boundaries must comply with the following continuity conditions

$$\vec{n} \times \left(\overrightarrow{E}_2 - \overrightarrow{E}_1\right) = 0, \tag{2.21}$$

$$\left(\overrightarrow{D}_2 - \overrightarrow{D}_1\right) \cdot \vec{n} = \sigma_{\mathrm{s}}, \tag{2.22}$$

$$\left(\overrightarrow{B}_2 - \overrightarrow{B}_1\right) \cdot \vec{n} = 0, \tag{2.23}$$

$$\vec{n} \times (H_2 - H_1) = \vec{j}_\mathrm{s}, \tag{2.24}$$

where $\vec{n}$ is the normal vector pointing from from the domain 1 to the domain 2, σ_s is the surface charge between areas and $\vec{j}_\mathrm{s}$ is the surface current density between domains.

Assuming no external charges or currents, Maxwell's equations yield wave equations

$$\nabla^2 \overrightarrow{E} - \frac{\varepsilon}{c^2} \frac{\partial^2 \overrightarrow{E}}{\partial t^2} = 0, \tag{2.25}$$

$$\nabla^2 \overrightarrow{H} - \frac{\varepsilon}{c^2} \frac{\partial^2 \overrightarrow{H}}{\partial t^2} = 0, \tag{2.26}$$

with $c = 1/\sqrt{\varepsilon_0 \mu_0}$ being the speed of light. For harmonic time dependent fields ($\overrightarrow{E}(t), \overrightarrow{H}(t) \propto \mathrm{e}^{-\mathrm{i}\omega\mathrm{t}}$), the wave equation can be rewritten in the form of the Helmholtz equations

$$\nabla^2 \overrightarrow{E} + \varepsilon \frac{\omega^2}{c^2} \overrightarrow{E} = 0, \tag{2.27}$$

$$\nabla^2 \overrightarrow{H} + \varepsilon \frac{\omega^2}{c^2} \overrightarrow{H} = 0. \tag{2.28}$$

As mentioned earlier, plasmons are evanescent waves propagating along the metal-dielectric interface. Thus using the geometry shown in fig. 2.1, the fields of the plasmon waves in a dielectric and metal read

$$\overrightarrow{E}_\mathrm{d} = \overrightarrow{E}_{\mathrm{d}0} \mathrm{e}^{-ik_\mathrm{d} z} \mathrm{e}^{i\beta x} \tag{2.29}$$

$$\overrightarrow{H}_\mathrm{d} = \overrightarrow{H}_{\mathrm{d}0} \mathrm{e}^{-ik_\mathrm{d} z} \mathrm{e}^{i\beta x} \tag{2.30}$$

for $z > 0$ (the dielectric region) and

$$\overrightarrow{E}_\mathrm{m} = \overrightarrow{E}_{\mathrm{m}0} \mathrm{e}^{k_\mathrm{m} z} \mathrm{e}^{i\beta x} \tag{2.31}$$

$$\overrightarrow{H}_\mathrm{m} = \overrightarrow{H}_{\mathrm{m}0} \mathrm{e}^{ik_\mathrm{m} z} \mathrm{e}^{i\beta x} \tag{2.32}$$

for $z < 0$ (the metallic region). Here the propagation constant $\beta = k_x$ denotes the wave vector component in the propagation direction, k_m and k_d describe the evanescent nature of the fields.

Inserting eq. 2.29 – 2.32 into the Helmholtz equations 2.27 and 2.28, we obtain $k_\mathrm{d} = \sqrt{\beta^2 - \varepsilon_\mathrm{d}(\omega/c)^2}$ and $k_\mathrm{m} = \sqrt{\beta^2 - \varepsilon_\mathrm{m}(\omega/c)^2}$. Note that $\delta_\mathrm{d} = 1/k_\mathrm{d}$ and $\delta_\mathrm{m} = 1/k_\mathrm{m}$ is the penetration depth into dielectric and metal, respectively.

After applying the boundary conditions 2.21 – 2.24, we find finally, that there exists only TM polarized surface plasmons in the frequency region, where the real part of the dielectric function of the metal is negative. The magnetic field of the TM modes reads

$$H_y(x,z) = \begin{cases} A\mathrm{e}^{-k_\mathrm{d} z} \mathrm{e}^{i\beta x}, & z > 0 \\ A\mathrm{e}^{k_\mathrm{m} z} \mathrm{e}^{i\beta x}, & z < 0 \end{cases} \tag{2.33}$$

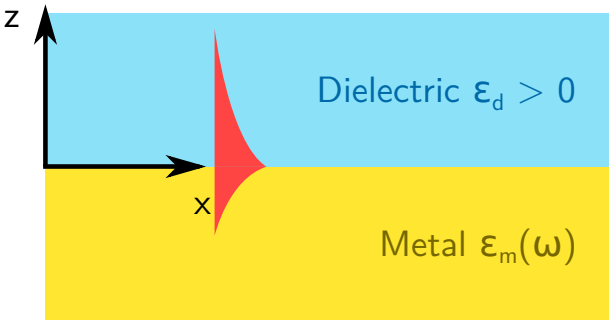

Figure 2.1 Surface plasmon polaritnos at a metal-dielectric interface, adapted from [1]

with

$$\beta = \frac{\omega}{c}\sqrt{\frac{\varepsilon_d \varepsilon_m}{\varepsilon_d + \varepsilon_m}}. \tag{2.34}$$

Supposing the dielectric function of the dielectric being real, the real and imaginary parts of the propagation constant β read, respectively [6]

$$\mathrm{Re}\left[\beta\right] = \frac{\omega}{c}\sqrt{\frac{\varepsilon_d \mathrm{Re}\left[\varepsilon_m\right]}{\varepsilon_d + \mathrm{Re}\left[\varepsilon_m\right]}}, \tag{2.35}$$

$$\mathrm{Im}\left[\beta\right] = \frac{\omega}{c}\frac{\mathrm{Im}\left[\varepsilon_m\right]}{2\left(\mathrm{Re}\left[\varepsilon_m\right]\right)^2}\left(\frac{\mathrm{Re}\left[\varepsilon_m\right]\varepsilon_d}{\mathrm{Re}\left[\varepsilon_m\right] + \varepsilon_d}\right). \tag{2.36}$$

Considering $\mathrm{Re}\left[\varepsilon_m\right] < 0$ and eq. 2.35 we can see, that $\mathrm{Re}\left[\varepsilon_m\right] \leftarrow \varepsilon_d$ must hold. The real part of β determines the SPP wavelength $\lambda_{SPP} = 2\pi/\mathrm{Re}\left[\beta\right]$ and the imaginary part of β determines the propagation length δ_{SPP}, i.e. the distance over which the power of the SPP falls to $1/e$ of the initial value, $\delta_{SPP} = 1/2\mathrm{Im}\left[\beta\right]$.

When we examine the dispersion relation of SPP (fig. 2.2) in a little bit more detail, we can find out, that SPPs cannot be simply excited by illumination as when we will match the energy of the plasmon with energy of light, their momentum will mismatch making it impossible to satisfy the momentum conservation law. In order to excite SPP, special k matching techniques such as total internal refraction developed by Otto [7] or Kretschman [8] has to be employed. Another possibility is the use of broken symmetry such as gratings in the metallic layer or by approaching the probe of Scanning Near-field Optical Microscope towards the interface.

2.3 Localized surface plasmon-polaritons (LSPP)

While the description of plasmons propagating along an infinite metal-dielectric surface is easy to understand, more interesting effects with many possible engineering applications can be obtained, when this interface is nanostructured - plasmons are excited in small nanoparticles with dimensions comparable to the plasmon wavelength [9]. These plasmons

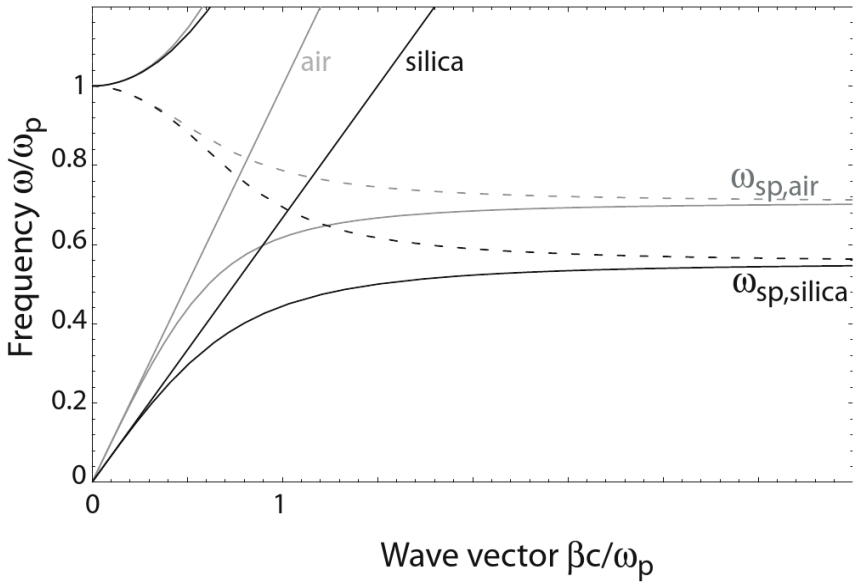

Figure 2.2 Dispersion of surface plasmon polariton at an interface of Drude metal with negligible losses and air (gray) or silica (black), the solid lines display the real part, the dashed lines the imaginary part, adapted from [1]

are called localised surface plasmon-polaritons(LSPP) or more often localised surface plasmons (LSP). Several models describing the nanoparticle response were invented in the past. The following sub-sections will briefly comment on two of them - a quasi-static approximation model suitable for small nanoparticles and Fabry-Pérot model, which can explain the size-dependent properties. Nowadays for description of complex systems such as dimer antennas, or plasmonic metamaterials, numeric solutions of Maxwell equations using a finite-difference time-domain method or a boundary-element method are needed in order to fully understand its behaviour.

2.3.1 Quasi-static approximation

When the dimensions of nanoparticle are smaller than the wavelength of the driving fields (for the visible range typically ~30 nm), the phase variation of the field across the nanoparticle volume can be neglected. The external wave can be approximated by a static field. Thus when a small sphere is placed into an electric field (see fig. 2.3), the Laplace equation ($\nabla^2\Phi = 0$) in spherical coordinates with associated boundary conditions is to be solved. Field potentials inside and outside the particle then read

$$\Phi_{\mathrm{m}} = -\frac{3\varepsilon_{\mathrm{d}}}{\varepsilon_{\mathrm{m}} + 2\varepsilon_{\mathrm{d}}} E_0 r \cos\theta, \tag{2.37}$$

$$\Phi_{\mathrm{d}} = -E_0 r \cos\theta + \frac{\varepsilon_{\mathrm{m}} - \varepsilon_{\mathrm{d}}}{\varepsilon_{\mathrm{m}} + 2\varepsilon_{\mathrm{d}}} E_0 a^3 \frac{\cos\theta}{r^2}. \tag{2.38}$$

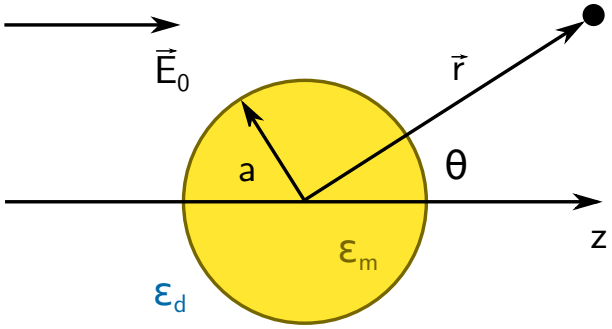

Figure 2.3 Metallic nanosphere in the quasi-static approximation, ε_m represents the dielectric function inside the metallic sphere, ε_d represents the dielectric function of the surrounding dielectric, adapted from [1]

The second term on the right hand side of eq. 2.38 describing the electric potential of an electric dipole may be expressed in the form

$$\frac{\vec{p}\cdot\vec{r}}{4\pi\varepsilon_0\varepsilon_\mathrm{d}r^3}, \tag{2.39}$$

where the dipole moment

$$\vec{p} = \varepsilon_0\varepsilon_\mathrm{d}\alpha\vec{E_0} \tag{2.40}$$

being induced by the incident field $\vec{E_0}$ is expressed by the polarizability of the nanoparticle

$$\alpha = 4\pi a^3\frac{\varepsilon_\mathrm{m}-\varepsilon_\mathrm{d}}{\varepsilon_\mathrm{m}+2\varepsilon_\mathrm{d}}. \tag{2.41}$$

We can see, that for $\mathrm{Re_m}\left[\varepsilon\right] = -2\varepsilon_\mathrm{d}$ the polarizability experiences a resonant enhancement (Fröhlich condition [10]). The mode associated with such a condition is called dipole localised surface plasmon-polariton.

To conclude, the quasi-static approximation model shows that localised SPPs can be excited by simple illumination at sub-wavelength nanoparticles with resonant frequency independent on their size, but depending on optical properties of metal and surrounding dielectrics. In order to include size effects that arise at larger particles, an exact theory developed by Gustav Mie [11] has to be employed.

2.3.2 Fabry-Pérot model

The Fabry-Pérot model [12] describes localised plasmon polariton on infinitely thin nanowire and it presents a very easy model, which can give a basic insight to different mode formation and size effects. Let's assume this nanowire made of metal. As such a nanowire may be described as an interface between metal and dielectric, according to the theory described in section 2.2, it supports the propagation of surface plasmon polariton waves. On the other hand, the limited length of the wire L_res makes it a perfect resonator cavity, meaning that the Fabry-Pérot like resonance can happen with simple resonance condition

$$\beta L_{\mathrm{res}} = n\pi, \tag{2.42}$$

where β corresponds to the plasmon propagation constant defined by eq. 2.34, and $n = 1, 2, ...$ is the resonance order. Due to electric poles at nanowire open ends at optical frequencies the field extends outside the antenna which causes the phase shift Φ_{R} at the reflection, turning the resonance condition into

$$\beta L_{\mathrm{res}} + \Phi_{\mathrm{R}} = n\pi. \tag{2.43}$$

for the dipole mode ($n = 1$) the nanowire acts as a radiating dipole.

2.3.3 Optical properties of plasmonic nanostructures

When plasmonic nanostructures are illuminated in the frequency region of their resonance wavelength, several effects can be observed. The incident irradiation is transferred into a localised surface plasmon excited in the nanostructures which leads to a significant dip in the transmittance spectrum at the resonant wavelength. As the excited LSPP are relaxed, the energy is re-radiated back into the free space enhancing the scattering. In order to quantify these effects, effective cross sections of absorption C_{abs} and scattering C_{sca} can be defined

$$C_{\mathrm{abs}} = \frac{P_{\mathrm{abs}}}{I}, \tag{2.44}$$

$$C_{\mathrm{sca}} = \frac{P_{\mathrm{sca}}}{I}, \tag{2.45}$$

where I represents the incident intensity, and P_{abs} and/or P_{sca} represent the intensity absorbed and/or scattered by the nanostructure. For nanostructures described by a quasi-static approximation, these cross sections can be expressed by polarizability [13]

$$C_{\mathrm{abs}} = k\mathrm{Im}\left[\alpha\right] = 4\pi k a^3 \mathrm{Im}\left[\frac{\varepsilon_{\mathrm{m}} - \varepsilon_{\mathrm{d}}}{\varepsilon_{\mathrm{m}} + 2\varepsilon_{\mathrm{d}}}\right], \tag{2.46}$$

$$C_{\mathrm{sca}} = \frac{k^4}{6\pi}\left|\alpha\right|^2 = \frac{8\pi}{3} k^4 a^6 \left|\frac{\varepsilon_{\mathrm{m}} - \varepsilon_{\mathrm{d}}}{\varepsilon_{\mathrm{m}} + 2\varepsilon_{\mathrm{d}}}\right|^2. \tag{2.47}$$

For complex structures the cross-sections have to be calculated numerically.

As engineered plasmonic nanostructures are capable of transforming electromagnetic fields, these nanostructures are often called nanoantennas [14].

2.4 Applications of plasmonic nanoantennas

As mentioned in Chapter 1 the plasmonic effects are nowadays investigated for their possible use for many applications in the field of nanophotonics and optics. This section summarizes three main industrial applications, that have been presented so far – (i) structural

colouring for anticonterfeit applications and data storage, (ii) optical metasurfaces, and (iii) sensing.

2.4.1 Structural colouring

The capability of plasmonic nanoantennas to scatter specific wavelengths of the incident light allows plasmonic nanoantennas to be used for surface colouring [15]. One of the largest advantages is unprecedented spatial resolution, with prints at ~10 000 DPI already demonstrated [16]. As such a resolution lies bellow the diffraction limit, such prints can be used as security elements for anticounterfeit protection of sensitive documents or high density optical information storage.

Most of these applications are nowadays based on two different geometries (see fig. 2.4). In the first case, hydrogen silsesquioxane pillars are fabricated on a silicon substrate using electron beam lithography. In the next step the whole sample is coated by a metal layer (usually aluminium), which produces small metallic nanoparticles on top of the pillars, while making a homogeneous mirror like layer in between these pillars [17]. The second approach utilizes a nanogap structure, where the selected substrate is firstly coated by an aluminium layer, followed by a thin transparent spacer (usually Al_2O_3). Plasmonic nanoparticles are then built on top of this spacer making a metal-insulator-metal (MIM) stack further enhancing the plasmonic effect [18].

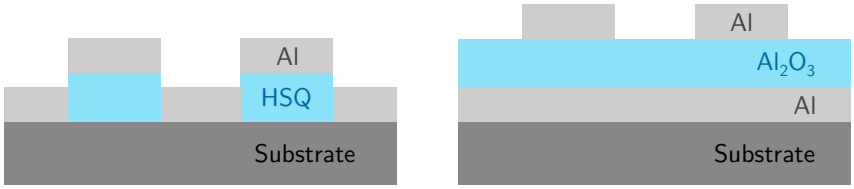

Figure 2.4 Plasmonic nanostructures for surface colouring, left: HSQ based setup, right: nanogap based setup

The lateral geometry of such surfaces usually consists of arrays composed of disc structures with the disc diameter as the main parameter for colour control and the spacing for fine tuning. Recently, the concept of mixed pixels has been introduced, where discs of different dimensions are combined in order to further extend available palette (see fig. 2.5).

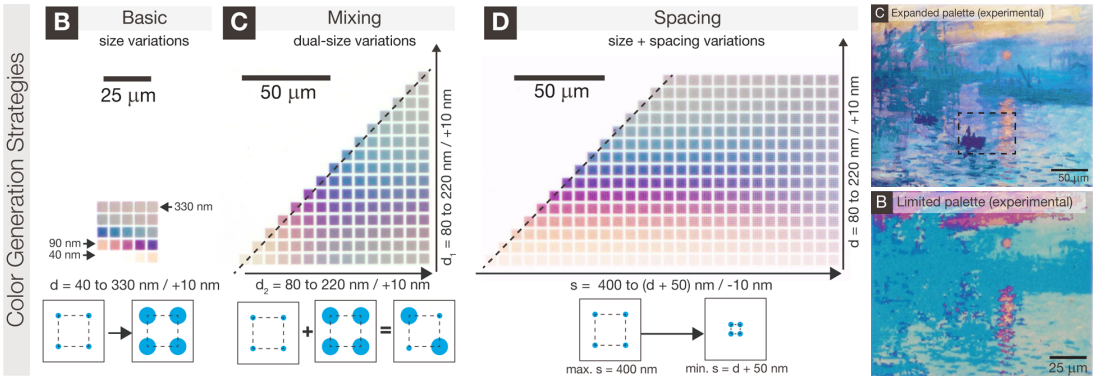

Figure 2.5 Different palette strategies for plasmonic structural colouring, adapted from [17]

Recent research in the structural colouring focuses on fabrication process scalability [19] and integration with current Optically variable device (OVD) systems and tunable systems, where the colour effects can be altered after the fabrication [20].

2.4.2 Plasmonic metasurfaces for light control

Plasmonic nanoparticles (nanoantennas) nowadays find their place in the field of metasurfaces [21,22] - engineered optically active surfaces for light manipulation at the nanoscale meant to be used as flat optical components with unique properties not achievable by conventional optical elements (often called the fourth generation optics).

Most of nowadays metasurfaces are based on manipulation of the light amplitude and phase at every point of the surface by plasmonic based meta-blocks or meta-atom with precisely tailored optical response. Several different principles/geometries have been proposed in the past. These approaches for instance include V-shaped nanoantennas supporting two resonant modes. Hybridization of these modes lead to two polarization states in the scattered radiation influencing the phase of transmitted light. The main advantage of such a geometry is its independence on light polarization, unfortunately its efficiency is limited. Another wide spread structure is based on the geometrical phase (Pancharatnam-Berry phase), where the phase of circularly polarized light can be controlled just by the orientation of individual nanoantennas.

Examples of demonstrated metasurfaces (see fig. 2.6) include aberration-corrected lenses, axicons [23], quater-wave plates [24], negative refractive index metasurfaces [25,26], metasurfaces for orthogonal polarization separation, meta-holograms, and others. Recent research in metasurfaces also focuses on tunable metamaterials that can be dynamically reconfigured.

2.4.3 Sensing

The plasmonics as part of the nanophotonics has been explored by biologists and biochemists right from the beginning for possible applications in the field of sensing or bio imaging [28]. The oldest sensing approach – a surface plasmon resonance [29] sensor is nowadays routinely used in many biological labs for daily analytical work. The sensor is based on the necessity of k-matching for the surface plasmon polariton excitation at a metal-dielectric surface. A thin film of metal (typically gold) is deposited on top of a glass prism (see fig. 2.7). When the prism is illuminated from bottom under different angles, at some angle θ ('resonance angle' in the biological terms) the k condition for plasmon excitation is fulfilled leading to excitation of SPPs in the metallic layer. The excitation of SPP leads to a significant drop in the reflected light. As the SPP wavelength strongly depends on the refractive index of the medium surrounding the metallic film, this angle is basically a function of the refractive index of the medium surrounding the metallic layer. Thus, when some probed analyte is placed on top of the layer, its refractive index can be precisely measured and its changes due to some biochemical reactions detected.

Localised surface plasmon polaritons bound to small metallic nanoparticles are on the other hand still finding its way into biological applications. They have been already applied as optically active labels for immunoassays [30] or as markers for sub-wavelength bio

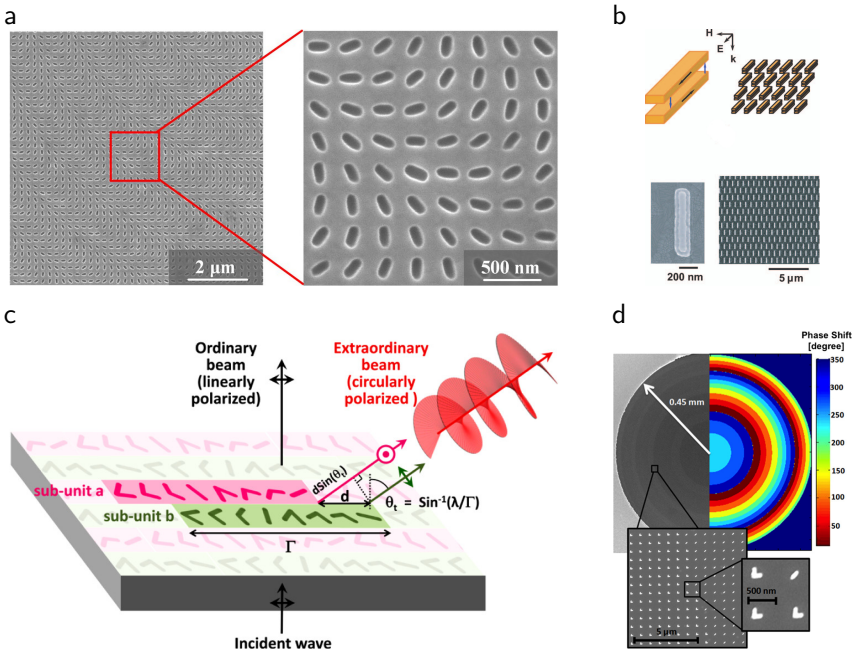

Figure 2.6 Plasmonic metasurfaces - (a) metasurface for vortex beam generation [27], (b) negative refractive index metasurface [26], (c) quarter wave plate [24], (d) meta lens [23]

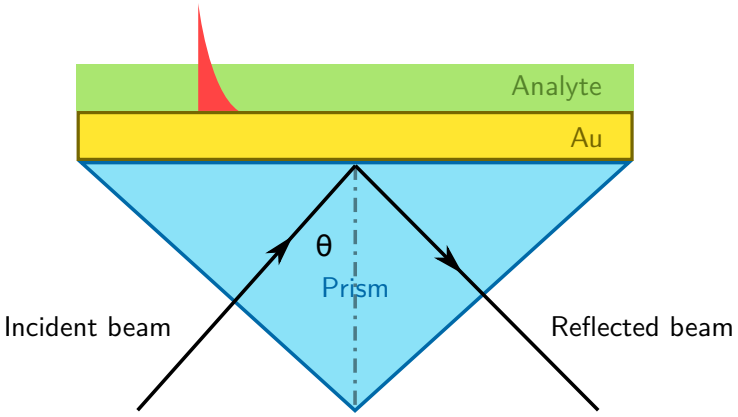

Figure 2.7 Surface plasmon resonance sensor

imaging replacing commonly used flurophores [31] which suffer from bleaching effects. The ability of plasmonic nanoparticles to enhance the near field has also been used to enhance signal in micro-optical spectroscopies, such as surface-enhanced Raman Spectroscopy [32], Surface-Enhanced Infrared Absorption Spectroscopy or fluorescence measurements [33].

Recently, the localised surface plasmon-polaritons on metallic nanoparticles have been proposed as a tool for sensing itself as their resonance wavelength depends on the index of refraction of surrounding medium. At such a configuration the spectrum of light transmitted through an array of plasmonic nanoantennas is measured and shifts in the resonance wavelength are observed [34]. The main advantage of such an approach is possibility of integration of such sensors in micro-fluidic systems allowing multi-channel simultaneous analysis on one chip [35], speeding up the process. Phase-resolved measurements were

also proposed [36] as the phase sensitivity to the index of refraction is usually stronger than the amplitude sensitivity.

3 Methods for plasmonic nanostructures fabrication

Fabrication of plasmonic nanostructures (nanoantennas) is based on methods common in fabrication of other types of nanostructures. Nowadays two approaches are typically used: lithographic fabrication and self-assembly processes. The lithographic fabrication (originally used in semiconductor industry) allows direct control of every single plasmonic nanoparticle position and shape. The main drawback of this approach is its limited scalability, where the datafile describing large structures can grow into big sizes. On the other hand, the fabrication based on self-assembly processes provides usually very good process scalability, but the control of shapes and positions of fabricated structures is limited and controlled semi-stochastically by process parameters only. One of the recent trends in plasmonic nanostructure fabrication consists of combination of both approaches, where the substrate is pre-patterned using lithographic techniques at low resolution in order to locally influence and control subsequent self-assembly processes allowing precise control of critical parameters while taking the advantage of scalability of self-assembly processes [37].

Lithographic approaches can be further divided into methods suitable for plasmonic nanostructures prototyping where the lithographic device writes the structures directly according to the digital description of the pattern (such as Electron Beam Lithography, fabrication using Focused Ion Beams or SPM based methods) and methods for massive nanostructure replication at industrial scales (Nanoimprint Lithography, Extreme Ultraviolet Lithography). This approach usually involves some kind of mask fabricated by a prototyping method, that can be replicated at high throughputs.

As the lithographic fabrication of plasmonic nanostructures typically involves nanostructuring of a metallic layer on a suitable substrate, there are two main methods: depositing metal through a nanostructured mask or sputtering a metallic layer through this mask.

Both processes begin with substrate preparation – a cleaning procedure followed by deposition of auxiliary layers when needed (these can include metallic reflectors, spacers, electrodes, etc.). When the substrate is prepared, it is usually pre-dieced by a laser cutter in order to allow easier separation of chips at the end of the fabrication process. Next steps differ according to the selected method.

When using the first method (see fig. 3.1 left), the fabrication follows with deposition of a polymeric resist layer, that would act as a mask for the deposition process. The layer is then patterned by some lithographic method, exposing the substrate only at desired places. The pattern transfer step involves deposition of a metallic layer on top of the mask and the 'lift-off' process dissolving the mask leaving the metal only at places, where the deposition was directly done at the substrate.

In contrast when using the second method (see fig. 3.1 right), the cleaning is firstly followed by deposition of a desired metallic layer and the polymeric resist layer is deposited on top of it. After the resist is patterned using some lithographic technique, it serves

as a mask for sputtering/etching process where it protects fabricated structures, while the metal is removed from the rest of the substrate. After the sputtering process, the residuals of the mask are removed by some selective etch cleaning.

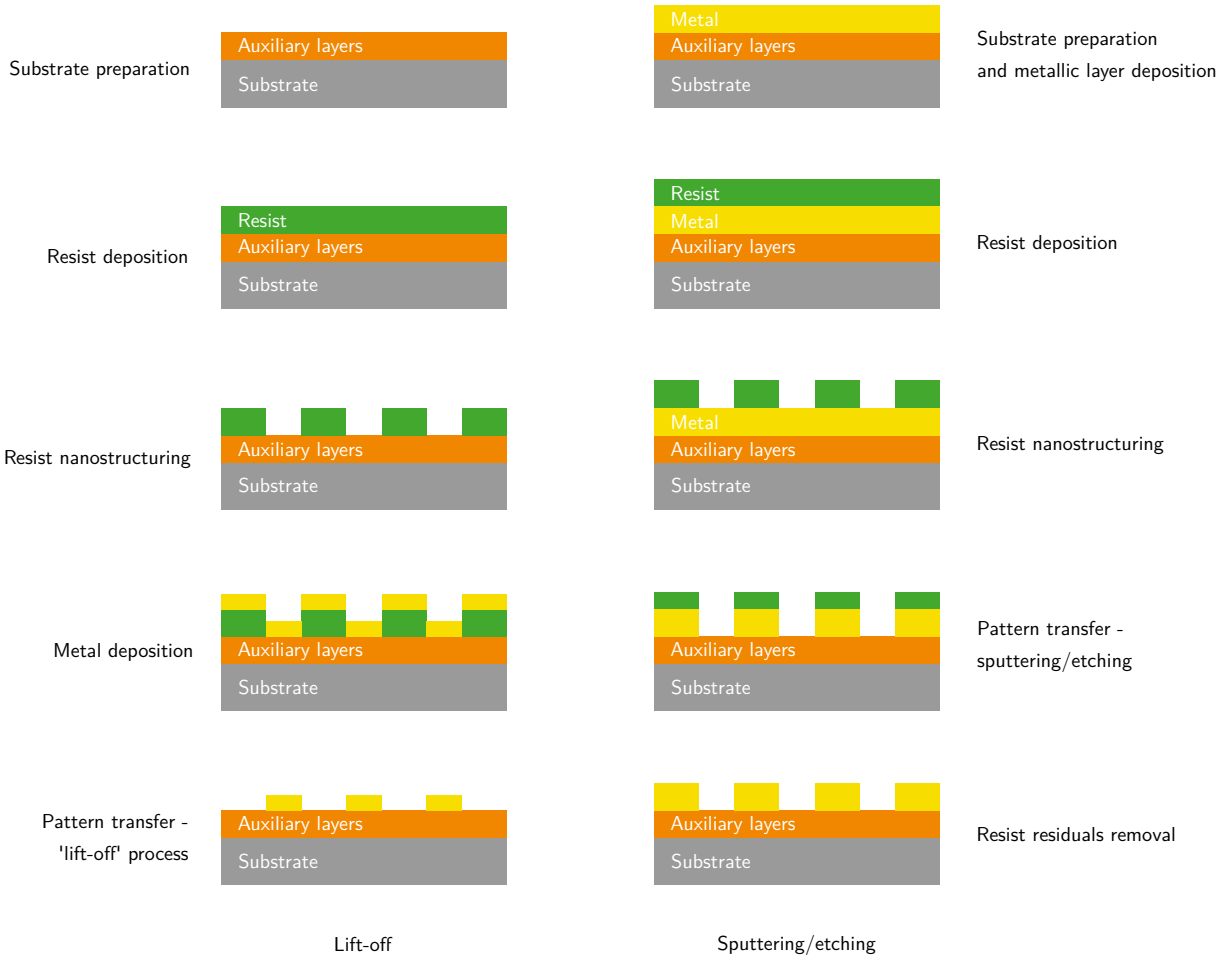

Figure 3.1 Lithographic methods

In reality, technical limitations of the lithographic methods and used materials often require combination of both methods, where for example the 'lift-off' process is used as a first step for fabrication of some kind of metallic or nitridic 'hard mask', that serves as a mask for the sputtering process. Such complex workflows often involve deposition of auxiliary layers, that can be selectively etched in order to remove the residuals of the mask while leaving the fabricated nanostructures untouched.

The following sections describe lithographic methods used for mask patterning, followed by methods used for metal deposition.

3.1 Electron Beam Lithography

Electron Beam Lithography (EBL) presents nowadays the state-of-the-art method for lithographic fabrication of various kinds of nanostructures. The main principle of EBL is modification of the resist layer by electron beam, which results in cutting polymer chains

into smaller fragments or polymer chain cross-linking that influence the solubility of the polymer layer in solvents (usually called developers).

3.1.1 Design data formats for EBL

Unlike the traditional optical UV lithography, which uses masks with defined structures, the EBL process is based on the direct nanostructure writing using the deflection system of EBL writer making the design definition in a purely digital form. Most of formats used nowadays are based on the principle of hierarchical database of graphical shapes, where complex structures are composed of arrays of simpler ones. The oldest format used for data storage is GDSII [38]. Even it was primarily designed for use with magnetic tapes, it is still de facto an industrial standard for electron beam lithography. The largest drawback of this format is its stream nature requiring software to completely parse the whole input file. Another drawback comes from the fact that many EBL processes need to store additional information. Unfortunately, EBL system manufacturers often ignore the standard way of user data storage (PROPATTR records) and are storing custom data in way that breaks the binary structure of the GDSII file. Together with missing documentation of such extensions, this leads to many problems of data inter portability where the design created for one EBL system cannot be simply loaded by another one. Another format is Caltec Intermediate Form [39]. Unlike the GDSII it stores all the data in the text form. These features make it very flexible an easily human readable. The main drawback is a quite large file size when compared to other alternatives due to the ineffectiveness of data representation in the text form. The newest format is the Open Artwork System Interchange Standard (OASIS) [40] developed by the SEMI standards consortium as a successor of GDSII. It offers very effective data storage suitable for very large designs [41], almost unlimited precision and possibility to store user data for each defined geometrical shape. OASIS format also provides indexes that can be used for quick seeking in the input file and embedded data compression reducing the output file size. Some special applications (typically optically variable devices) are often defined using bitmap formats, where each pixel represents a square element of the resulting pattern. Patterning of such data often requires conversion or special patterning strategies. There are also other mostly proprietary formats developed by EBL equipment manufacturers as the Tescan DrawBeam project file, Raith CSF format, etc. Fig. 3.2 shows typical workflow in GDSII designer with a database hierarchical structure shown in the left panel.

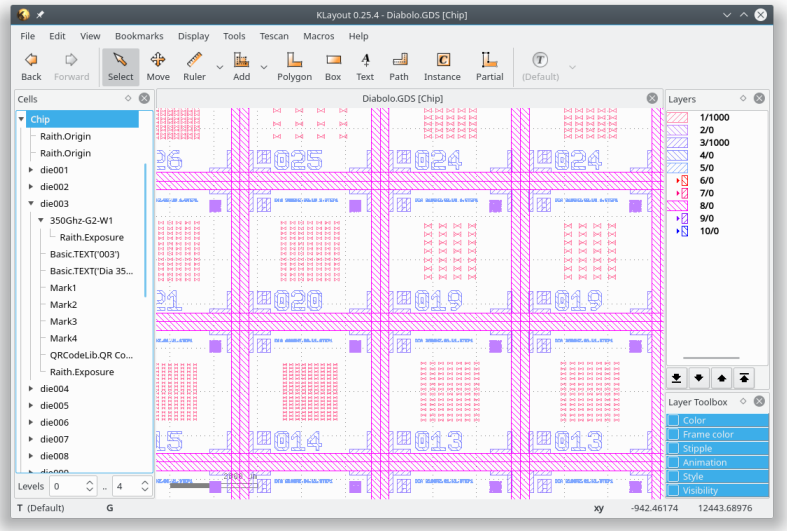

Figure 3.2 GDSII design being edited using KLayout [42] software

3.1.2 Resists for EBL

Resist materials are nowadays based usually on various polymers with different properties. Selection of the right resist is a crucial decision, that determines the properties of the fabricated structures and possible pattern transfer techniques. Electron beam resists can be divided into two main categories – positive and negative. For positive resists the exposure using electron beam causes scission events in the polymer chain enhancing the solubility of exposed areas in some solvents – resist developers. On the other hand, for negative resists, the exposure by electron beam usually initiate cross-linking reactions in the polymer making the exposed areas less soluble in the selected developer.

The selected resist/development process combination can be characterised by two main parameters – critical exposure dose (often called sensitivity) and resist contrast. The critical dose is deposited charge density (usually defined in $\mu C/cm^2$), that is necessary to fully cross-link (or remove) the resist in the exposed area. The contrast specifies the slope between the dose that leaves the resist untouched and critical dose. More specifically, the contrast is usually defined as

$$c = \left(\log_{10} \frac{D_2}{D_1} \right)^{-1} \tag{3.1}$$

where D_2 is the minimal dose, which causes complete exposure of the resist layer, and D_1 is the maximal dose, which leaves the resist unexposed [43].

Process parameters such as the dose generally depend on the processing conditions that influence the dynamics of exposure and development processes. For example, the cross-section of inelastic collisions of the electron beam decreases with the increasing beam energy, which leads to a decrease of the resist sensitivity. In case of the PMMA resist, the critical dose for 30 keV beam is three times higher than for 10 keV beam. Another important process condition is the development temperature because the dissolution of

the resist can be represented as a kinetic diffusion-like process. M.A. Mohammad et al. has shown that the temperature dependence of the applicable dose window described by (D_{min}, D_{max}) can be simply defined by [44]

$$D\left(T\right)_{\mathrm{min,max}} = D^{\mathrm{ref}}_{\mathrm{min,max}} \exp\left(-\frac{U}{\alpha k}\left(\frac{1}{T} - \frac{1}{T^{\mathrm{ref}}}\right)\right) \tag{3.2}$$

where $D^{\mathrm{ref}}_{\mathrm{min,max}}$ are the experimentally obtained doses for temperature T^{ref}, U is the activation energy and α is the power of medium. The development temperature T also influences the process contrast, which is often used in cold development recipes, where decreasing of the development temperature increases the process contrast [45,46].

The resist contrast and sensitivity also depend on developer handling during development. Landobasa et al. showed [46], that developer sonification during development increases the process contrast as the sonification allows also larger fragments of the resist to be removed and prevents their redeposition.

The oldest and still the most popular resist nowadays is Poly(methyl-methacrylate) (PMMA). PMMA is basically a positive resist, but its use as a negative resist has been also demonstrated [47]. PMMA resist is available in different molecular weights (different chain lengths). PMMA with longer polymer chains has usually lower sensitivity, but higher contrast. PMMA is usually developed by solution of Methyl isobutyl ketone (MIBK) and isopropyl alcohol. The typical exposure dose for PMMA resist is 300 µC/cm^2 when exposed by the 30keV beam, but its sensitivity can be rapidly improved using alternative developers (100 µC/cm^2 when developed with IPA:water solution [48] or even 15 µC/cm^2 when used with an acetone:ethanol solution). PMMA usually allows fabrication of lines with the width down to 50 nm. Its main drawback is bad resistance against ion sputtering or reactive ion etching.

Another example of positive resists is CSAR 62 made by Allresist company. It is chemically semi-amplified resist based on poly(α-methylstyrene-co-α-chloromethacrylate) with high sensitivity (critical dose for exposure by 30keV beam is 65 µC/cm^2). Development of CSAR 62 is usually done using an Amyl acetate developer. CSAR 62 offers high resolution (lines with a width of 6 nm have been reported [49]) and also very good resistance against ion milling [50]. When the resist is overexposed, it provides enhanced undercut profile suitable for lift-off applications. The main drawback of CSAR 62 is its high price compared to PMMA. Another alternative for CSAR 62 is ZEP made by ZEON company. Unfortunately its price over 11 000 USD/l makes it one of the most expensive resists available on the market.

Typical example of a negative resist is AR-N 7520 [51]. It is a novolac based high sensitivity negative resist (critical dose 30 µC/cm^2 at 30 kV). Due to its high resistivity against ion sputtering it is often used as a sputtering mask. Another feature of this resist is its sensitivity to deep UV illumination which enables its use for mix and match lithography processes, that combine EBL with UV mask lithography. It can be developed using Tetra methyl amonium hydroxide (TMAH) based developers used for optical resists.

Another example of a negative EBL resist is hydrogen silsesquioxane. It is a high resolution negative resist enabling fabrication of lines with a width in the sub 10nm regime [52]. It is usually developed using TMAH or salt-based developers. As its structure is

similar to SiO_2, it offers high resistivity against ion sputtering and reactive ion etching. The main drawback of HSQ is its unpredictable and not easy optimizable behaviour. As its sensitivity is very low when compared with other resists (typically over 1000 $\mu C/cm^2$) its exposure is time consuming. This resist can be also very easily destroyed by contact with water, which makes its processing technologically demanding.

Resists are typically deposited using a spin coating method. A droplet of the resist solution is dispensed on a sample substrate and the substrate is spun at a defined speed to create a thin film. The thickness of the film depends on spin speed, solution viscosity and solvent evaporation rate [53]. Fig. 3.3 shows such a dependence of film thickness on spin speed for the PMMA resist.

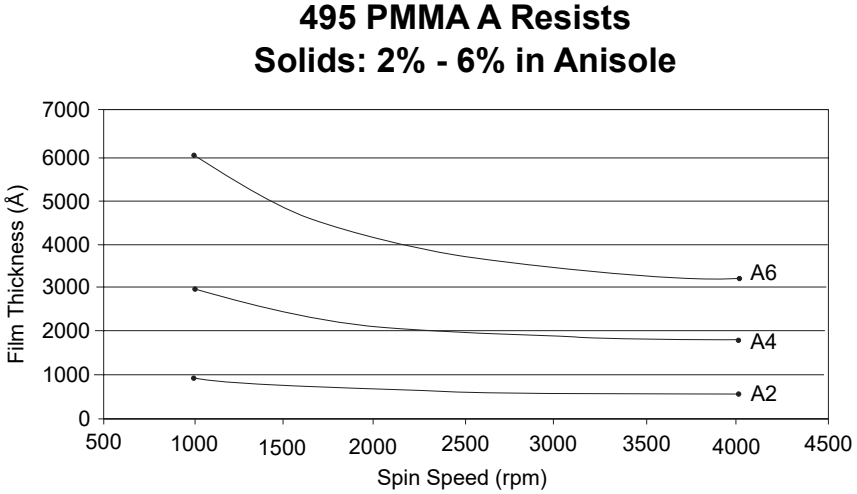

Figure 3.3 Dependence of resist thickness on spin speed for different concentrations of the PMMA resist in anisole, adapted from [54]

Advanced nanopatterning tasks often require specific resist profiles to be obtained, which can be achieved by combination of several resist layer with different properties patterned in one step [55].

3.1.3 Electron beam lithography systems

The types of electron beam lithography systems can be divided into three main categories: Gaussian beam systems, multi-beam systems and shaped beam systems. The design of the Gaussian beam systems usually originates from scanning electron microscopes. The system produces a focused electron beam with the Gaussian intensity profile in the spot. This beam is then scanned over the substrate in order to write a specific pattern. In the multi-beam systems several beams are produced through various optical components based on microelectromechanical systems (MEMS) and controlled separately in order to speed up the exposure. On the other hand, the shaped beam systems produce the beam with a defined shape (often called stamp), the pattern is than divided into shapes, where each shape is exposed at once by the selected stamp of a defined shape.

As the Gaussian beam systems are based on SEM designs, the easiest solutions pose 'EBL conversion kits' – pieces of hardware and software, that can turn a conventional

scanning electron microscope into an entry-level EBL system. Such kits include for example a NanoMaker system from Inreface Ltd., Nano Pattern Generation system from JC Nabity Lithography Systems, Elphy from Raith company or DrawBeam made by Tescan Brno. The pattern generator is connected to external scanning inputs of the microscope electronics and control interface of the microscope blanking system – the system that can turn the beam on or off at high frequencies. The performance of such a system is limited by the design of the used SEM column, which is usually not optimized for EBL applications. Exposure of large areas is also limited by accuracy of SEM stages. The beam energy available by these systems is usually only up to 30 keV, for beam booster based optics often up to 20 keV only.

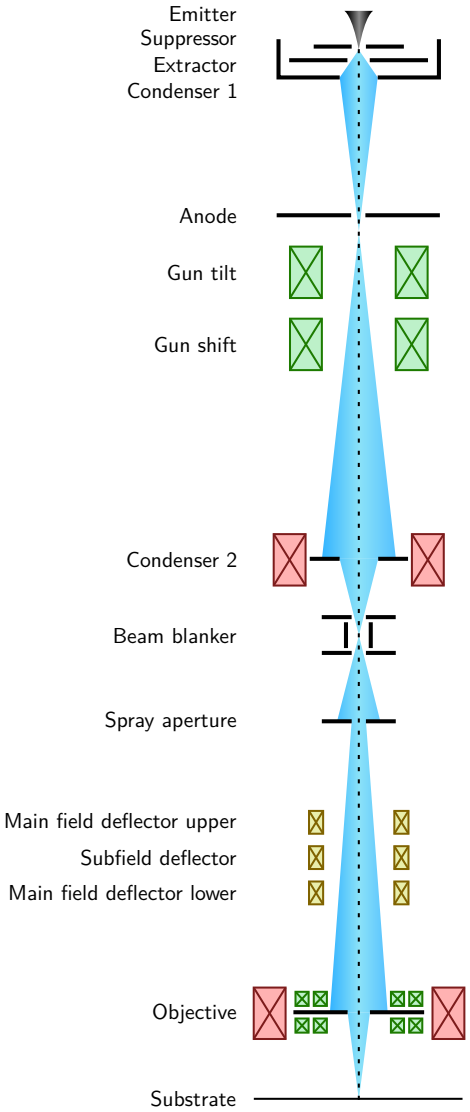

Figure 3.4 Raith EBPG system, adapted from [56]

Dedicated e-beam writers on the other hand often utilize special hardware in order to provide defined repeatable precision and high stability. Fig. 3.4 shows an example of such a system Raith EBPG. Most of the systems use a Schottky field emission gun with

accelerating voltages up to 50 or 100 kV. The columns design usually involves multiple condensers in order to keep the Gaussian beam profile through a wide range of beam currents. Electrostatic lenses are often used to minimize the hysteresis effects of column parameters switching. The scanning system of dedicated EBL systems is usually done as a multi-stage electrostatic deflector, that provides high beam placement repeatability at large fields of view. Dedicated EBL systems are usually equipped with an interferometric stage that ensures precise movements and high mechanical stability. Focusing to sample surface is typically done using an automatic optical distance meters.

The gaussian beam systems usually use two different writing strategies to write large patterns. In the first one – the field stitching strategy, the whole pattern is at first divided into smaller parts according to the view field size of the electron optics. These fields are than scanned one by one with a stage navigating between them. The main advantage of this technique is easier implementation as the stage has enough time to settle, before the exposure is performed. Unfortunately, as the calibration of the write field geometry and stage positioning are never perfect, this approach often produces stitching errors such as double exposures or gaps at field boundaries. Another approach is the modulated-beam moving stage (MBMS) approach, where the stage moves at a constant speed with beam scanning required structures in long stripes. In comparison with the previous approach, the MBMS writing strategy offers a higher writing speed, but requires more demanding control of the stage, that has to be precisely synchronized with beam scanning.

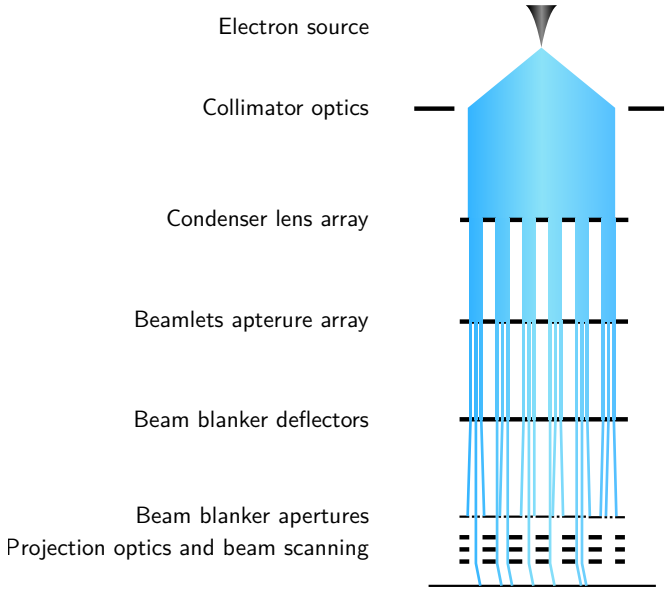

Figure 3.5 Mapper system, adapted from [57]

The multi beam systems use multiple Gaussian beams to write a selected pattern. An example of such systems are the EBL writers produced by Mapper Lithography B.V. (see fig. 3.5). The beam from an electron source is firstly passed through collimator optics producing a 3 cm wide electron beam. This beam is then passed through an array of condenser lenses forming the beam into beam groups. Each beam group is then shaped by an array of nano apertures forming final beamlets (650 000 in total). These beamlets are then independently controlled by a MEMS based beam blanker. The unblanked beams

are finally focused to sample surface using projection optics to produce 25 nm spots on the sample surface. The projection optics also scans with beamlets making a 2 µm view field for each beamlet. In contrast to the single beam systems, where the stitching write strategy is dominating, the Mapper systems employ a modulated beam moving stage strategy.

In the shaped beam systems the beam is shaped by a set of apertures and deflectors, which position the beam in these apertures. The beam is then projected onto a sample making rectangular stamp. The main advantage of a shaped beam systems is a high write speed for patterns containing large areas as the whole rectangular area can be exposed in one step. Unfortunately, the main drawback is a generally worse resolution than in the Gaussian beam systems. Fig. 3.6 shows an example of the old shaped beam system Tesla BS600 developed at the Institute of Scientific Instruments in Brno.

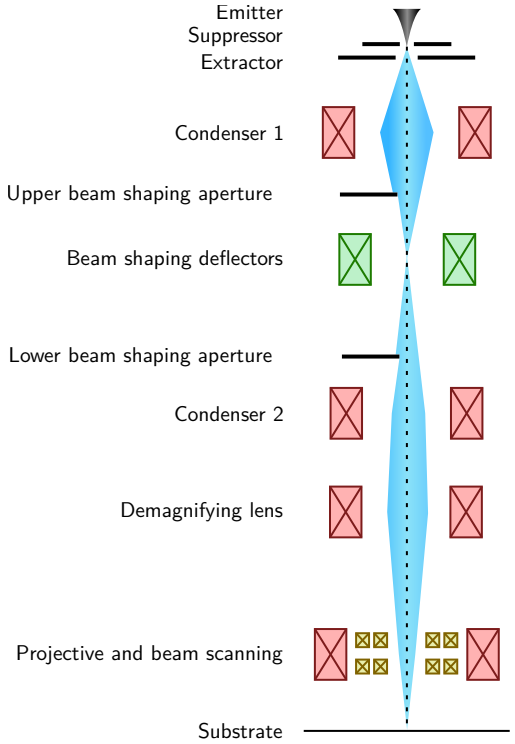

Figure 3.6 Tesla BS600 system, adapted from [58]

The special case of shaped beam systems are the projection systems, where the beam is shaped by a reticle in order to project the whole part of the device or the whole wafer die directly on a wafer. Examples of such systems are SCALPEL and PREVAIL prototypes [59].

3.1.4 Interaction of electron beam with sample

When the beam hits the sample substrate, the electrons typically undergo several scattering events. While traveling through resist layers and substrate, a part of the electron beam is forward scattered and another part is backward scattered. Such scattering events

cause beam spot broadening and unwanted exposure of places, that should remain unexposed. These events are in general called the proximity effect, as the real dose that is deposited at some exposure point also depends on exposure of points in its close proximity. The proximity effect is often described by proximity function (often called beam point spread function), that describes the dependence of density of deposited energy on distance from the beam center. The proximity function was originally described by the formula [60]

$$f(r) = \frac{1}{\pi\,(1+\eta)}\left[\frac{1}{\alpha^2}\exp\left(-\frac{r^2}{\alpha^2}\right) + \frac{\eta}{\beta^2}\exp\left(-\frac{r^2}{\beta^2}\right)\right] \tag{3.3}$$

where the first term (α) describes the short range interactions (mainly caused by forward scattering and development dynamics) and the second term (β) describes long range interactions (backward scattering). The η parameter represents the ratio between the short range and the long range interactions. The resulting dose distribution on a sample surface is then defined by convolution of the point spread function (PSF) and exposed design (p)

$$D(r) = f(r) * p(r). \tag{3.4}$$

The definition of PSF was further extended by various authors [61, 62] up to a model consisting of three Gaussian terms and exponential terms in form [63]

$$f(r) = \frac{1}{\pi\,(1+\eta)}\left[\frac{1}{\alpha^2}\exp\left(-\frac{r^2}{\alpha^2}\right) + \frac{\eta}{\beta^2}\exp\left(-\frac{r^2}{\beta^2}\right) + \frac{\nu}{2\gamma^2}\exp\left(-\frac{r}{\gamma}\right) + \frac{\nu_2}{\gamma_2^2}\exp\left(-\frac{r^2}{\nu_2^2}\right)\right], \tag{3.5}$$

where ν, γ, ν_2 and γ_2 are the additional empiric parameters.

Fig. 3.7 shows example of the point spread function of a 30keV beam passing through a 100 nm thick layer of the PMMA resist on a silicon substrate together with fits for some of the most popular analytical models. Nowadays, numerically defined PSFs are used for most applications providing more accurate description than analytical models.

The point spread function can be obtained in two ways – by running Monte Carlo simulation calculating trajectories of electrons passing through layers of resists or experimentally.

One of the methods for experimental determination of the proximity effect parameters was proposed by Stevens et al. [64]. The method is based on exposure of doughnut structures (see Fig. 3.8). At the center of each doughnut, the effective dose deposited by exposure of doughnut is equal to

$$Q_{\mathrm{p}} = Q\int_{R_1}^{R_2} r f(r)\mathrm{d}r \tag{3.6}$$

with Q representing the exposure dose. If we assume eq. 3.3 as a proximity function f, we can find out that the resist in the center of each doughnut is cleared exactly when the doughnut is exposed by dose at least (assuming positive tone resist)

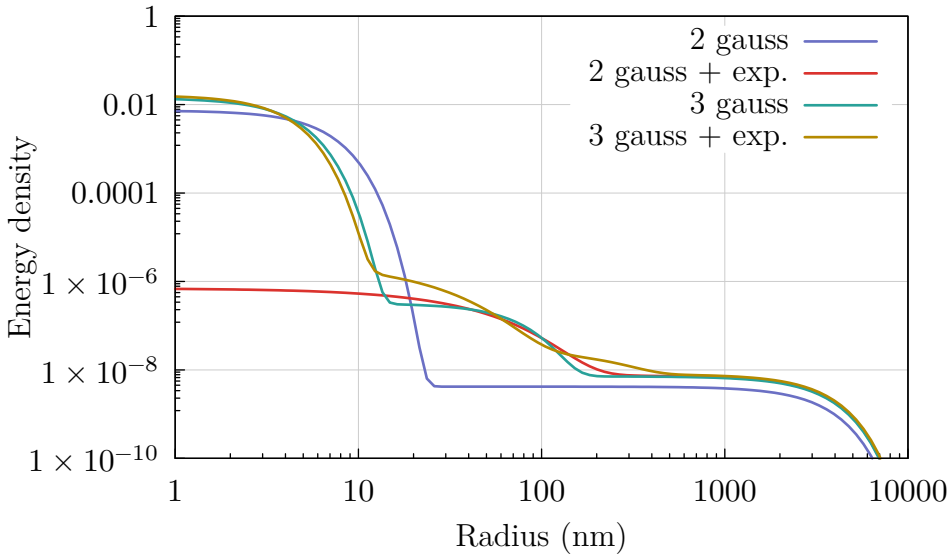

Figure 3.7 Point spread function of a 30keV beam passing through a 100 nm thick layer of the PMMA resist on a silicon substrate, modeled using different analytical models (2 Gaussians, 2 Gausianns and exponential term, ...)

$$D_0 = \frac{Q}{1+\eta}\left[\exp\left(-\frac{R_1^2}{\alpha^2}\right) + \eta \exp\left(-\frac{R_1^2}{\beta^2}\right)\right]. \tag{3.7}$$

By exposing a series of doughnut structures with different R_1 and different exposure dose Q assuming R_2 big enough to include the whole β range, we can easily fit eq. 3.7 to our experimental data and obtain constants α, β, η and D_0.

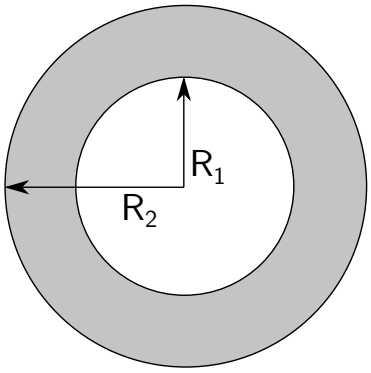

Figure 3.8 Test structures for point spread function parameters determination, adapted from [64]

Another method, the 'Fit before measurement test', proposed by Dubonos et al. [65] uses a test pattern with numerically calculated doses in order to characterize the dose loss by forward scattering and dose gain by unwanted exposure due to backward scattering.

PSFs calculated using Monte Carlo simulations often provide very accurate description of mid-range and long range interactions, unfortunately, as the parameters of the short range interactions are strongly influenced by beam defocus and development dynamics,

the results provided by simulations have to be 'calibrated' by convolving the PSF with a Gaussian function representing a total 'process blur' that is determined experimentally.

In order to reduce the pattern distortion caused by the proximity effect, several methods of pattern correction were developed. The proximity effect can be corrected by doing deconvolution of the written pattern, fracturing the source objects into smaller ones and assigning a specific dose to individual parts [66,67]. Another approach is modification of the object dimensions [68] or generation of sheriff structures at object vertices [69]. Recently, Nien et al. shown, that the proximity effect correction can be solved as minimization of critical-development time variations using a graph theory and swarm intelligence optimization [70]. The latest research [71] shows that the precise application of the proximity correction can also achieve the isofocal point – i. e. the point, where the critical dimension of a fabricated structure is independent on the process blur, for various pattern densities making the exposure less sensitive to beam defocus.

Apart from corrections of the proximity effect, the data preparation also often includes correction of fogging [72], which is the effect, where the primary beam is backscattered and then re-emitted back towards the sample by objective pole piece causing constant dose background and process load effects – microscopic and macroscopic developer fatigue.

When electrons of the primary beam hit the substrate, another effect that can happen, is substrate charging. This effect is usually present at dielectric substrates – materials often used as substrates for plasmonic nanodevices. The substrate charging leads to various pattern distortions or even worse, when the used EBL system relies on live image for beam alignment, the proper focusing on the sample surface can be impossible. Several different approaches of patterning non-conductive substrates have been developed in the past. The most common method is deposition of a conductive layer on top of the resist, which is removed after the exposure. Traditionally, several metallic layers were used, unfortunately, their removal requires wet etching which is time consuming and often technically complicated. Nowadays, these metallic layers are being replaced by conductive polymers, that can be simply deposited using spin coating in a similar way as underlying resist layers. For a quite long time, the Espacer 300 made by Showa Denko was the only choice. Recently, Electra 92 from Allresist company has appeared. While the Espacer provides higher conductivity when compared to the Electra polymer, its layers have a very short shelf life (up to 8 hours) and can be easily damaged by UV light.

The alternative approaches of patterning non-conductive substrates include a critical energy matching technique [73], where the energy of the primary beam is tuned in such a way, that the interaction of electron from the primary beam results in emission of one secondary electron and thus leaving the substrate charge-balanced. Another approach is variable-pressure Electron Beam Lithography [74], the technique borrowed from environmental scanning electron microscopy, where the charge balance is maintained by introduction of residual gasses, that are ionized to positively charged ions by the primary beam, which compensate the negative charge that is being built up at the sample surface.

3.2 Focused ion beam writing

Fabrication using focused ion beam systems [75] is another direct write technique providing massless nanostructure fabrication. From the technical point of view it is similar

technique to Electron Beam Lithography. The only difference is, that this technique uses beam of focused ions instead of electrons. As the weight of ions is much higher, their interaction with material results in elastic collisions leading to material sputtering and thus no resist and related post-processing is needed. Originally, the first commercially available systems came with gallium liquid metal ion sources. The gallium systems provide an optimal balance between the achievable ion current and resolution. Recently, the systems with Xenon plasma ion sources have become available, providing high ion currents and thus high fabrication speeds at cost of lower resolution. Some systems use experimental helium sources [76] (ultra high resolution, low sputtering rates) and multi-species sources [77], where the beam is formed out of an eutectic metal alloy and the selected element is chosen using a Wien mass filter. As the weight of ions is significantly larger than the weight of electrons, magnetic field cannot be used for ion manipulation, making the optics for ion beams strictly electrostatic. Focused ion beam systems are nowadays produced in two configurations: dedicated systems for ion beam nanofabrication, where the ion column is typically perpendicular to the sample surface and stage is navigated using interferometers in a similar way as for EBL systems, and 'dual beam' systems, where the ion column is added to the chamber of classical SEM providing the ability of real time monitoring of the fabrication process at cost of stage precision. Even though these systems are usually designed for analytical purposes or extraction of sample lamellas for Transmission Electron Microscopy, they are often used for fabrication purposes.

The focused ion beam systems provide basically two processes for plasmonic nanoantennas fabrication: Focused Ion Beam Milling and Focused Ion Beam Induced Deposition. In the milling process, the layer of metal is firstly deposited on a selected substrate. The focused ion beam system is then used to selectively remove the metallic film in order to fabricate desired structures. The main advantage of this approach is possibility of direct process observation during fabrication and no need for a pattern transfer after the fabrication. Another advantage is possibility to work with single crystal metallic grains providing superior roughness of fabricated structures [78]. In recent works it has been shown, that by utilization of helium based systems, this approach allows perfect control of geometry of fabricated nanoantennas allowing fabrication of sub-5nm gaps [79]. Unfortunately, the main disadvantage of this approach is low fabrication speed due to necessity to remove large areas of metal, limited scalability and damage of underlying substrate layer, which get amorphised and often mixed with atoms from layers being removed [80].

In the Focused Ion Beam Induced Deposition (FIBID), precursor gases containing metal-organic compounds are introduced near to the sample surface using a gas injection system. These compounds are than decomposed using the focused ion beam into metallic atoms and organic residuals. The metallic atoms are deposited on the sample surface, while the organic residuals are typically removed using a vacuum system. Unfortunately, during the deposition, some of the organic residuals are converted to carbon and also deposited, which often leads to poor plasmonic performance of fabricated structures that require further processing and purification. The Ion Beam Induced Deposition is nowadays usually replaced by electron beam induced deposition (EBID) using electrons instead. One of the main advantages of this approach is possibility to prepare semi 3D structures [81].

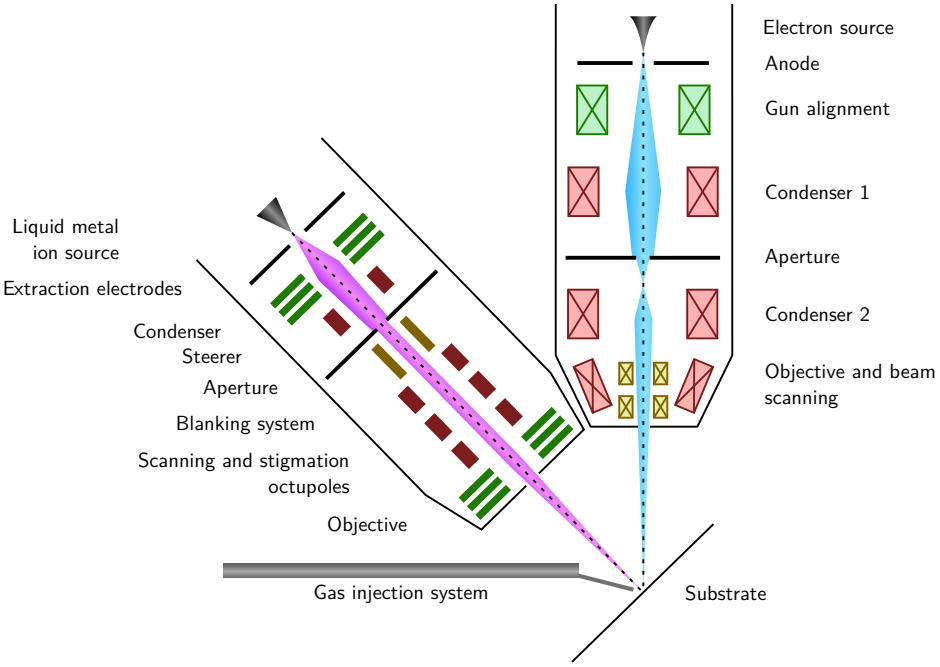

Figure 3.9 Dual beam FIB system, adapted from [75] and [82]

3.3 SPM lithography

Scanning Probe based lithography techniques nowadays provide many different approaches to the nanostructure fabrication [83]. The scanning probe techniques allow for precise navigation of some probe over the sample surface, that can be used for its modification. Traditionally, the local anodic oxidation [84] and Dip Pen nanolithography [85] were state of the art nanofabrication methods for some specific fields of nanotechnology. Recently, thermal scanning probe lithography emerged as a promising general purpose nanofabrication technique, that has been successfully commercialized [86].

In the Thermal Scanning Probe Lithography (TPL), the electrical current flows through the tip area of the cantilever (see fig. 3.10) heating the tip up to 1000 °C. The tip is scanned over the surface in a similar way as during Atomic Force Microscopy in tapping or contact mode. When the tip is heated up, the underlying resist (typically Polyphthalaldehyde) decomposes and evaporates. While the probe moves the tip heating is modulated in order to write desired pattern. One of the advantages of Thermal Scanning Probe Lithography is direct monitoring of the writing process as every line that is written is immediately scanned on retrace move of the cantilever and checked.

Apart from relative simplicity, one of the main advantages of Thermal Probe Lithography is possibility to create overlay lithographic steps and field stitching without markers utilizing natural roughness [87] of the substrate as unlike electron beam lithography or focused ion beam systems the writing cantilever can be used for imaging without any damage to the patterned substrate. Another advantage is possibility to use resist layers prepared by a physical vapor deposition process [88] which eliminates the need for solvent based spin coating. Unfortunately, the main drawback is low writing speed arising from

the mechanical scanning nature of SPM methods. Another challenge is the pattern transfer that often involves special approaches and multi layer hard mask systems [89–91] as the resist thickness used for TPL is relatively low, when compared to the other methods and it has low dry etch resistance.

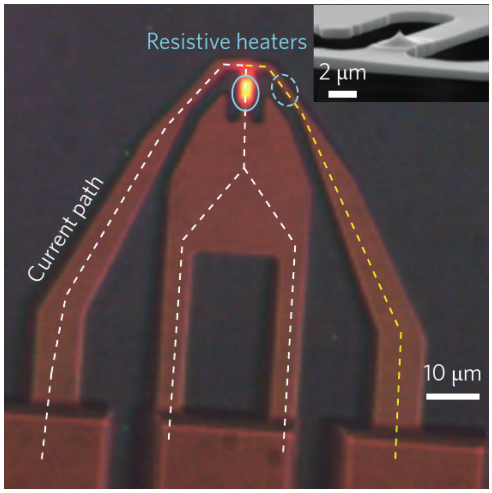

Figure 3.10 Cantilever used for Thermal Probe Lithography (TPL), adapted from [92]

3.4 Extreme Ultraviolet Lithography (EUV)

The ultraviolet mask based lithography has been for many years the standard method of microstructure fabrication in the semiconductor industry. Unfortunately, the lateral resolution of traditional ArF immersion UV lithography was for long time insufficient for plasmonic nanostructures operating in visible light as it is limited by wavelength of used light (193 nm). Luckily, the demand of semiconductor industry for device miniaturization led to development of Extreme Ultraviolet Lithography – optical lithography technique operating at 13.5 nm making sub 20 nm patterning achievable [93,94].

The EUV machine consists of two major components – light source and projection optics. The beam generated by a EUV source is used to project and demagnify the image from a reticle mask to a die on a target wafer. As a light source, the current EUV technology uses a laser-produced plasma light source [95]. The EUV light is produced by plasma of tin droplets inside a vacuum vessel heated by a powerful CO_2 laser and collected by an ellipsoidal mirror. The projection optics is made of cooled mirrors projecting the reticle to typically 26x36 mm^2 field on the target wafer.

EUV technology nowadays usually uses chemically amplified resists where the photo-generated acids catalyses chemical decomposition of a polymer matrix. Experiments with negative tone resists and molecular resists have also been demonstrated [96].

The current limitation of EUV lithography technology arises from low efficiency of light generation and high absorption in projection optics, limiting the throughput of typical EUV writer to approximately 1000 wafers per day.

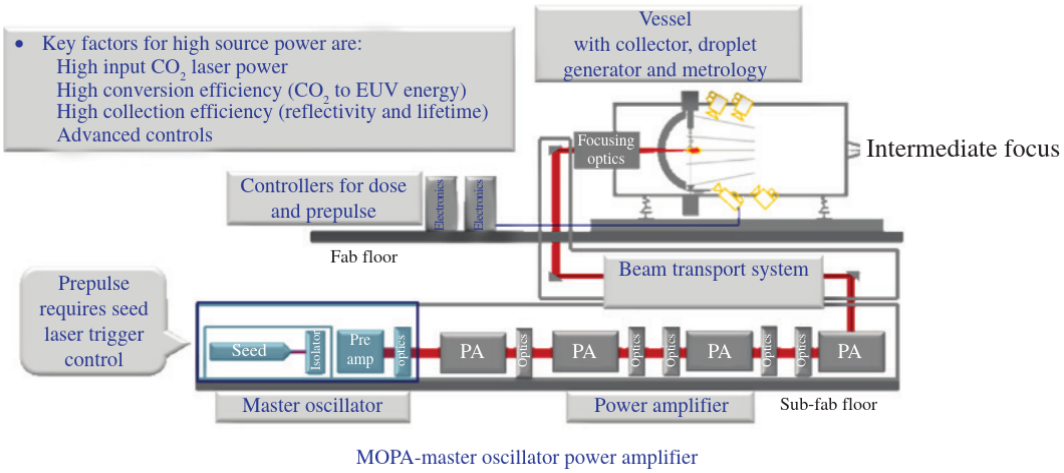

Figure 3.11 Light source for EUV lithography, adapted from [95]

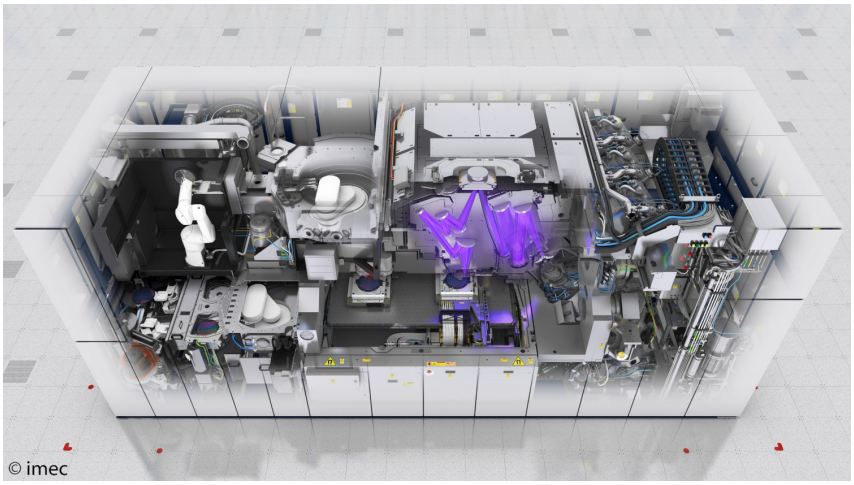

Figure 3.12 ASML Extreme Ultraviolet Lithography system, adapted from [97]

3.5 Nanoimprint lithography (NIL)

Nanoimprint lithography [98,99] is nowadays one of the new emerging techniques capable of fast replication of nanostructures. Thanks to its low cost of ownership it is considered as promising technology for large scale industrial applications.

In nanoimprint lithography, the master mold is fabricated using conventional lithographic techniques at first, that serves as mask. The mold is typically fabricated from silicon or fused silica glass as the technique requires the mold to be mechanically durable. The target substrate preparation begins by a thin polymer layer deposition in the similar way as for conventional lithography. In the next step, the mold is mechanically imprinted into the polymer surface copying the structure into it. Nowadays two different methods are typically used. In Thermal Nano Imprint Lithography, the mold is heated to temperature above the glass transition temperature of the target polymer and pressed against it at high pressure. Upon the contact the polymer is remolded according to the shape of mold and cooled down to recrystallize. Another method is UV assisted nano imprint

lithography, where the target polymer is cured by UV light upon the contact in order to harden it.

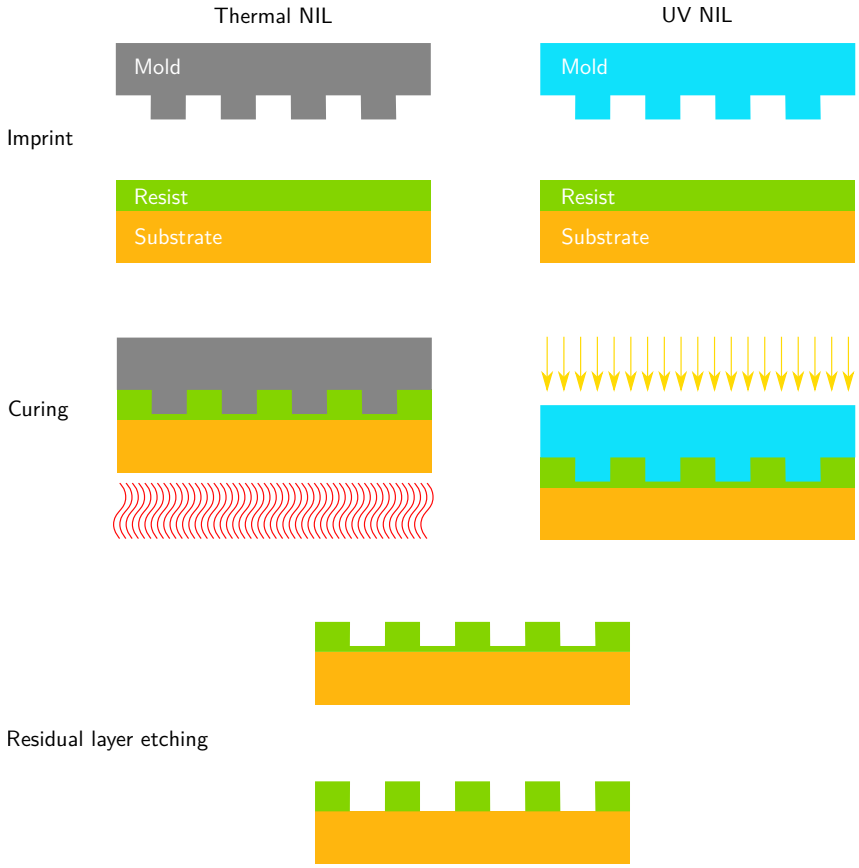

Figure 3.13 Nanoimprint lithography workflow

The main disadvantage of NIL is the residual resist layer, that is left on the surface after the imprinting, that requires the break-through reactive ion etching as the first step in the pattern transfer process. Another problems arise with large areas printing with high density patterns. Luckily, last research shows, that these problems can be overcome by combination of NIL with traditional negative-tone UV lithography [100], where large structures (contact pads, etc.) are masked by a traditional UV mask while the fine features are patterned using NIL approach.

3.6 Metal deposition

When it comes to metal deposition [101] for plasmonic nanostructures fabrication, there are several options available mostly in the realm of physical vapor deposition methods. One of the key parameters of the deposited layer is apart from material composition and purity also size of the grains that form the layer as the grain size can be comparable to the dimensions of fabricated structures and thus can significantly influence the resulting geometry. Due to the high purity of required layers all depositions for plasmonic applications are usually done in high vacuum, where the chamber is typically pumped down to the pressure 10^{-6} Pa using either turbomolecular pumps or cryogenic pumps.

The evaporation is nowadays still one of the easiest methods of thin metallic layer preparation. The deposited material is heated and evaporated towards the sample, where it condenses and creates a layer. Traditionally, the evaporated material was melted directly by electric current flowing through a boat with the material. Unfortunately, such an approach involves complicated regulation due to high volumes of material being melted and risk of contamination or chemical degradation (such as oxidation). Nowadays, the evaporation is typically done using an Electron Beam Evaporation system (see fig. 3.14), where the material is heated using a focused electron beam. The electron beam melts only a thin layer of the material on the top of the crucible, while the rest is cooled (typically by water). As the volume of the melted material is much smaller, the control of the deposition speed can be flexibly achievable using a simple PID regulator. The deposition using evaporators is usually limited by the high melting point of some materials, making reasonable deposition rates for them unachievable.

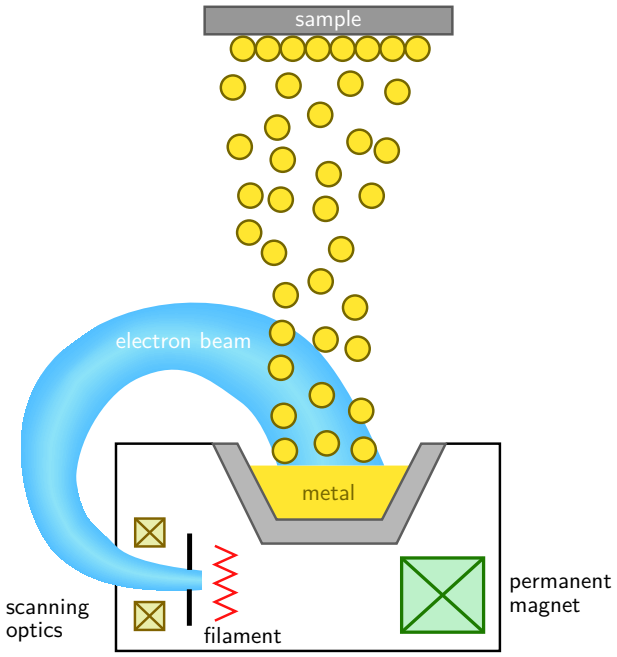

Figure 3.14 Electron beam evaporator, adapted from [102]

Another option of deposition poses plasma sputtering. In the industrial use, the most established method is nowadays magnetron sputtering. In the magnetron sputtering (see fig. 3.15), the chamber is firstly pumped down and then a carrier gas (typically argon or xenon) is introduced into the chamber. The next step is ignition of discharge between the anode and cathode ionizing the carrier gas by cascade collisions with electrons. These ions are accelerated towards the anode (sputtered target) where they sputter atoms of the target towards the sample, where the layer is grown. In the magnetron, there are strong magnets placed around the sputtered target in order to help to confine the plasma near the target area, thus enhancing the sputtering of the material. While the magnetron sputtering is considered as an universal deposition method allowing deposition of various kinds of materials, it often suffers from non-uniform deposition rates making its technical implementation even more challenging.

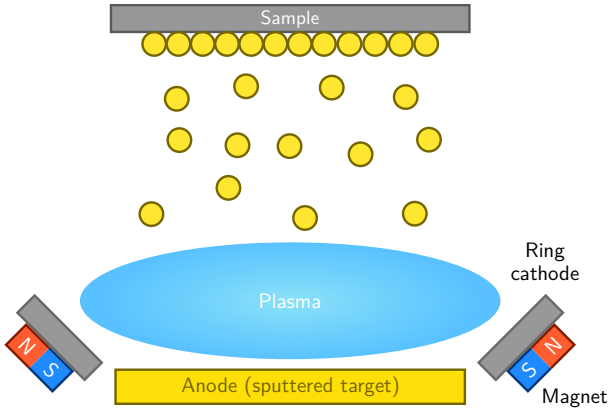

Figure 3.15 Circular magnetron, adapted from [101]

Even though magnetron sputtering nowadays presents the first choice of sputtering deposition, many demanding R&D tasks require a more versatile deposition approach. Such a versatility can be achieved by Ion Beam Assisted Deposition (IBAD) [103]. In the IBAD deposition system (see fig. 3.16), ions for sputtering of the material are generated in a separate part of the system by the Kaufman ion beam source [104]. The plasma is formed inside the source and ions are then extracted from the source using accelerating grids. These ions are then directed to the sputtered target, where they eject atoms of the material to be deposited towards the sample. One of the biggest advantages is presence of secondary assisting ion beam source, that can be used for simultaneous bombardment, and hence to modify it . Such modifications include sputtering the deposited layer using argon ions in order to reduce the grain size, which enhance the resolution of the lift-off process, nitridation of the grown layer by nitrogen ions, or oxidation by oxygen ions.

Apart from deposition, ion beam sputtering systems are often used for material etching through resist masks as a pattern transfer technique. These techniques include both purely physical processes (sputtering) and chemically assisted processes, where reactive gases such as CHF_3 are introduced into the chamber – reactive ion etching [105].

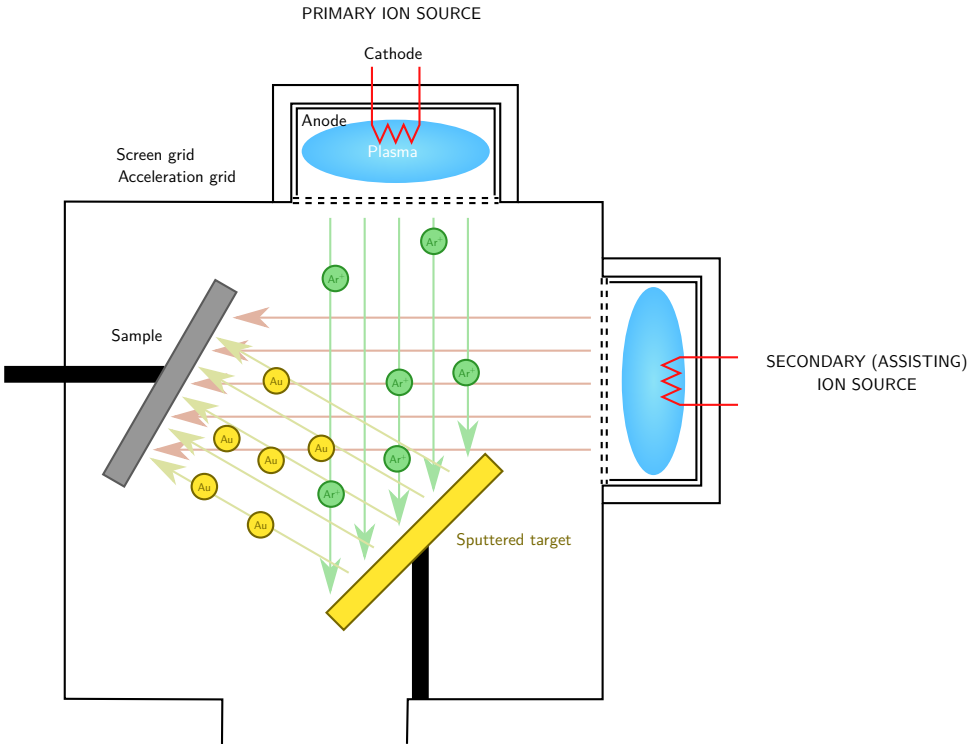

Figure 3.16 Ion beam deposition system, adapted from [103]

4 Characterisation methods

Characterization of plasmonic nanostructures can be divided into two main groups. The first group includes general methods for nanostructure characterization, such as geometry and chemical composition. The second group includes methods for assessment of functional properties of plasmonic nanostructures..

One of the basic method for geometrical characterization of nanostrucutres is Scanning Electron Microscopy [106], which utilizes a focused electron beam for sample imaging. Regarding the plasmonic nanostructures, the SEM imaging is a quite straightforward task, when the user should only consider risk of contamination of the sample by carbon deposited during sample imaging which can alter optical properties of analysed nanostructures by changing index of refraction in their near field region. Another complication of SEM imaging arises from the chosen substrates, that are often non conductive which can lead to the sample charging during inspection. Nowadays, the simplest solution of imaging of non-conductive samples using SEM is deposition of a thin metallic layer. This approach unfortunately definitely deteriorates optical properties of most plasmonic nanostructures and thus such a step should be carefully planned as the last one in the sample characterization. Fortunately, imaging in the low vacuum mode [107] or critical energy matching technique [108] are becoming more and more common.

For characterization of nanostructure morphology Atomic Force Microscopy (AFM) [109] is the first option. As the plasmonic nanostructures are generally made of solid materials, their characterization using AFM can be done in a relatively routine way.

Although other methods of nanostructure characterization (especially chemical characterization methods – Energy-dispersive X-ray Spectroscopy – EDX or X-ray Photoelectron Spectroscopy – XPS [110–112]) are generally useful in troubleshooting of plasmonic nanostructure fabrication, they are more dedicated to thin film characterization and so off-topic in context of this thesis. The following sections describe methods used for functional optical assessment of plasmonic nanostructures.

4.1 Optical spectroscopy

As mentioned in chapter 2, the amplitude response of plasmonic nanoantennas/plasmonic metamaterials is a key characteristic of their optical performance. The optical spectroscopy is therefore the method of the first choice for characterization of their optical properties allowing easy identification of plasmonic resonances in their transmission or reflectance spectra. The spectroscopic assessment of plasmonic nanostructures is often done in te confocal microscopic mode, allowing the signal to be acquired only from a small defined area of the observed sample while providing a wide field microscopic image for navigation during analysis. An example of such an apparatus is in fig. 4.1. The instrument consists of two optical microscopes (upright and inverted) with a sample placed in between of their objectives on a piezo stage allowing its precise positioning. The apparatus can work in two different modes – the mode for measurement of transmittance spectra and the mode for measurement of reflectance spectra. In the reflection mode,

only the upright microscope is used. The sample is illuminated through a beam splitter and microscope objective. The light reflected from its surface is guided both to an eyepiece providing an overview image of the sample and to an optical fiber connected to a spectrometer. As the optical fiber is aperture limited, it allows user to select only a small place of the sample where the signal is collected from. In the transmission mode, the inverted microscope serves for sample illumination, while the upright microscope is used only for light collection. The inverted microscope also provides another eyepiece allowing the sample observation in the transmission mode, when the illumination is provided by the upright microscope.

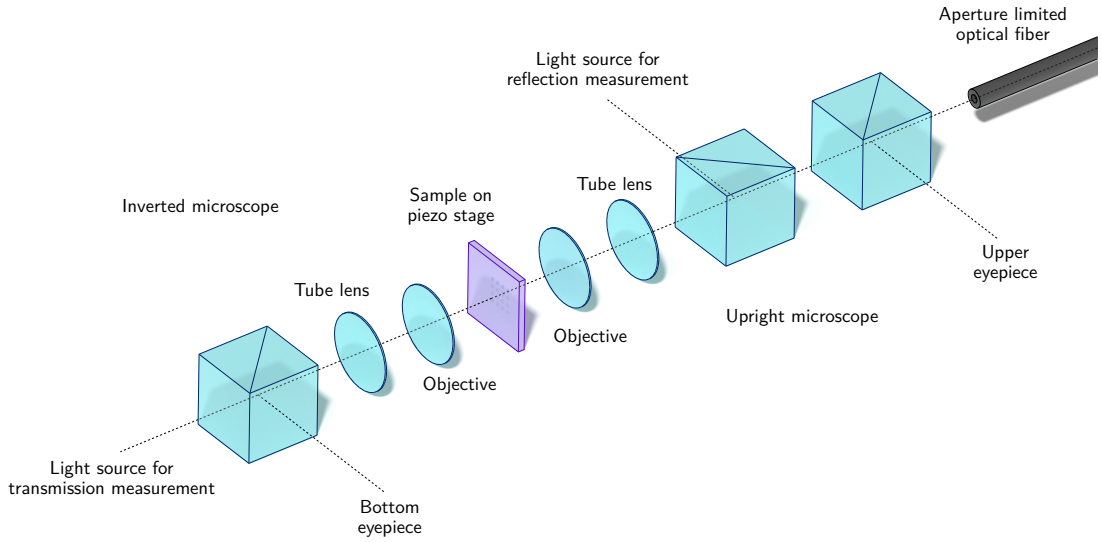

Figure 4.1 Spectroscopy setup, adapted from [113]

When performing any spectroscopic measurements, proper data handling is necessary in order to eliminate any unwanted effects which can lead to misinterpretations of observed data. Every experiment usually starts with measurement of a dark spectrum which represents the spectrum observed by the spectrometer when there is no light coming through the system. Such a spectrum is observed due to imperfections of the setup, where often some parasitic light from the outside can penetrate inside or by imperfections of the spectrometer itself. The measured dark spectrum is then subtracted from all acquired data. When obtaining reflectance or transmittance spectra, another needed dataset is the 'reference spectrum'. As one wants to see only relative changes of the light intensity that is transmitted or reflected due to the presence of plasmonic nanostructures, it is necessary to divide the observed intensity by the reference intensity which describes how the substrate would perform without any nanostructures. Typically, when measuring a transmittance spectrum of a plasmonic metasurface the reference spectrum is obtained just by measuring the spectrum of light transmitted through the substrate without any nanostructures.

Another important parameter of the measurement is the used objective numerical aperture that influences the light collection angle which can lead to different spectra observed by different objectives.

4.2 Fourier Transform Infrared Spectroscopy

In infrared region, the traditional dispersive spectroscopy can no longer be used due to low signal to noise ratio of IR detectors. A different approach is used instead. Fig. 4.2 shows a typical Fourier Transform Infrared Spectroscopy (FTIR) setup [114]. The IR radiation created by a high temperature source (typically a nickel chromium wire or a silicon carbide rod) is collected by a collimating mirror and fed into the Michelson interferometer, where the intensity of the probe beam can be modified in time by changing the position of a moving mirror. The beam modified by the interferometer is then passed through the investigated sample into a detector. Similarly to dispersive spectroscopy for the characterization of plasmonic nanostructures, FTIR is often done in combination with a microscope and apertures that can limit the area from which the signal is acquired.

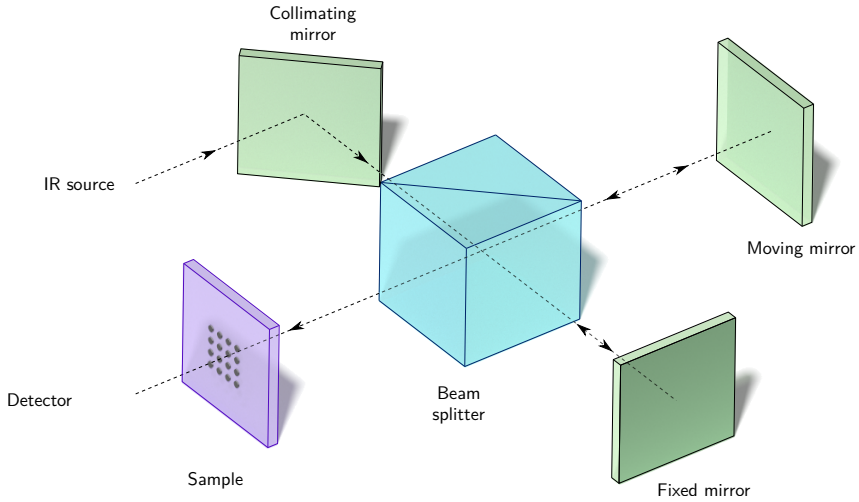

Figure 4.2 Fourier Transform Infrared Spectroscopy setup, adapted from [114]

The typical FTIR measurement consists of a 'scan' where the moving mirror of the interferometer is scanned and the dependence of the amplitude on time (interferogram) is acquired. According to the construction of the interferometer, it is possible to conclude, that monochromatic radiation of wavelength λ will be represented in the interferogram as a sine signal with frequency

$$F = \frac{2v}{\lambda} \tag{4.1}$$

where v is the speed of the moving mirror. As for the polychromatic radiation the interferogram is a linear combination of all included wavelengths, the spectrum (dependence of intensity on the wavelength) can be simply retrieved from the interferogram using the Fourier transform [115].

4.3 Spectroscopic Elipsometry

The spectroscopic elipsometry is a method, that probes how the materials influence the polarization of light upon reflection from their surface. In the typical elipsometry setup

(see fig. 4.3) the sample is illuminated by linearly polarized light. Upon reflection from the sample surface the polarization state of the beam changes turning the linearly polarized light into the elliptically polarized one. The light is then guided through a rotating linear analyser to a spectrometer, where the spectra for different polarizations are acquired.

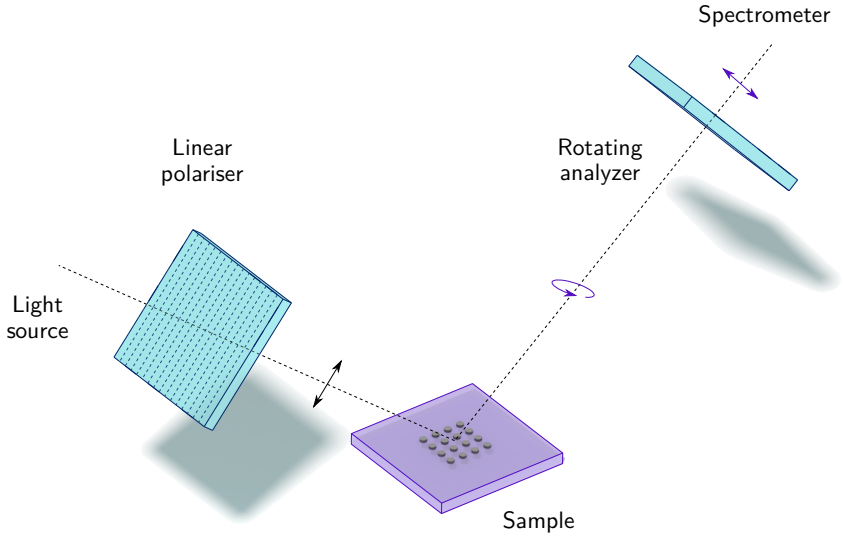

Figure 4.3 Spectroscopic Elipsometry setup, adapted from [116]

The polarization of the light can be described by two perpendicular directions with the respect to the plane of incidence – in plane (p polarization) and out of plane (s polarization) component. Using the Jones formalism, the reflection is then described by the 2x2 matrix of complex parameters

$$\begin{bmatrix} E_{\mathrm{rp}} \\ E_{\mathrm{rs}} \end{bmatrix} = \begin{bmatrix} r_{\mathrm{pp}} r_{\mathrm{ps}} \\ r_{\mathrm{sp}} r_{\mathrm{ss}} \end{bmatrix} \begin{bmatrix} E_{\mathrm{ip}} \\ E_{\mathrm{is}} \end{bmatrix}, \tag{4.2}$$

with E_i representing incident wave and E_r reflected waves in s and p polarizations. In isotropic materials the cross terms r_{ps} and r_{sp} are zero. The elipsometric parameters Ψ and Δ are then defined using the reflectance ratio ρ as [116]

$$\rho = \frac{r_{\mathrm{pp}}}{r_{\mathrm{ss}}} = \tan \Psi e^{-i\Delta}. \tag{4.3}$$

Using Fresnel equations

$$r_{\mathrm{p}} = \frac{n_1 \cos\theta_0 - n_0 \cos\theta_1}{n_1 \cos\theta_0 + n_0 \cos\theta_1}, \tag{4.4}$$

$$r_{\mathrm{s}} = \frac{n_0 \cos\theta_0 - n_1 \cos\theta_1}{n_0 \cos\theta_0 + n_1 \cos\theta_1},$$

where θ_0 is the angle of the incident beam and θ_1 is the angle of the refracted beam it is possible to define the pseudo dielectric function of the observed semi-infinite sample as

$$\langle \varepsilon \rangle = \varepsilon_0 \sin^2 \theta_0 + \frac{(1-\rho)^2 (\sin^2 \theta_0)(\tan^2 \theta_0)}{(1+\rho)^2}. \tag{4.5}$$

For typical measurements (on air), the ambient dielectric function $\varepsilon_0 = 1$, making the elipsometry a suitable tool for characterizing the effective dielectric function of the observed sample. In the application of spectroscopic elipsometry for plasmonic nanostructure characterization, the main task is development of an effective medium model, that describes the effective behavior of the examined structures and than fitting its parameters to the measured data.

4.4 Fourier Plane Microscopy (back focal plane imaging)

For applications of plasmonic nanoantennas in the field of optical metamaterials it is often necessary to examine angle resolved radiation patterns of metasurface building blocks. For a long time, such an analysis has been usually done using numerical FDTD models. Recently, the Fourier plane microscopy has been found an ideal tool for investigation of these patterns experimentally [117].

Fig. 4.4 shows a typical Fourier Plane Microscopy setup. The sample is placed on top of a prism and connected to its surface by index-matching immersion oil and illuminated through that prism from side under the total internal reflection angle. Such an illumination ensures sample excitation by an evanescent field which provides an effective suppression of the driving field in the resulting image. The light scattered by the sample is collected by a high NA objective. The telescope behind the objective together with a tube lens projects the image to a detection CCD. The Fourier lens, when inserted, refocuses the telescope to the back focal plane of the objective, where the image containing angle dependence information can be obtained. The pinhole is used to select a single antenna on the sample surface to collect the observed information from there.

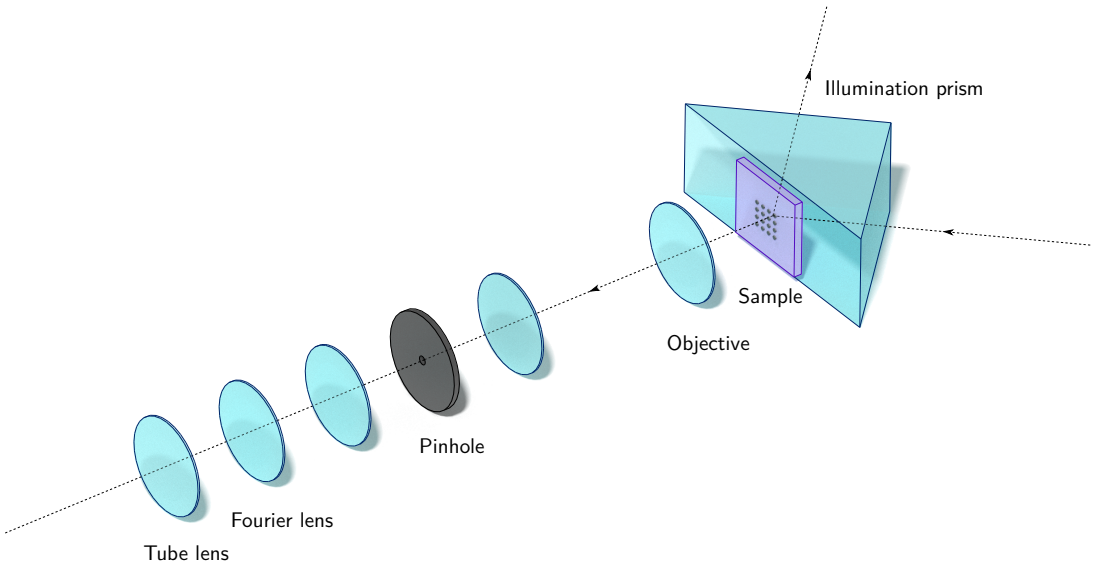

Figure 4.4 Fourier plane microscope, adapted from [117]

4.5 Quantitative Phase Microscopy

The Quantitative Phase microscopy (QPM) [118] presents a group of interferometric microscopy methods providing the quantitative wide field phase imaging. The quantitative phase microscopy finds its main applications mainly in biology, cell and cancer research [119–121], but its techniques are not limited to these applications and provide useful general-purpose imaging tools.

The QPM is based on the interference of two waves originating from the same source in the image plane. One of these waves is the object wave which is interacting with the observed sample and the second one is the reference wave which is interacting with the reference sample or it is just a wave unaffected by the sample at all. The interference of these waves can be described as

$$\begin{aligned} I = |O+R|^2 &= |O|^2 + |R|^2 + OR^* + O^*R \\ &= |O_0|^2 + |R_0|^2 + 2O_0R_0\cos\left(\varphi_\mathrm{O} - \varphi_\mathrm{R}\right) \end{aligned}, \tag{4.6}$$

where O and R represent the object and reference waves, O_0 and R_0 their amplitudes and $\varphi_O - \varphi_R$ their phase difference.

There are two main approaches of recording the information in the quantitative phase microscopy: in-line and off-axis.

4.5.1 In-line Interference Microscopy

Fig. 4.5 shows a typical setup for recording images using the in-line QPM [122]. The beam from a polychromatic broadband source is split into two arms – the object and reference ones. The beam in the object arm passes through the observed sample and interferes with the reference beam, which is mixed back by another beam splitter. In the in-line setup, the object and the reference beams interfere precisely aligned to each other. The value recorded at each point of the image is exactly the mixture of the amplitude DC terms and phase-containing cross terms as in eq. 4.6. In order to separate the cross terms during hologram reconstruction, it is necessary to acquire minimally four images, where the phase of the reference beam is shifted in respect to the object beam by four $\pi/2$ steps.

The recorded images than become

$$\begin{aligned} I_1 &= |O_0|^2 + |R_0|^2 + 2O_0R_0\cos\varphi, \\ I_2 &= |O_0|^2 + |R_0|^2 + 2O_0R_0\sin\varphi, \\ I_3 &= |O_0|^2 + |R_0|^2 - 2O_0R_0\cos\varphi, \\ I_4 &= |O_0|^2 + |R_0|^2 - 2O_0R_0\sin\varphi, \end{aligned} \tag{4.7}$$

where the φ represents the phase of the object wave. The complex amplitude and phase of the object wave can be than calculated as

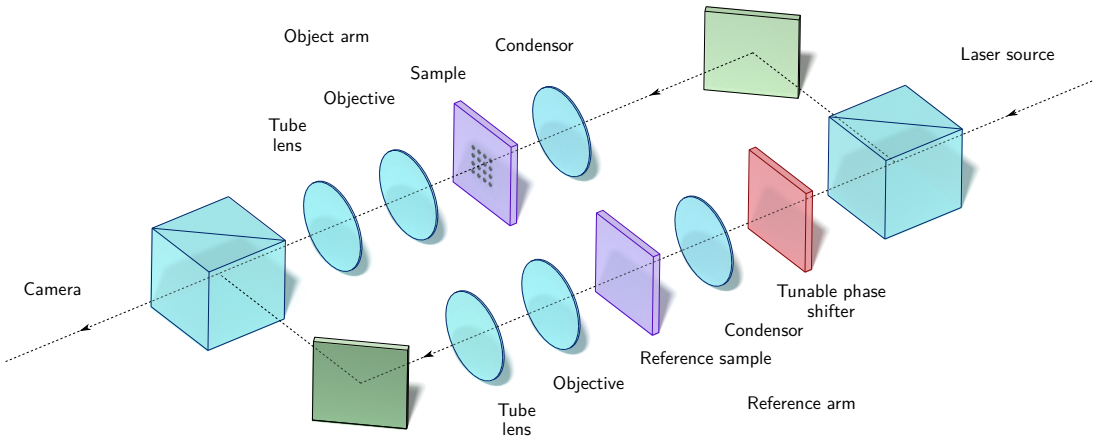

Figure 4.5 In-line phase shifting holographic microscope

$$O = \frac{1}{4R}\left[(I_1 - I_3) + \mathrm{i}\,(I_4 - I_2)\right]$$
$$\varphi = \arctan\left(\frac{I_4 - I_2}{I_3 - I_1}\right) \tag{4.8}$$

While the in-line approach provides some advantages such that the resolution of reconstructed images is the same as the resolution of the acquired interferogram (in comparison to the off-axis setup), which is useful for QPM in the infrared region, where high resolution cameras are still very costly. As it requires acquisition of many images, it is not suitable for imaging of dynamic processes, where the observed object can change between acquisition of dataset images and also requires a very good mechanical stability of the whole system in order to have the acquired source images well aligned.

4.5.2 Off-axis Holographic Microscopy

The need of observation of dynamic processes and better stability led to development of an off-axis holographic microscopy setup. In contrast to the in-line setup, in the off-axis setup the complex amplitude can be reconstructed from a single image making the proper alignment of many images unnecessary. Fig. 4.6 shows a Coherence-Controlled holographic microscope (CCHM) [123,124] – one of commonly used off-axis QPM setups.

The input beam from a broadband polychromatic source is divided by a beam splitter in two arms (object and reference ones). The light in the object arm interacts with an observed sample, the light in the reference arm passes just a reference sample. Both beams interfere at the camera plane at the off-axis angle ϑ. When the hologram is obtained using an achromatic and space invariant off-axis setup, the image term OR^* and twin image term O^*R are separated from the zero-order (autocorrelation) term $|R|^2 + |O|^2$ by a spatial carrier frequency

$$f = \frac{2\sin(\vartheta_0)}{\lambda}, \tag{4.9}$$

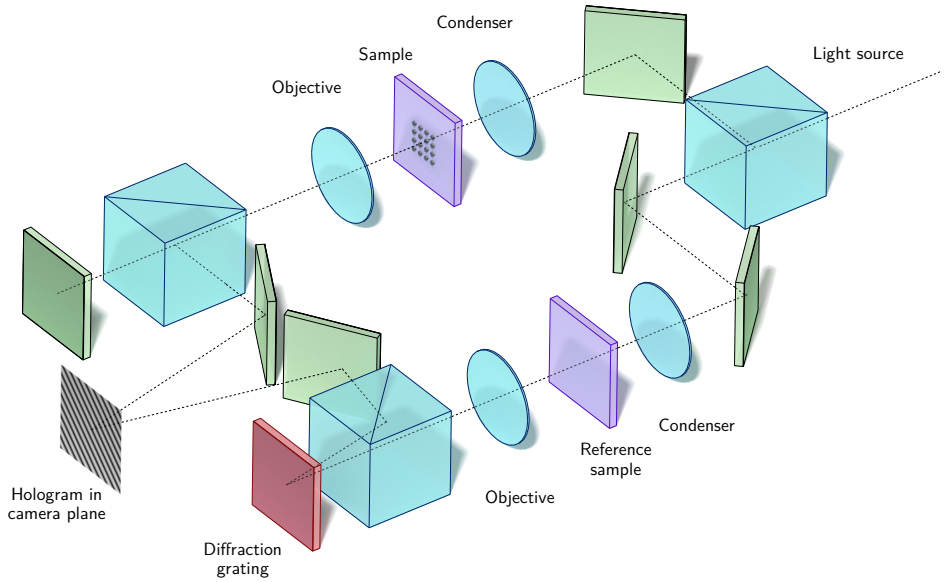

Figure 4.6 Coherence-controlled Holographic Microscope (simplified)

where λ is the illumination wavelength. This property allows the complex amplitude to be reconstructed from single recording using the method developed by Thomas Kreis [125]. The reconstruction process is shown in fig. 4.7. The first step of hologram reconstruction is thus calculation of the hologram Fourier transform which turns it into the spatial frequency domain. The next step is extraction of the image term (OR^*) using the circ function followed by apodization using the Hann window. After shifting the object term to the center of the frequency domain space the complex amplitude I of the object wave can be calculated using the inverse Fourier transform. The phase can be than simply calculated as

$$\phi = \arctan \frac{\mathrm{Im}(I)}{\mathrm{Re}(I)}. \tag{4.10}$$

However, due to differences in optical components used in the object and reference arm, the phase information is usually modulated on a spherical background exceeding the 2π range, which lead to division of the image to several $0-2\pi$ rings. The next step in the image processing is thus 'phase unwrapping', where a special algorithm tries to identify these zones and connect them together in order to convert the image from the $0-2\pi$ range to its real range. The last step of the processing is fitting of the 2D polynomial surface, that is then subtracted from the phase image as a background.

In contrast to another commonly used off-axis microscopes, the CCHM uses a non-coherent light source (typically a halogen bulb with a colour filter), which requires the light path in the object and reference arm to be almost identical (with errors at most in the order of coherence length) to preserve interference, when beams are combined. On the other hand, the non-coherent illumination provides better phase resolution due to the lack of any coherence noise and ability to use coherence-gating effect, which can be utilized for optical sectioning of observed specimen. The biggest disadvantage of the off-axis setup is reduction of the image reconstruction as due to the cropping of the image in the Fourier

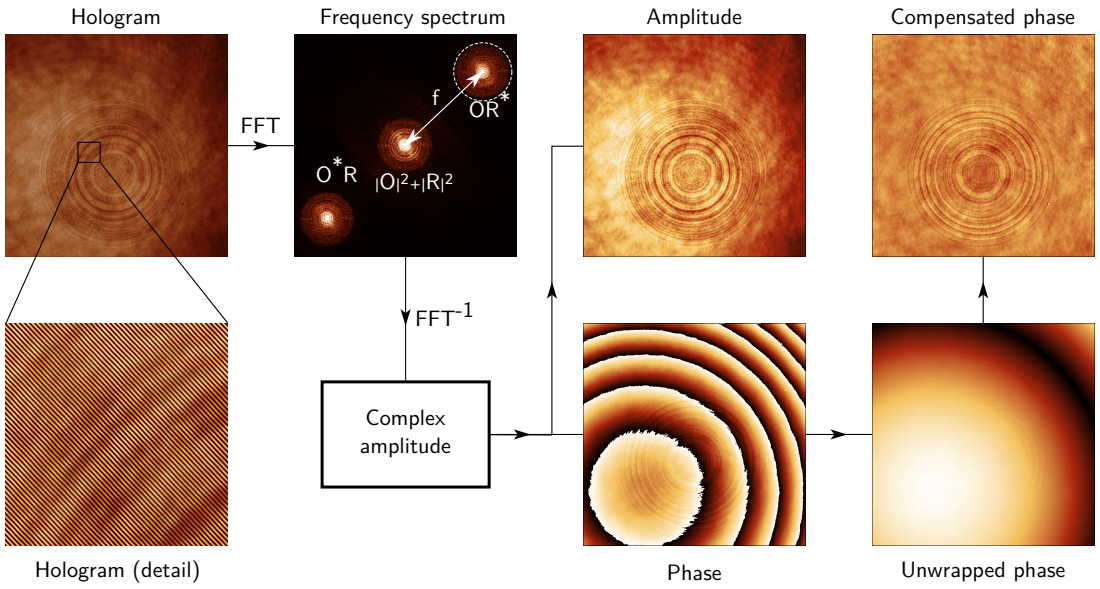

Figure 4.7 CCHM hologram reconstruction

space the resolution of the reconstructed image is half of the resolution of the hologram acquired by the camera.

4.6 Cathodoluminescence and Electron Energy Loss Spectroscopy

Cathodoluminescence and electron energy loss spectroscopy (EELS) differ from other characterization methods significantly as they use focused electron beam for plasmon mode excitations instead of the light, thus making them quite special techniques in the broad palette of optical characterization methods.

In EELS the sample is illuminated by high energy electron beam (typically in Scanning Transmission Electron Microscope – STEM). The electron passing a plasmonic nanostructure causes disturbances in the charge distribution inside the nanoparticle leading to the excitation of bulk and surface plasmon modes. During the interaction, a part of the electron energy is transferred to a specific plasmon mode making it loose energy, which corresponds to that one of the created plasmon mode. In the EELS experiment the beam transmitted through the sample is guided inside an energy spectrometer, where the energy spectrum of transmitted electrons is measured. The EELS spectrum is basically a histogram of the electron energy losses from which the energies of excited plasmon modes can be identified.

EELS has two significant advantages for the plasmonic nanostructure characterization: the electron beam in STEM can be focused into a very small spot making the nanoparticle excitation localised at some specific point. This is often used in 'mode mapping' applications, where the beam is scanned over the nanoparticle with the spectrum being acquired at every point. In such a dataset the user can then easily visualize the lateral distribution of places where some specific mode can be excited giving the picture of the mode charge distribution simultaneously. The another advantage arises from the electron excitation process which allows dark modes and breathing modes of plasmonic nanoparticles

to be excited and visualised in addition to bright modes related to traditional far field light excitation.

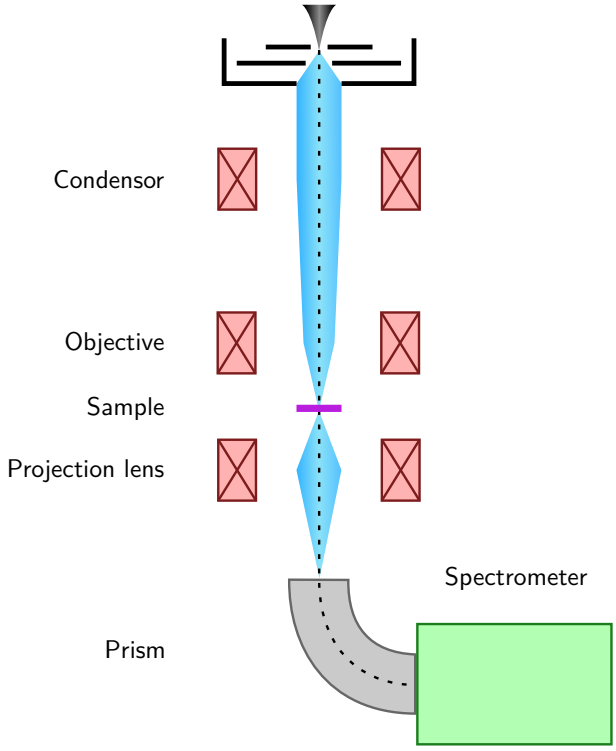

Figure 4.8 EELS measurement in STEM, adapted from [126]

Unfortunately, as the EELS is performed in STEM, the sample for investigation needs to be very thin, which makes a study of structures prepared on traditionally used substrates impossible. Another complication of EELS studies in plasmonics is a very low energy of the surface plasmon modes (around 1 eV making their loss peaks often hidden in the 'zero loss' peak of the EELS spectrum corresponding to the electrons that are scattered elastically (i.e. electrons, that do not loose their primary energy). It makes the proper processing of the EELS spectra often mathematically demanding.

Cathodoluminescence can be considered as a complementary method to EELS. Plasmons are excited by the focused electron beam in the similar way as during the EELS experiments, but instead of transmitted electrons the light emitted by plasmon relaxation is examined. This gives the cathodoluminescence some of the features unique to EELS such as the study of the light radiated by plasmons in a similar way as during the traditional far field spectroscopy. Moreover, it has been demonstrated, that it is possible to use cathodoluminescence in combination with the back focal plane imaging to obtain angle-resolved radiation patterns of plasmonic nanoparticles. Another advantage of the cathodoluminescence is no need for any special substrates (in addition to STEM, also conventional SEM can be used) with the limitation caused only by possible substrate charging and cathodoluminiscence generation in the substrate itself during its irradiation by the electron beam.

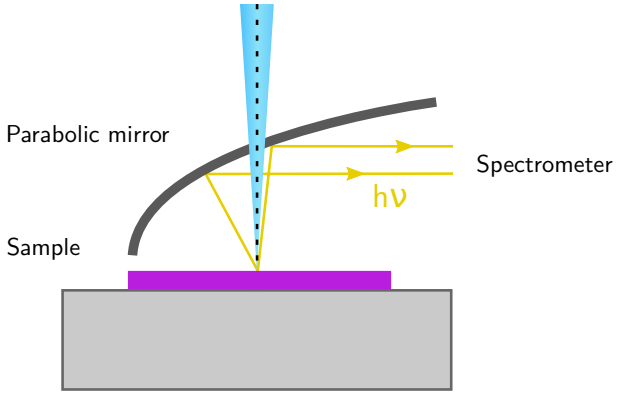

Figure 4.9 Cathodoluminescence measurement, adapted from [127]

5 Patterning large area plasmonic nanostructures using VP-EBL

As shown in chapter 2, plasmonic nanostructures for applications working in the visible range are often fabricated on non-conductive samples such as fused silica, quartz crystals, and others. EBL patterning of such substrates is often challenging as special treatment for charge dissipation is needed. The commonly used workflow involves deposition of temporary conductive layers, which have to be removed before the sample development. While such an approach present the state-of-the-art option, it complicates the fabrication process adding several steps increasing the probability of fabrication failure. In this context, alternative approaches eliminating necessity to use auxiliary conductive layers are being actively developed[1].

The variable pressure electron beam lithography (VP-EBL) is one of the most promising alternative candidates [74]. The technique itself is based on variable-pressure electron microscopy, a technique routinely used for biological samples imaging. Such a technique involves modification of the SEM column where an additional aperture is placed into the objective lens allowing separation of the electron beam column and the sample chamber. The aperture should be precisely centered in the objective crossover point in order to prevent any unwanted cropping of the achievable view field. The next step is introduction of a residual gas inside the chamber (typically N_2 or H_2O) at pressures ranging from 50 Pa to 500 Pa. The aperture allows differential pumping keeping high vacuum inside the SEM column while maintaining low vacuum in the sample chamber. When the primary electron beam hits atoms of the introduced gas, the atoms get ionized and interact with the sample compensating the negative charge being built up on its surface. The imaging in the low vacuum mode also needs special detectors, that are differentially pumped in order to prevent any discharges between extraction grids. As the electron beam lithography is the process very similar to SEM imaging same approach for charge dissipation during the EBL on non-conductive samples can be used.

The VP-EBL technique has been originally demonstrated with the water vapour system, which is typically used in biological imaging. Unfortunately, maintaining a constant environment inside the SEM chamber with the water vapour system for long time is often very complicated. This chapter will describe experiments [128] which focused on using nitrogen gas instead. As nitrogen is usually available in nanofabs and as it can be simply dosed into the SEM chamber using dosing valves, it is an attractive alternative to water vapor systems. Experiments were done in collaboration with colleagues from the Tescan company and CEITEC.

[1] based on J. Babocký, P. Dvořák, F. Ligmajer, M. Hrtoň, T. Šikola, J. Bok, and J. Fiala, Journal of Vacuum Science & Technology B 34, 06K801 (2016)

5.1 Sample fabrication

As a substrate for sample fabrication, we have chosen conventional microscope glass slides. After the substrate cleaning in acetone and iso propyl alcohol, substrates were coated by the poly-methyl metacrylate electron beam resist (molecular weight 950 000, 3% solution in ethyl lactate) using conventional spin coating (see chapter 3.1.2). The resist was baked out for 90 s at 150 °C. For VP-EBL exposures no other sample treatment was performed. Samples were exposed using TESCAN Mira 3 environmental scanning electron microscope with the DrawBeam pattern generator. The microscope is equipped with a low vacuum SE detector, that was used for navigation and focusing on the sample surface prior to the exposure. Unfortunately, the detector is pumped by its own turbo pump which can cause mechanical vibrations that influence the beam position stability. In order to prevent the vibration transfer during exposure, the turbo and detector were switched off during the exposure. Samples were developed in methylisobutyl keton-iso propyl alcohol solution (1:3) for 60 s and rinsed in iso propyl alcohol for 30 s. For comparison, another set of samples was prepared using conventional approach with conductive polymer. These samples were coated by a 60nm layer of Electra 92 conductive polymer made by Allresist company after the resist baking step and exposed in the high vacuum mode (10^{-3}Pa). The conductive polymer was removed before resist development using deionised water. The sample fabrication was finished by deposition of a thin titanium adhesion layer followed by a 40 nm thick layer of silver and lift-off process in acetone.

5.2 Beam current

As the primary beam interacts with molecules of nitrogen gas inside the chamber, some electrons are scattered causing decrease of current reaching the sample surface. In order to carry out the exposure, we have at first measured the dependence of the absorbed beam current on the chamber pressure. From the imaging experience we have concluded to work in the pressure range 20 – 200 Pa. The results (see fig. 5.1) show that the current linearly decreases as the pressure increases due to higher probability of collisions between electrons of the primary beam and nitrogen atoms.

5.3 Test samples

With knowledge of the beam current dependence, we have focused on optimization of VP-EBL process pressure and dose for fabrication of plasmonic nanoantennas on a glass substrate. For these purposes, we choose 10x10 µm^2 arrays of silver nanodiscs with a diameter ranging from 50 to 150 nm and a thickness of 40 nm. The pitch between nanodiscs was chosen as double of the diameter in order to keep the fill factor constant for different arrays. We expected such structures to exhibit clear localised surface plasmon resonances in the visible range, that should be easily observable as artificial colours by optical microscope. These arrays were exposed by different doses (300 – 450 µC/cm^2) at pressures ranging from 20 to 200 Pa (nitrogen atmosphere). The layout of the test structure is shown in fig. 5.2.

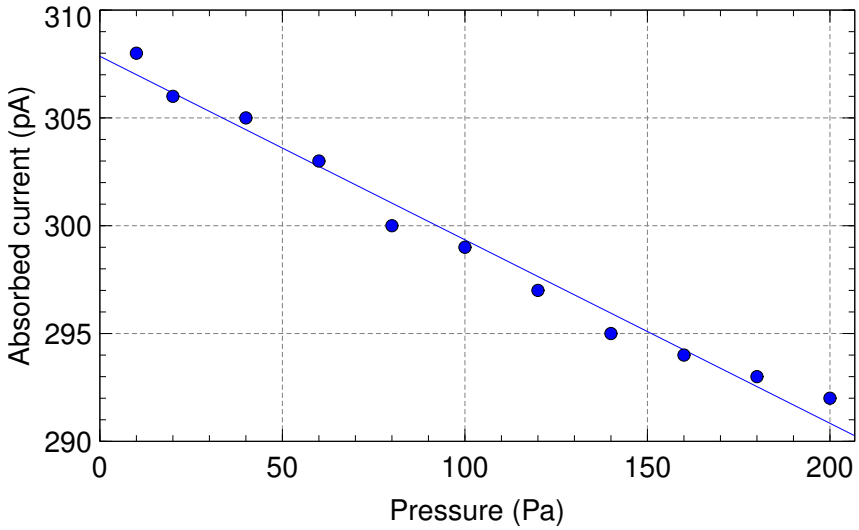

Figure 5.1 Dependence of absorbed beam current on the chamber pressure, adapted from [128]

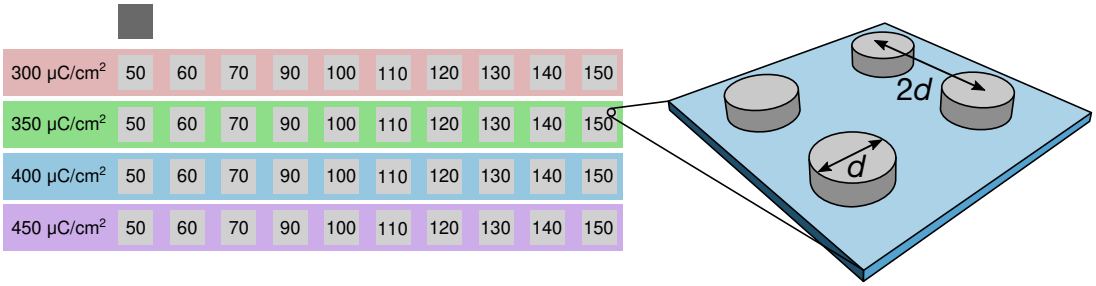

Figure 5.2 Layout of the test samples for variable pressure EBL, numbers in each square represent diameter of nanodiscs in nano meters, adapted from [128]

Fabricated samples were investigated by optical microscopy in the reflection mode (see fig. 5.3). All fabricated arrays exhibit localised surface plasmonic resonances in the visible range, that can be observed as colours. According to the models presented above, smaller nanodiscs have resonances at smaller wavelengths, that can be observed as blue tint in the scattered light. On the other hand, structures with larger diameters have resonances at larger wavelengths turning them to red. As the pressure in the SEM chamber increases, the beam shape gets altered, thus changing its properties. This leads to a decrease of the exposure dose for structures exposed at higher pressures which is manifested by a significant blue shift of fabricated structures (smaller structures).

In order to asses the effectively of the nitrogen atmosphere on charge dissipation we have investigated the geometry of fabricated arrays by scanning electron microscope. When the charge dissipation is not sufficient, the charge being built up on the sample surface leads to errors in beam positioning which are manifested as pattern distortion (parts of the pattern that are written later are shifted away from parts written at the beginning of the process due to the accumulated charge). Fig. 5.4 shows nanodiscs with a diameter of 150 nm exposed at 400 µC/cm^2 prepared at three different conditions. The structure *a)* was exposed at 20 Pa, *b)* at 120 Pa and *c)* is the reference structure fabricated using the conductive polymer layer. We can see, that for the structure *a)* the pressure

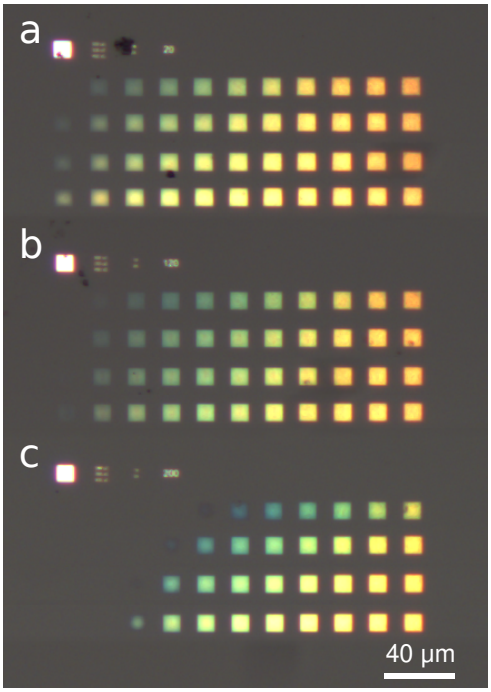

Figure 5.3 Scattered light optical image of fabricated test structure for pressure a) – 20 Pa, b) – 120 Pa, c) – 200 Pa, adapted from [128]

inside the SEM chamber wasn't sufficient for charging effects reduction making the pattern distorted bleeding out of the desired area (yellow square). For the structure *b)* (120 Pa) the charge compensation was successful making almost no difference to the reference structure. The quantified pattern distortion was calculated as the ratio between the area of the structure fabricated by VP-EBL and the reference structure. In fig. 5.4, panel d we can see that the pressures above ~100 Pa successfully prevent any pattern distortion. According to the results, the pressure 120 Pa and dose 400 µC/cm^2 were selected as optimal parameters that provide the best trade-off between charge compensation and resolution preservation.

The optical performance of fabricated structures was examined by optical spectroscopy in the transmission mode. We have used the confocal setup [113] based on a Nanonics multiview system introduced in chapter 4.1. Fig. 5.5 shows a transmittance spectra of nanodiscs fabricated by VP-EBL (solid) and conventional (dashed) approach. Both sets of fabricated nanodiscs exhibit well defined LSPR resonances that correspond to colours observed in optical microscopy images making VP-EBL the suitable method for plasmonic nanoantenna fabrication.

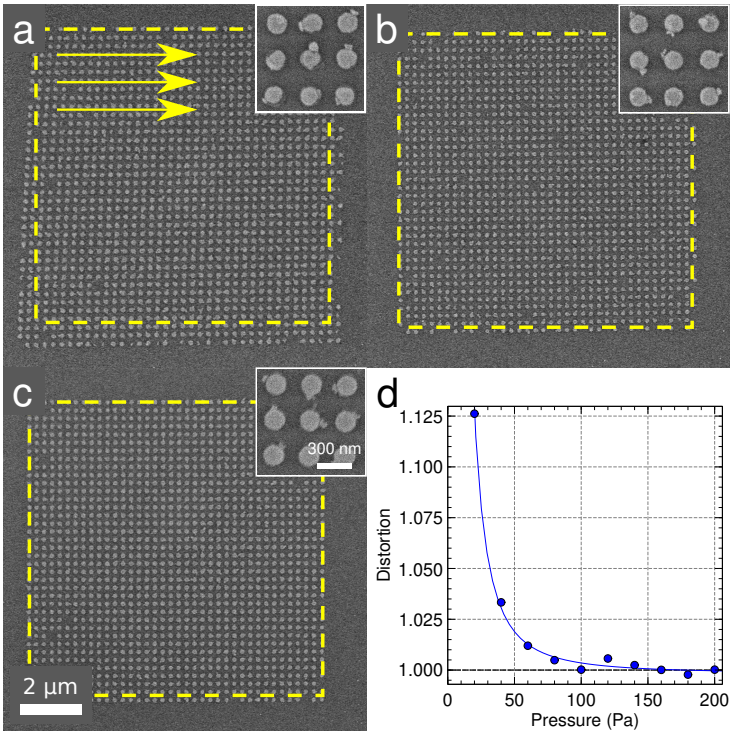

Figure 5.4 SEM images of fabricated nanoantenna arrays, a) VP-EBL exposure at 20 Pa, b) VP-EBL exposure at 120 Pa, c) reference structure exposed with a conductive polymer, d) dependence of pattern distortion on chamber pressure. The yellow square shows the designed pattern area, the arrows show patterning order,adapted from [128]

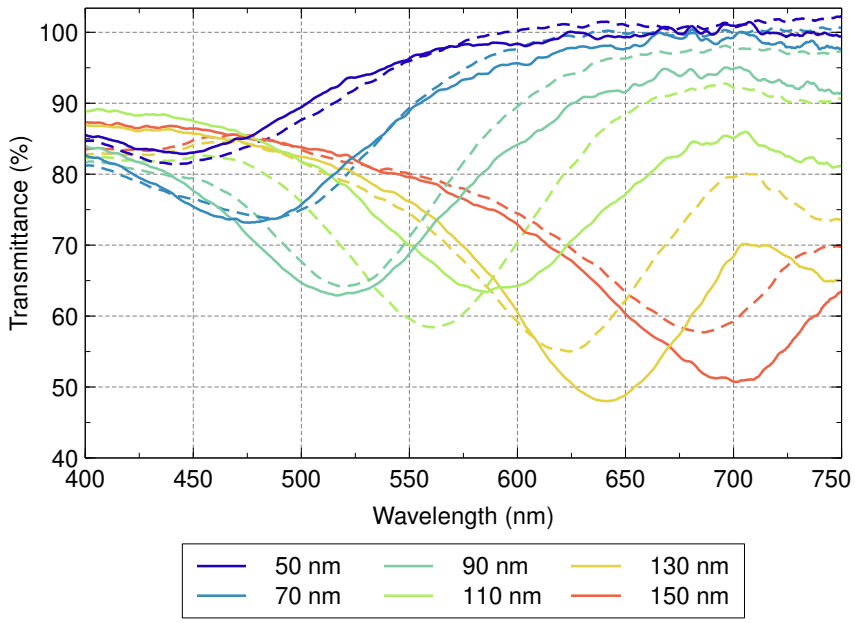

Figure 5.5 Transmittance spectra of fabricate nanodiscs, solid lines correspond to spectra fabricated by VP-EBL, dashed ones by the conventional approach with conductive coating, adapted from [128]

5.4 Large area exposure

To demonstrate the VP-EBL process stability, we have exposed a large area plasmonic colour image (3x5 mm^2). The structure itself was assembled from 20x20 μm^2 arrays on nanodiscs with different sizes in order to create pixels of different colors. The patterning was controlled using a custom script through the TESCAN SharkSEM scripting interface, which allowed us to use a PNG image as a control template with each pixel representing one 20x20 μm^2 write field. The structures in each write field were assigned according to the pixel colour in order to produce the desired optical effect. Fig. 5.6 shows the resulting fabricated structure with the template image in its corner. Even though the exposure was running for 36 h, the exposure parameters of the VP-EBL process (i.e. chamber pressure, beam current, and spot size) are stable enough to result in nanoantennas with correct 'colours', and therefore, the technique is suitable for prototyping large-scale advanced plasmonic devices.

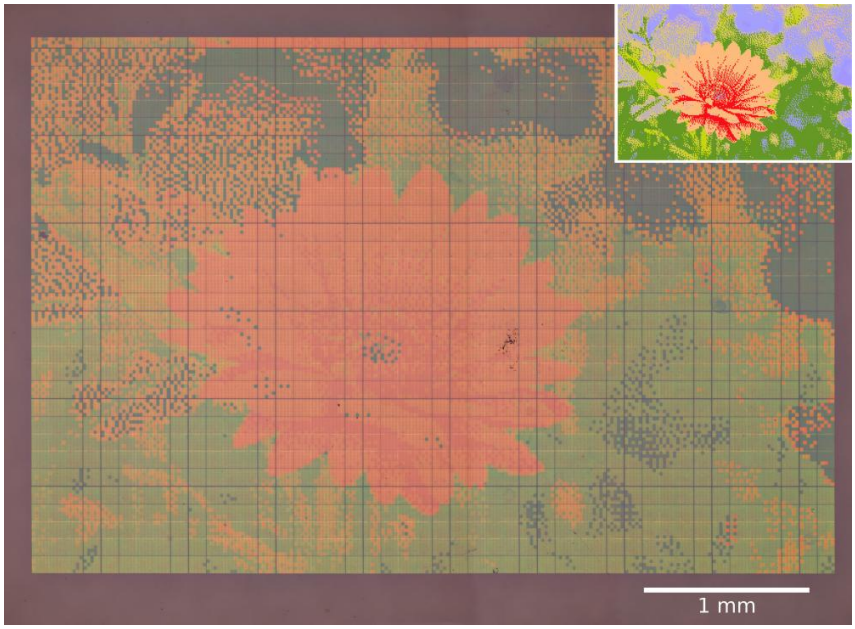

Figure 5.6 Large-scale plasmonic image, corner – template image used for exposure control, adapted from [128]

5.5 Plasmonic nanoantennas for structural colouring

The previous sections showed, that arrays of silver nanodisc naoantennas are useful for artificial surface colouring which served as an inspiration for exploring such effects little bit deeper with possible applications in the field of optically variable devices in anticounterfeit industry. Unfortunately, due to limited access to the variable pressure system, we have switched for conventional fabrication using conductive polymer in the following experiments. Most of the work that will be shown in the following section was done by my

bachelor student Petra Binková and published in her bachelor thesis 'Industrial applications of optical nanoantennas' [129], where my contribution was mostly in the supervision and design of the experiment ideas.

One of the largest problems that arose in the previous experiments was a poor chemical stability of fabricated structures. The silver is well known for its oxidation, that can completely destroy fabricated structures in a few days. In order to address this problem, several solutions were proposed:

- storing of fabricated samples under vacuum to avoid sample oxidation,
- sample bake-out in the nitrogen atmosphere – the main idea was that bake-out in nitrogen could help to purify silver which would lead to higher stability,
- covering the sample by 10nm thick layer of SiO_2 by atomic layer deposition,
- covering the sample by PMMA using conventional spin coating,
- switching over from silver to aluminium, which should provide similar optical properties, while being less sensitive to oxidation effects.

In order to quantify the sample degradation, we fabricated samples with arrays of silver plasmonic nanoantennas similar to the ones shown in fig. 5.2 and we periodically measured its transmittance spectra and observed the extinction. As the sample degrades, plasmonic effects fade away leading to a decrease of the extinction (increase of transmittance). The transmittance was measured at the resonance wavelength, which was identified from the spectra measured right after the sample fabrication. Fig. 5.7 shows the dependence of the sample transmittance on the time passed since the sample fabrication.

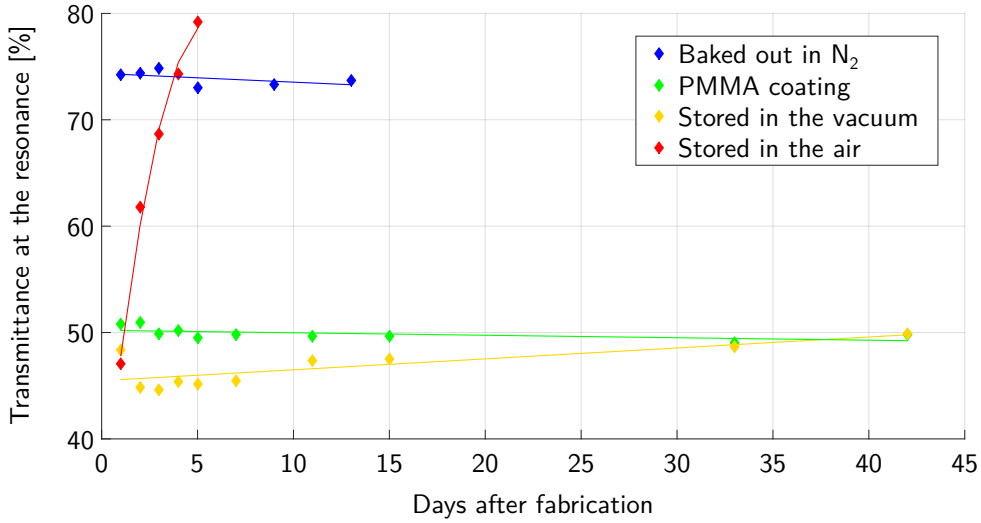

Figure 5.7 Dependence of the antenna transmittance at the resonance wavelength on time passed since sample fabrication (antenna diameter $d = 150$ nm, antenna pitch $2.5d$), adapted from [129]

We can see that the first proposed method – storing samples under vacuum (yellow line) helped to slow down the degradation process when compared to reference sample stored in normal conditions (red line), but still wasn't able to prevent it completely. We can also see, that the sample-bake out in nitrogen atmosphere was completely a failure as

the increased temperature speeded up the degradation process leading to the almost complete destruction of plasmonic effects. Even not shown in the figure, the result of ALD deposition was exactly the same, probably due to high temperatures during the ALD deposition process. The most successful method seems to be covering the sample by PMMA, which prevented the degradation of the silver structures. Unfortunately, as the index of refraction of PMMA is significantly higher than the index of refraction of the air, such a treatment leads to red-shift of the resonances of fabricated structures. Fig. 5.8 shows the difference in the transmission spectra of coated and uncoated samples with the red shift clearly visible.

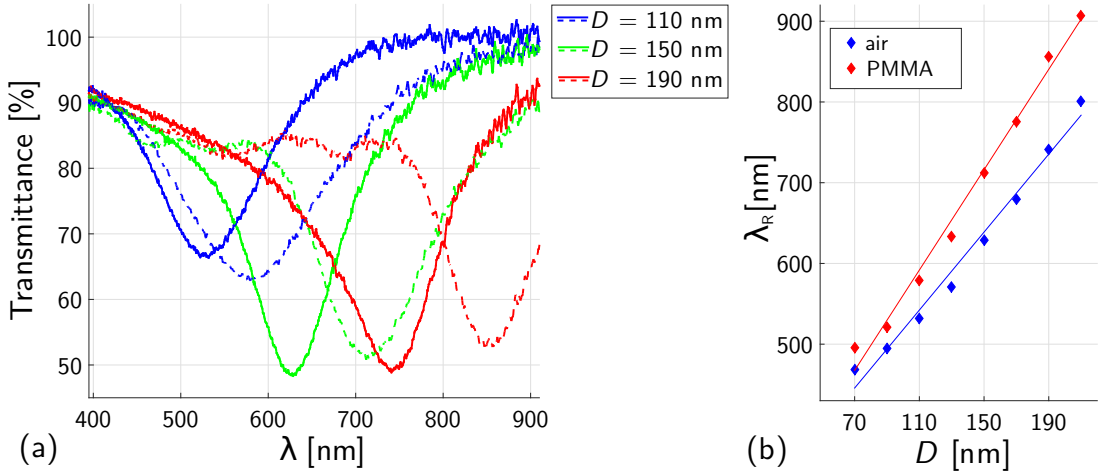

Figure 5.8 a) Transmittance spectra of antennas coated by PMMA (dashed) and uncoated (solid), b) dependence of the resonance wavelength on the antenna length for coated and uncoated samples, adapted from [129]

Other investigated structures were rectangular antennas. Such antennas have two main axes which lead to two different resonance wavelengths for two different linear polarizations. Consequently it is possible to simply switch colour effects by switching polarization of the illumination light. While this effect wasn't achievable with aluminum antennas, for silver antennas it proven to be feasible. Fig. 5.9a shows the spectra of the fabricated antennas. The antenna size a varied along its axis from 70 nm to 190 nm while keeping the second size b fixed at 150 nm. The antenna pitch was 2.5 times bigger than the antenna dimension in the corresponding direction. We can see, that when the sample is illuminated by polarization along the longitudinal axis, the observed resonant wavelength significantly varies with the a size, when the sample is illuminated with polarization along the fixed b axis, the observed resonance wavelength variations are much smaller. For completeness, fig. 5.9b shows resonances both for PMMA-coated and uncoated samples.

With the technology developed and demonstrated the next step was creation of an optical variable device (OVD) prototype that would utilize the studied plasmonic effects. The first sample was based on the rectangular antennas supporting two resonances at different wavelengths for two orthogonal polarizations. Fig. 5.10a shows the fabricated sample (BUT logo) illuminated by two orthogonal polarizations. We can clearly observe that for each of the two polarizations the area filled with plasmonic nanoantennas (background around T letter) exhibits different colour. Another sample was butterfly consisting

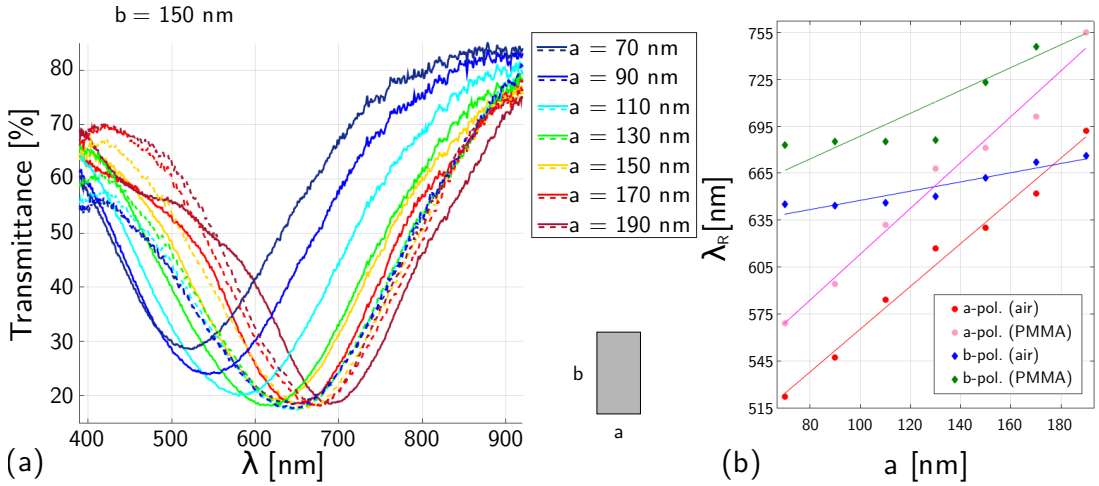

Figure 5.9 a) Transmittance spectra of uncoated rectangular nanoantennas illuminated by linearly polarized light along the two principal axes (solid curves – longitudinal axis, dashed curves – lateral axis) of the rectangle, b) dependence of the resonance wavelength on the antenna length for different polarizations and environment, adapted from [129]

of silver nanodiscs of different diameters in order to produce different colours. The outer contour was filled by nanodiscs with resonances in the infrared, looking white at perpendicular illumination, but serving as an diffraction grating producing various colours, when illuminated under different angles.

Figure 5.10 (a) prototype of OVD made of silver rectangular antennas illuminated by two different polarizations, (b) prototype of OVD made of aluminum nanodiscs illuminated under different angles, adapted from [129]

6 Plasmonic antennas for THz region fabrication

The following chapter describes experiments on fabrication of plasmonic antennas with resonances in THz region. The experiments were done as a part of the FET OPEN project 'Plasmon Enhanced Terahertz Electron Paramagnetic Resonance (PETER)'. The project aims at enhancement of the local magnetic field by concentrating electron current density using plasmonic antennas creating magnetic hot spots. Fig. 6.1 shows the proposed geometry of 'Diabolo' like antennas consisting of two triangular wings interconnected by a small bridge of width W and length G.

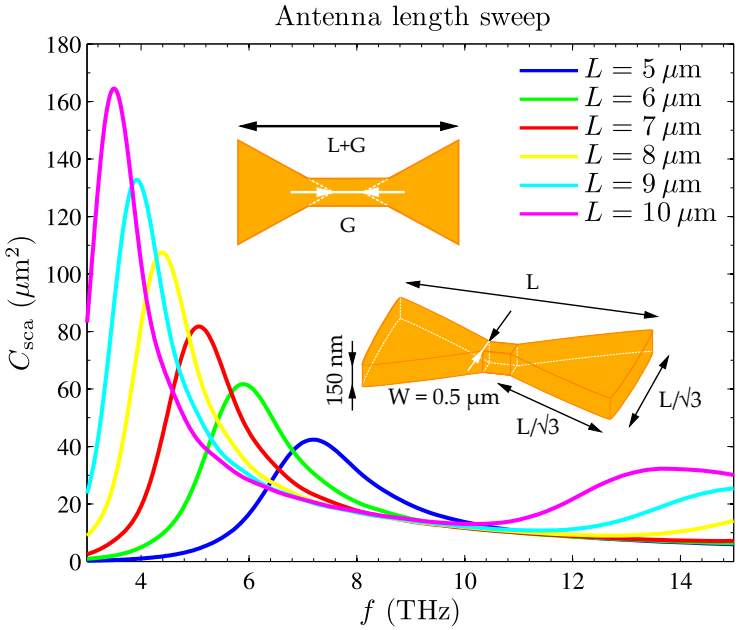

Figure 6.1 Proposed geometry of plasmonic antennas with resonances in the THz region, designed and calculated by Martin Hrtoň

As the required resonances lay in the region 210 – 490 GHz which requires structures too big to be easily calculated, the dimensions were extrapolated from calculations in the THz region, leading to L in the range 72 – 169 µm. Together with the samples for testing different antenna densities (pitch $1.5L$, $2L$ and $3L$) and bridge parameters, this resulted in total in 29 structures. Due to the THz spectrometer construction each structure has to be placed a on separate sample that must fit into a tube with a diameter of 5 mm. According to these specifications, the sample size was chosen as 3.2x3.2 mm^2 with the 1.3x1.3 mm^2 area filled by antennas in the center of each sample. Every sample has markings and identification QR code in corner. Fig. 6.2 shows the layout of fabricated samples taking one half of a 2 inch wafer (due to possibilities of fabrication failure each sample was fabricated two times – 58 samples with antennas + 4 blank samples as reference). For the wafer design, we have used the KLayout parametric cell system, which allows custom

Python scripts to be used for geometry generation using numeric parameters making the design easier (see appendix A) [130].

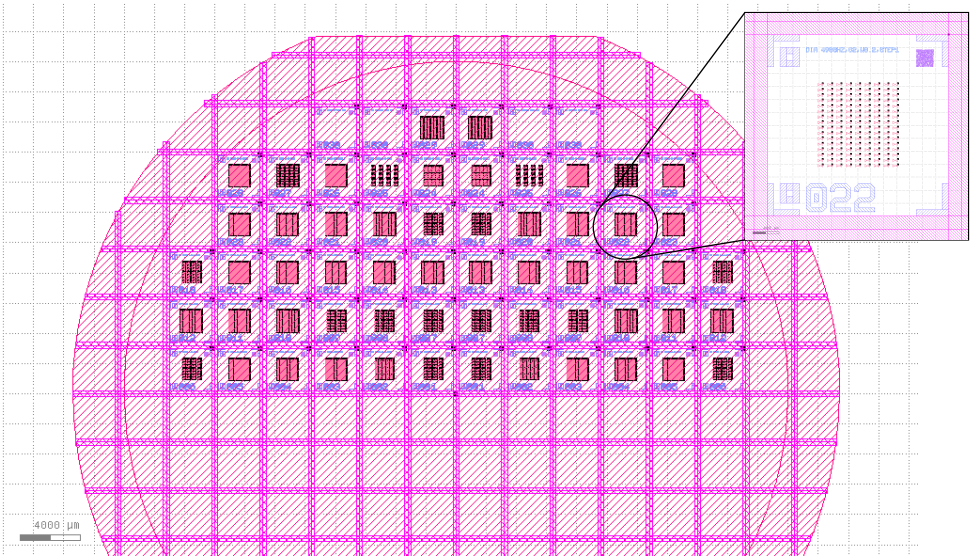

Figure 6.2 The layout of fabricated structures

As the expected working frequency is quite low for plasmonic antennas, and thus maintaining a dielectric (i.e. non-conductive) nature of the substrate is crucial for their correct function, the float zone [100] silicon with a resistivity of 300 – 500 Ω·cm was chosen as a substrate. The substrate was coated by a 230 nm thick layer of the poly-methyl metacrylate resist with the molecular weight 950 000 (3% solution in ethyllactate, 2000 rpm) and grooved using a UV laser (pink lines in fig. 6.2). The pattern was exposed using the RAITH 150 two e-beam lithography system. As the exposed area was large, lower acceleration voltage (10 kV) was selected in order to increase the resist sensitivity and achieve shorter write time. According to the previous test, the exposure dose was set to 100 µC/cm^2. The sample was developed in a methyl isobutyl keton-isopropyl alcohol solution (1:3) for 60 s and rinsed in isopropyl alcohol for 30 s. The fabrication was followed by deposition of a 3 nm thick adhesion titan layer and 150 nm thick layer of gold using an electron beam evaporator. The fabrication was finished by the lift-off process in N-methyl pyrolidinone heated up to 80 °C.

Fig. 6.3 shows a detail of fabricated structures. As the wafer was exposed in one run, the EBL system placed the individual write fields in a rectangular grid leading to some stitches between the fields being placed inside the structures. Although the calibration of the write field geometry was performed before the exposure it is noticeable, that the residual geometry errors were big enough to cause a gap in the fabricated structures. This probably happened as an effect of scanning system hysteresis as the actual geometry corrections that should be applied to the scanning system depend on the shapes to be written. Naturally, it makes absolutely precise correction for non-homogeneous patterns impossible. Another observable effect is an insufficient exposure dose in the bridge area of fabricated structures due to different relative pattern density and lower proximity effect in comparison to the wing area of the structure which even further worsen the stitch problems.

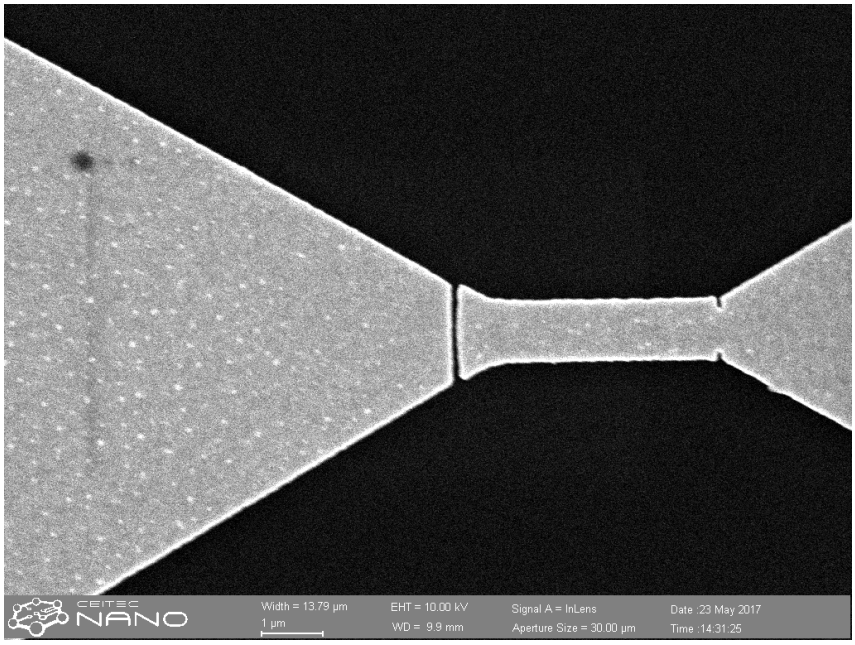

Figure 6.3 SEM image of fabricated structures showing a gap in the antenna

As the size of the individual antenna is smaller than the used write field, it should be possible to avoid any stitch artefacts by a precise placement of individual write fields. Unfortunately as the pitch of the antennas is different for each structure and not same in x and y direction, it is not possible to define any global setting that would achieve the desired write field placement. Luckily, the write process in the Raith system is governed by a position list – a simple text file describing positions on a wafer and corresponding structures (or a part of structures) that should be exposed there. It makes it theoretically possible to tailor the position list in such a way that each antenna is exposed by its individual write field. The position list is composed of lines describing each exposure task defined by several parameters, such as

- *U, V* – specifying the position of exposure in the Raith UV system,
- *Comment* – specifies the name of the top cell to be patterned,
- *Pos1, Pos2* – reference point in the structure to be placed at position defined by UV,
- *File* – path to the GDS file to be patterned,
- *Layer* – list of layers to be patterned,
- *Area* – the area of pattern to be written,
- *Time* – originally served probably for storage of time, in current version however serves as a bit field for storage of parameters like which type of objects (Areas, lines, Dots, FMBS objects) should be written and also determines if global exposure parameters, or parameters stored the in position list should be used,
- *Dwelltime, stepSize, SplDwell, SplStep, ...* – low level exposure parameters calculated out of the dose and beam current.

In cooperation with Jakub Sadílek, we have developed an add-on for KLayout GDSII editor, which allows to graphically define such an exposure strategy and generate the corresponding position list automatically. The main concept of our approach is dividing of

layers in the GDSII file into two categories – graphic layers, that describe the geometry to be patterned and technological layers describing the write field placement and technological parameters used for exposure. The graphical layer acts as a standard layer in GDSII containing shapes of structures. The technological layer includes only two types of objects – origin object (one per technological layer), which describes the point of layout, that should be mapped to $[0, 0]$ point of the Raith UV system, and exposure objects – rectangles marking areas to be exposed in the layout. When the size of the exposure object is smaller or equal the size of a single write field, the Raith system exposes the whole area as a single write field. When the area is larger, it is filled with a rectangular grid of write fields in the standard way. Moreover, each exposure object carries information about the graphic layers, that should be exposed by that object allowing both layer and spatial filtering of objects to be patterned. The both special objects were implemented as parametric cells using standard PCell API, which allows their easy visualization in the editor (see fig. 6.4). Thanks to the hierarchical nature of the GDSII format, the user can easily make rectangular arrays of exposure objects using AREF objects in the hierarchy. In addition, each technological layer carries information about the write field to be used for patterning and optical preset allowing these parameters to be automatically switched during exposure using corresponding position list commands.

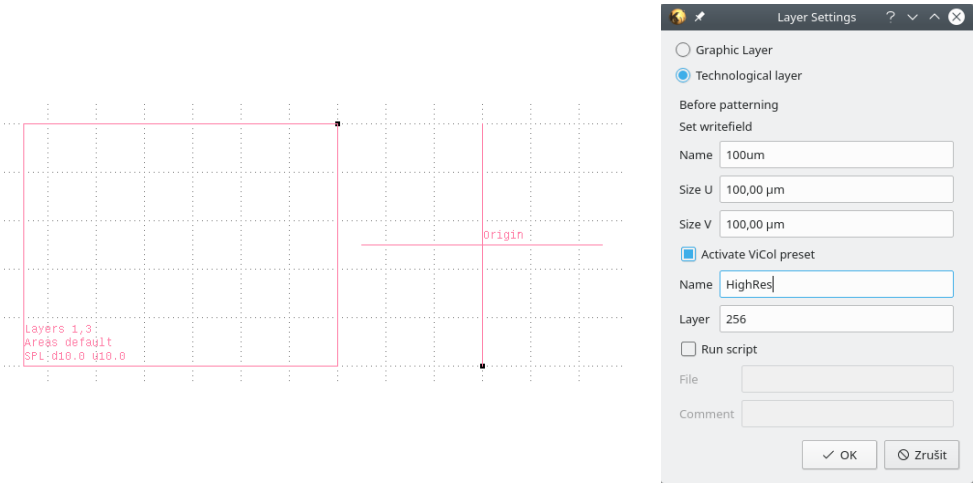

Figure 6.4 Left – exposure and origin PCell object, right – technological layer setup

In order to store these additional data into the GDSII file, the add-on creates service cell \$RaithKlayoutInfo and for each technology layer it creates a TEXT record there with all tech layer metadata serialized in the JSON format [131].

Unfortunately, the exposure parameters like the Dwell time and exposure step are also stored in the position list file. So, if the user wants to use different exposure parameters for a different technological layer, these parameters has to be calculated inside KLayout and stored to the position list file. In order to allow this, we have replicated the Raith dose calculator tool inside the KLayout editor (see fig. 6.5), which allows the user to assign a different exposure process to each exposure object or technological layer.

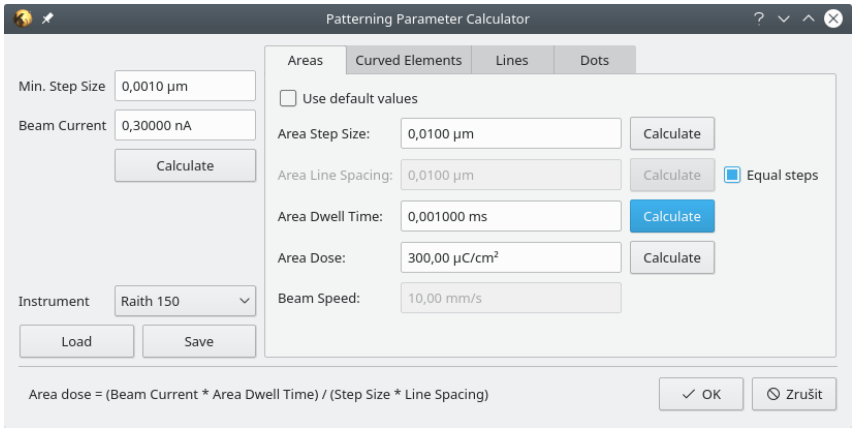

Figure 6.5 Raith patterning parameter calculator window recreated inside KLayout

The main function of the add-on is generation of the positionlist file. It allows user to select which technological layers should be patterned, flattens the exposure object hierarchy and generates the corresponding position list together with a command for write field and column preset switching.

In order to address the proximity effect related dose variation, a correction was done. The proximity effect correction consists of many different steps, that must be precisely performed in order to get accurate results. The first step of the correction was calculation of the beam point spread function using a Monte Carlo approach. The calculation was done using the GenISys Tracer software. We have set the later stack according to the previous experiment (bulk Si substrate and 230 nm thick layer of PMMA). Fig. 6.6 shows the cross section of the calculated point spread function in the middle of the PMMA layer.

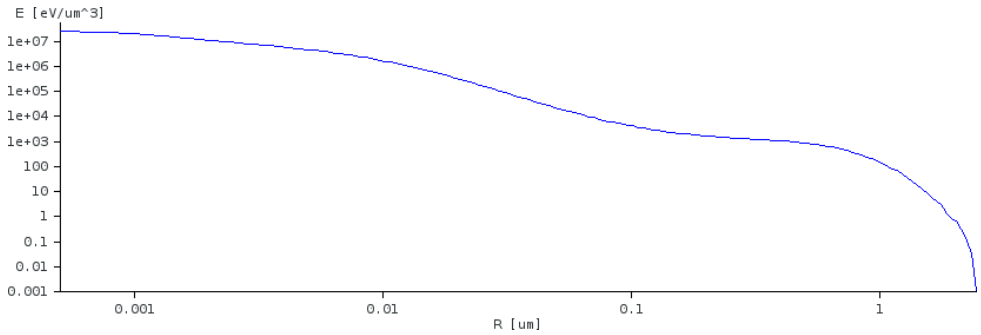

Figure 6.6 Calculated point spread function

However, as mentioned in section 3.1.4, all numerically calculated point spread functions need to be corrected for process blur. As the main manifestation of the proximity effect is change of the dimension of fabricated structures with different pattern densities, a special test pattern consisting of arrays of 200 nm lines with different pattern densities was corrected using a numerical point spread function and exposed by doses of 70–200 µC/cm^2 (see fig. 6.7).

After the exposure, the resulting pattern was imaged in order to obtain the dimensions of fabricated lines. Using the calibration tool of the Tracer software it is possible to calculate the process beam blur and optimal base dose. During the calibration process, the Tracer software simulates the developed resists profiles (performing deposited energy

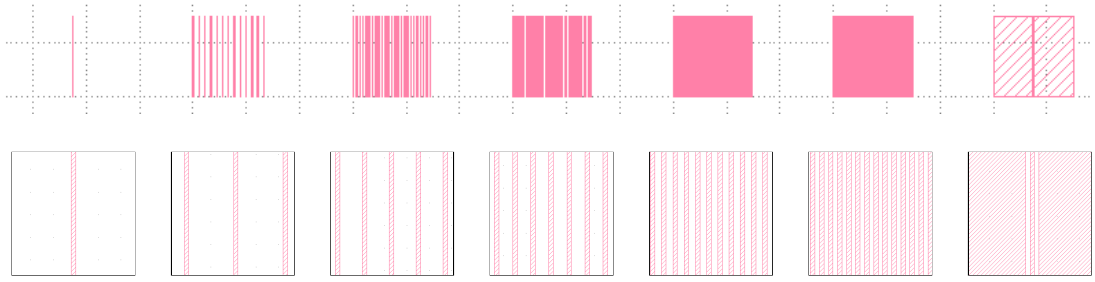

Figure 6.7 Top: test structures with the pattern density from 0% (left) to 100% (right), bottom: detailed images of each structure

density calculations) using the calculated point spread function for different beam blur and tries to fit this parameter to measured data. Another part of the calculation is a proposal of the optimal dose window, where the real dimensions of fabricated structures should follow dimensions defined by the structure design. Fig. 6.8 shows the results of the calibration – dependence of the critical dimension on the exposure dose for different pattern densities together with the fitted model.

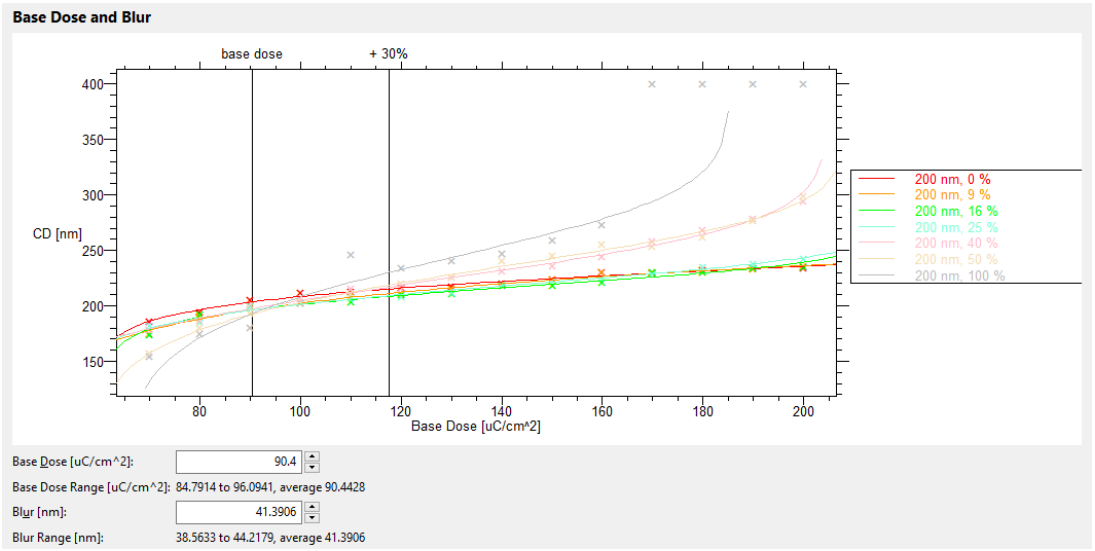

Figure 6.8 Dependence of the critical dimension on the exposure dose for different pattern densities

With the knowledge of the point spread function and process beam blur, the layout was proximity corrected using the GenISys Beamer software. As the pattern is very large and conventional correction consisting of flattening the whole design, calculating the correction and running heuristic algorithm to rebuild the hierarchical structure would take very long time, another approach was selected. The correction was done for every single type of the antenna geometry contained in the design one by one. In order to correct for spatial effects arising from the array nature of the pattern, periodic boundary conditions accordingly to the periodicity of each array were chosen. After the calculation of corrected antennas, corresponding cells in the design hierarchy were replaced by the corrected ones. Fig. 6.9 shows the data flow in the Beamer to achieve such a correction based on the replace_cell_by_pec macro, that does the correction for one antenna type.

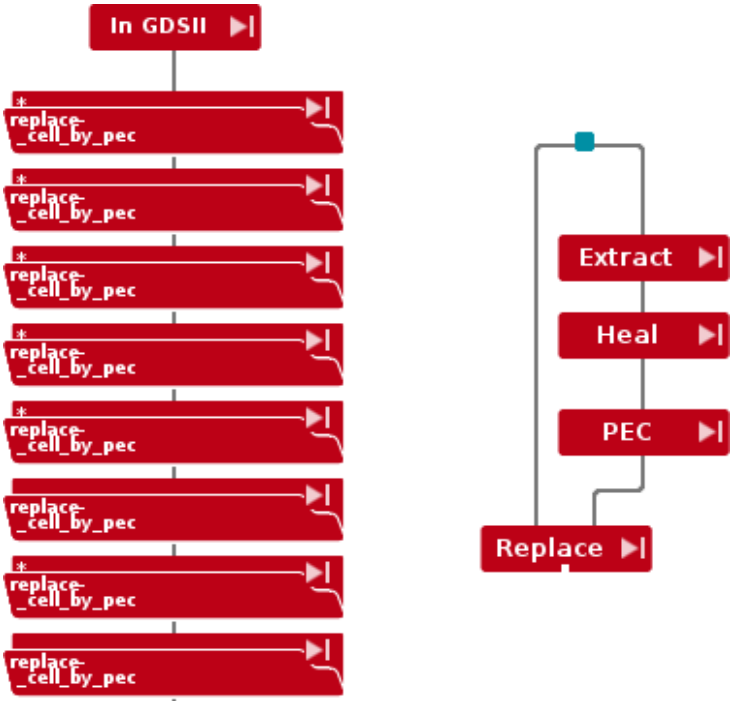

Figure 6.9 Left – Beamer flow for design processing, right – replace_cell_by_pec macro

After the correction and new write field placement strategy the fabricated samples no longer suffered from problems mentioned earlier.

7 Chracterization of plasmonic metasurfaces using digital holographic microscopy

Pasmonic metasurfaces, one of the most promising applications of plasmonic nanoantennas, are nowadays often based on alternation of the phase of the light by plasmonic nanostructures. In such a context the ability of quantitative imaging of the phase distribution becomes a crucial task for assessment of any engineered metasurface. Traditionally, accessing the phase information was done using Spectroscopic Ellipsometry [132]. Unfortunately, it is limited to some special cases and often requires inverse analysis. Another option is Differential Scanning Heterodyne Microscopy [133], but it provides only differential data making the analysis complicated. Experiments using a scattering type of Scanning Near Field Optical Microscopy have also been demonstrated [134], unfortunately the SNOM is very slow as it is a scanning probe technique and its spectral range covers the IR–THz region only. So far the interferometric approach seems to be the most promising and straightforward method, as it has been demonstrated by Genaro et al. [135]. However, their Spectral Interferometric Microscopy is a scanning technique and has limitations for dimensions of observed samples.

In such a context the digital holographic microscopy presents an attractive alternative for plasmonic metasurface characterization as it is capable of direct quantitative imaging of the phase distribution. This project was done in a cooperation with the Experimental biophotonics group at CEITEC which focuses on the development of digital holographic microscopy instruments, and my colleagues from the plasmonic group, who were of assistance during the measurements and built the theoretical background and associated calculations.

7.1 Characterization of plasmonic metasurfaces for non-polarized light using Coherence-controlled holographic microscopy

For our first experiments [136], we choose the Coherence-Controlled holographic microscope (see section 4.5.2) [137]. It is a digital holographic microscope operating in the visible range using non-polarized light. As it supports the use of non-coherent light, it offers a superior phase resolution with images not suffering by any coherence noise, or speckling[2].

The first experiment was done on a sample similar to that one presented in chapter 5. We have fabricated 10x10 µm^2 areas of golden plasmonic nanodiscs on a glass substrate. The disc diameter was $d = 30 - 190$ nm. In order to keep the fill-factor for different fields constant, the antenna pitch was chosen as $2d$. The layout of the sample is displayed in fig. 7.1. Each sample also contains reference structures. These structures simply consists

[2] based on J. Babocký, A. Křížová, L. Štrbková, L. Kejík, F. Ligmajer, M. Hrtoň, P. Dvořák, M. Týč, J. Čolláková, V. Křápek, R. Kalousek, R. Chmelík, and T. Šikola, ACS Photonics 4, 1389 (2017).

of squares with dimensions high enough to be out of resonance for visible light while they keep the same fill-factor as plasmonically active structures.

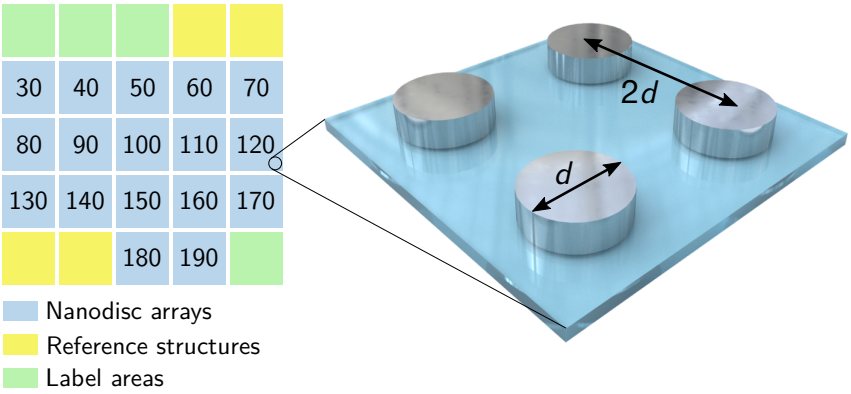

Figure 7.1 Sample layout, adapted from [136]

The fabrication itself was done by Electron Beam Lithography. We choose a 140 nm layer of PMMA as a resist. In order to make the substrate conductive, the conductive polymer Electra 92 was applied on the top of the resist layer. Structures were written by Tescan Mira 3 SEM with the Raith Elphy lithographic system at 30 kV. The sample was developed using a MIBK:IPA solution (1:3) for 60 s followed by rinsing in IPA for 30 s. The fabrication was finished by deposition of 40 nm of gold together with a 3 nm thick Ti adhesion layer and lift-off in acetone.

Fig. 7.2 shows a quantitative phase image of the fabricated sample while illuminated by white light with a red filter (650 nm).

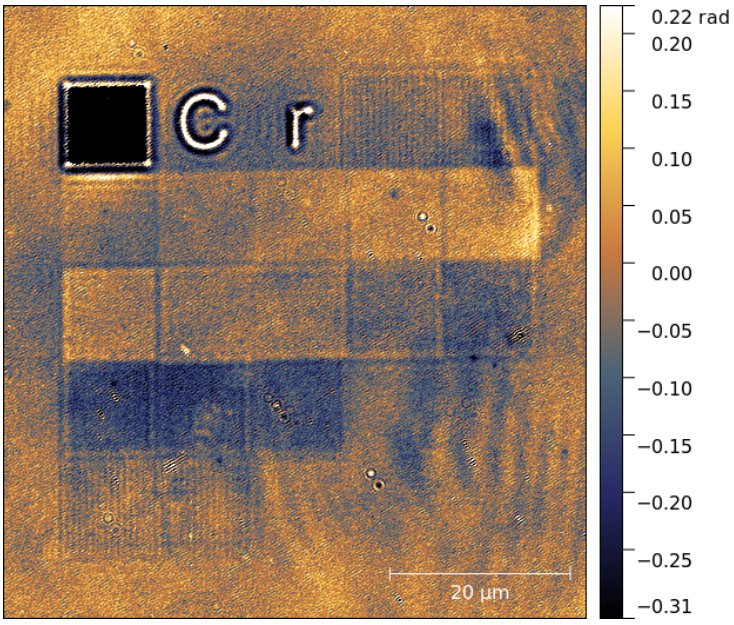

Figure 7.2 Phase image of gold nanodiscs illuminated by the non-coherent red light obtained by CCHM

It is obvious that at a diameter 110 nm there is a noticeable phase flip, where the phase rapidly changes from positive values to negative ones making clear our plasmonic nanostructures alter the phase of the transmitted light.

For better understanding of the phase effects arising in the disc nanoanttennas, several changes for the following experiments were done. At first, we have decided to replace the gold with silver as for golden nanodiscs the resonances are mostly in the near infrared region, while similar structures fabricated of silver provide resonances at visible wavelengths (wavelengths the microscope is designed for). We have also done slight changes to the sample layout sacrificing labels and reference structures (that have not found any use anyway) for getting 4x4 arrays of plasmonic nanodiscs with diameters in a range of 50 – 200 nm. We have also increased spacing between fields which helped with background subtraction during quantitative image processing. In order to be able to perform wavelength-resolved imaging of plasmonic nanoantennas, we have upgraded the microscope with a supercontinuum light source (Fianium WhiteLase) and acusto-optical tunable filter. While this modification adds coherence noise to the image, leading to the need for flat field correction, it allows to illuminate the sample with a selected wavelength. Unfortunately, the control software supplied with the device seemed not to work with current version of Microsoft Windows, which led us to the development of the custom control software RainbowLase (see fig. 7.3).

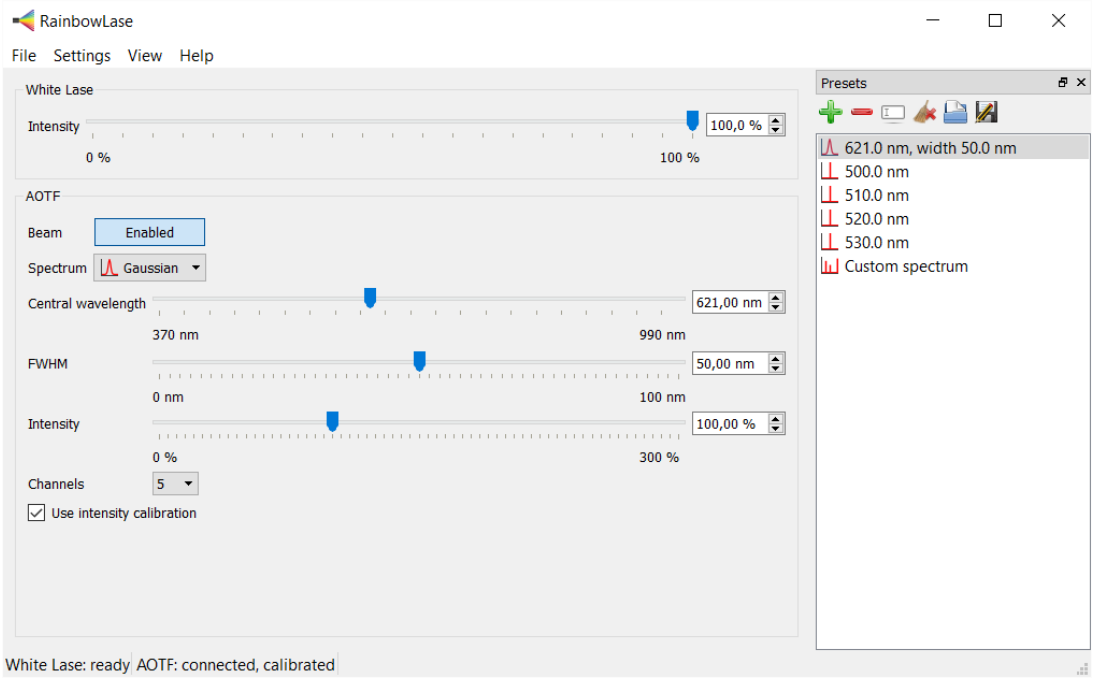

Figure 7.3 RainbowLase control software

To make sure the resonances of fabricated structures are situated in the visible range, we have characterized the sample using optical spectroscopy. Fig. 7.4a shows extinction spectra of fabricated antennas for different antenna diameters (the first number denote the designed diameter, second one – in the parentheses the real diameter of fabricated antennas obtained from SEM images). We can observe, that our fabricated structures

exhibit clear localised surface plasmon resonnaces in the range 530 – 700 nm that red shift with an increased diameter. Note, that the spectra from antennas with diameters 50 nm and 60 nm are not included here as their fabrication was not successful. The measured spectra were also verified using finite difference time domain simulations performed by Martin Hrtoň. Fig. 7.4b shows the spectra obtained by the simulations. The red shift of experimentally measured spectra with respect to calculated ones was probably caused by thin layer of oxide formed on the top of fabricated nanoantennas.

The next step was an actual imaging using Coherence-controlled holographic microscope. After the installation of the laser source into the microscope, it was necessary to defocus the condenser in the Köhler illuminator as the microscope is designed to work with non coherent area source produced by halogen bulb light guided through a thick bundle of multi-modal optical fibers and our laser source produced only a small bright spot in the center of the view field. During the measurement, we have acquired set of multiple images of the fabricated structure for different wavelengths (500 – 770 nm) of the illumination light. We have also acquired a set of background images from an area without antennas, that were subtracted from the images of the structure to compensate the coherence noise arising from parasitic interferences in the optical system (flat field correction). All acquired holograms were reconstructed using the Kreis method [125] by algorithm embedded in the microscope control software. Fig. 7.4c shows some examples of acquired images. We can clearly observe that similarly to the previous measurement, when the antennas are at resonance, the phase of the transmitted light rapidly flips from negative to positive values. We can also observe, that closer the antennas are to the resonance, the more intense noise effect can be observed inside the field. The main origin of this effect is imperfection of the antenna fabrication, where even small differences in the antenna sizes can be visualized in their phase response upon the resonance.

For better visualization of the phase dependence, we have extracted the phase values from each image and plot the dependence of the phase of transmitted light on the illumination wavelength for different antenna sizes (phase spectra) in fig. 7.4d. Apparently, the phase measured by CCHM exhibits an S-shaped flip from positive (above the resonance wavelength) to negative values (below the resonance wavelength) and goes to zero in both regions far from the resonance. Such a behavior seems to be inconsistent with the classical resonator theory, where we would expect the phase to go monotonously from 0 to π with $\frac{\pi}{2}$ at the resonance. The main reason of these discrepancy is the fact that in our measurements the microscope measures the superposition of the phase of the original driving field and of the field scattered by plasmonic nanoantennas that will be called in the further description as the total field phase.

Fig. 7.5a demonstrates the formation of the total field phase in the phasor representation. The reference phasor $\vec{E}_{\mathrm{ref}}$ serves in the model as a fixed reference. The $\vec{E}_{\mathrm{dr}}$ represents the driving field, which is shifted by some background value φ_{bg}, that is usually removed by the flat field correction. Plasmonic antennas create the scattered field $\vec{E}_{\mathrm{sca}}$ that lags behind the driving field by φ_{sca}. The total field measured by the CCHM $\vec{E}_{\mathrm{tot}}$ is simply $\vec{E}_{\mathrm{tot}} = \vec{E}_{\mathrm{dr}} + \vec{E}_{\mathrm{sca}}$. With the knowledge of the total field formation, we can simply derive the total field phase profile (fig. 7.5c) from the phase profile of the scattered field and the ratio between the driving and scattered field, that can be easily calculated using the finite difference time domain method (fig. 7.5b).

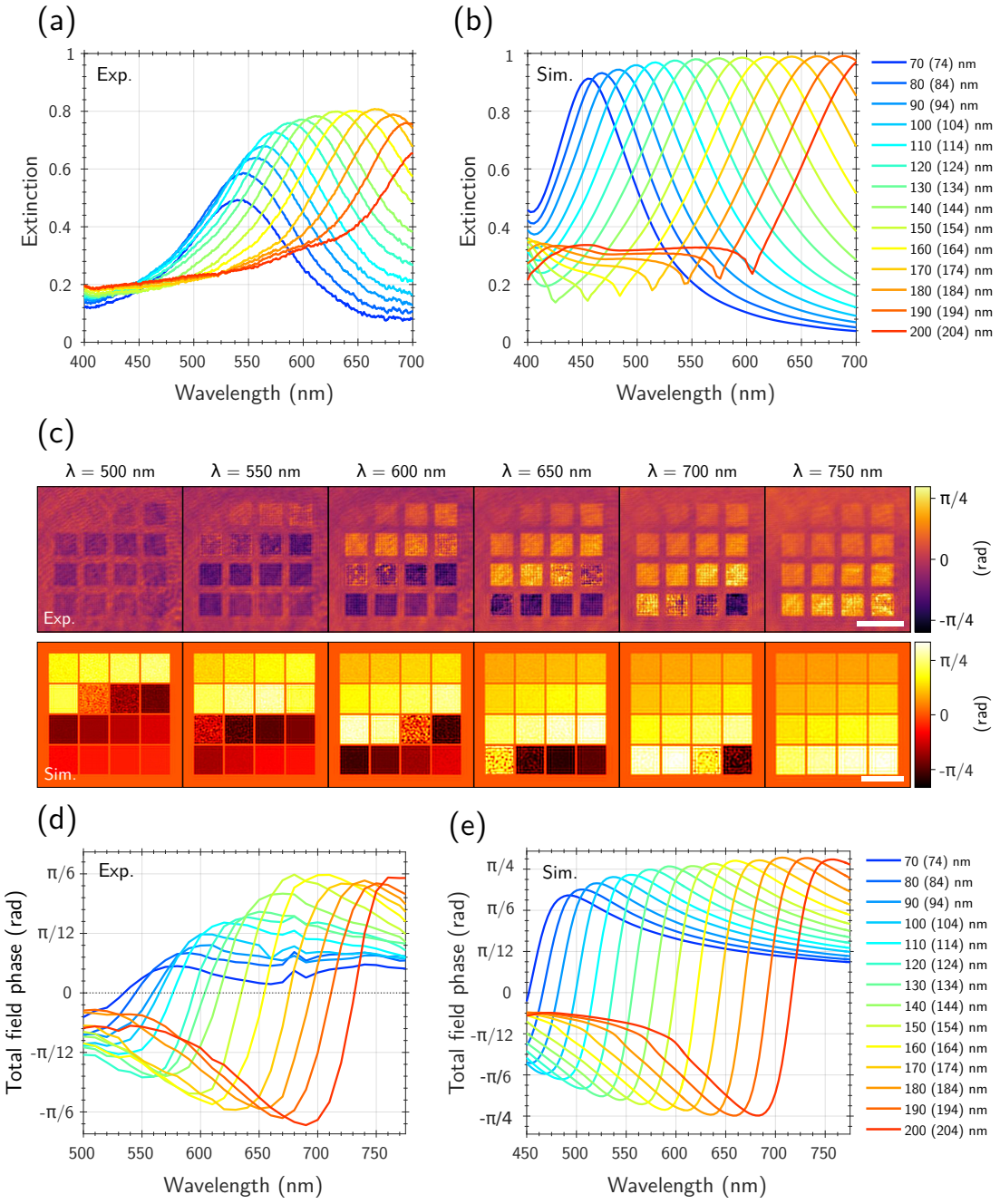

Figure 7.4 (a) Experimental and (b) FDTD-calculated extinction spectra of silver nanodisc arrays on glass. Both show characteristic plasmon resonances. The experimental extinction in (a) has been calculated as T/T_{REF}, where T is the transmission through the nanodisc array and (T_{REF}) the transmission through the bare substrate. (c) Quantitative phase images of silver nanodisc arrays at a selected subset of illumination wavelengths, measured in CCHM (top) and theoretically calculated (bottom). The scale bars are 20 µm. (d, e) Spectra of the total field phase at nanodisc arrays of various dimensions extracted from the full set of measured CCHM images (d) and from numerical simulations (e), adapted from [136]

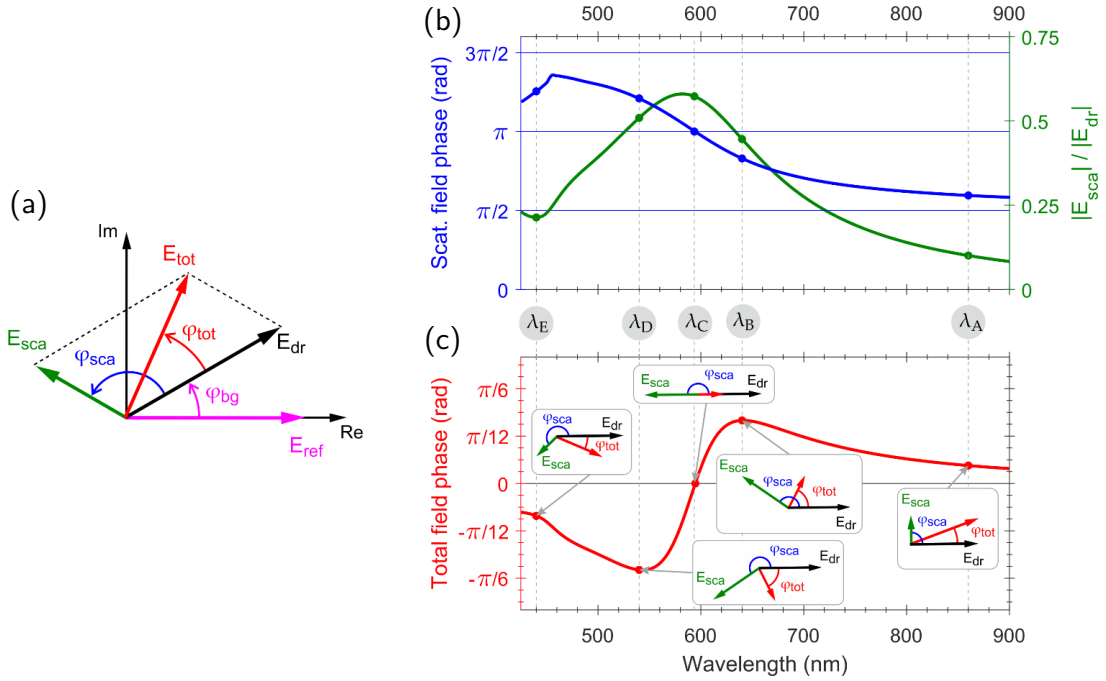

Figure 7.5 (a) Phasor diagram of the fields forming the signal measured in CCHM. Note that we follow a convention where a phase shift in the counterclockwise direction represents a phase delay. The field that drives the plasmonic structures is denoted as $\vec{E}_{\mathrm{dr}}$ and it is phase-shifted with respect to the reference field $\vec{E}_{\mathrm{ref}}$ by φ_{bg} due to an inevitable path difference between the sample and reference arms. The field scattered by nanodiscs ($\vec{E}_{\mathrm{sca}}$) lags behind the driving one by an angle φ_{sca}. The total measured field $\vec{E}_{\mathrm{tot}}$ is the sum of $\vec{E}_{\mathrm{dr}}$ and $\vec{E}_{\mathrm{sca}}$, and its phase shift φ_{tot} with respect to the driving field is the ultimate quantity measured in CCHM. (b) Calculated scattered field phase (blue) and amplitude (green) spectra for the 154 nm nanodiscs; the values of the amplitude and phase at selected wavelengths $\lambda_{\mathrm{A}} - \lambda_{\mathrm{E}}$ (labeled by dots) are used in (c) to elucidate the total field phase formation using phasor diagrams. (c) Calculated phase spectrum of the total field resulting from the superposition of scattered and driving fields (with the superposition of phasors sketched in the boxes), adapted from [136].

The phasor analysis allowed us to numerically calculate the expected total field phase profiles displayed in fig. 7.4e and expected phase images for different wavelengths (fig. 7.4c), which both show a very good match with the measured data.

As the coherence-controlled holographic microscope is equipped with a precise piezo stage allowing acquisition of z stacks, the next experiment focused on the acquisition of three dimensional field profiles produced by a metasurface. In order to demonstrate the ability of three dimensional imaging, we have fabricated a focusing plasmonic metasurface based on the principle of a zone plate with zones filled by disc nanoantennas (diameter 130 and 190 nm) producing negative or positive phase shifts (see fig. 7.6a). The zone plate was designed to operate at 650 nm (red light) with a main focal length of 100 µm. To image the field above the zone plate, we have used the coherence controlled holographic microscope with a tunable laser. Later, we have found that the defocusing of condenser lenses in the illuminator also provided plane wave illumination that made the imaging

way easier. A series of images which varied by the objective focus was acquired. The step in the focus was 1 µm leading to focus in the range 0 – 200 µm above the sample surface. With this experiment, we have to switch from hologram reconstruction using the internal microscope control software to Holom software developed by Matěj Týč as the internal reconstruction algorithm designed primarily for biological data was unable to correctly unwrap the phase of the observed image. The Holom software allowed us to employ a custom unwrap method, where the standard processing was done as the first step to obtain the parameters of the compensation surface that needs to be subtracted from the unwrapped phase data. As the unwrap technique would fail and our data were in fact in a range that did not need any unwrapping, we have then wrapped the compensation surface and subtracted it from the wrapped data instead. This operation produced compensated but not unwrapped phase data that were just adjusted in order to center the histogram of the phase image in the center of the $-\pi$, $+\pi$.

Fig. 7.6b shows the phase profile in the space above the zone plate, fig. 7.6c shows the cross section of the phase profile in the xz-plane. From the phase profile we can clearly observe the formation of the main focal point at $z = 100$ µm together with some of the minor focal points. Their positions, however, do not coincide with those of an ideal zone plate (e.g., the secondary focal point should be situated at one-third and not at one-half of the zone plate focal length). We ascribe this discrepancy to the fact that the field distribution produced by our nanodiscs does not fully match the one from the design. More specifically, the transition between the neighboring zones is not abrupt but gradual which makes them effectively narrower. Fig. 7.6d shows the same cross section obtained from the theoretical framework discussed above by the real nanodisc distribution as the calculation input.

In conclusion, we have demonstrated that the coherence-controlled holographic microscopy is a robust wide field imaging technique that can be used for plasmonic metasurface characterization and analysis of their optical effects.

7.2 Characterization of geometrical phase metasurfaces using Coherence-controlled holographic microscopy

In the following research [138], we have focused on extension of the previously mentioned technique for characterization of metasurfaces based on geometrical (Pancharatnam-Berry) phase [139, 140]. The geometrical phase metasurfaces employ simple rectangular dipole nanoantennas that convert circularly polarized light of one helicity to light with opposite helicity. The phase difference between the input beam and opposite helicity beam can be simply tailored by the orientation of these antennas as the phase can be described by

$$\varphi = 2\sigma\theta, \tag{7.1}$$

where θ is the antenna orientation with respect to some reference (in our case x axis) and σ is the factor describing the light helicity ($\sigma = 1$ for right hand helicity and $\sigma = -1$ for

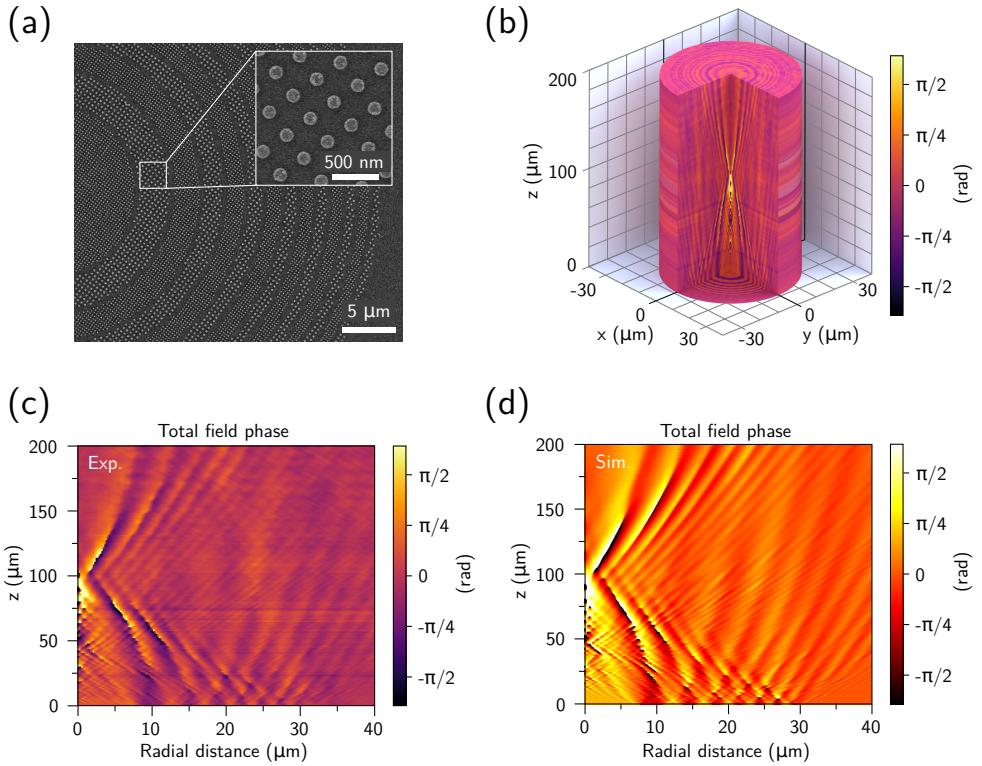

Figure 7.6 (a) SEM micrograph of the fabricated zone plate where individual zones are formed by silver nanodiscs (130 and 190 nm). (b) 3D visualization of the measured total phase distribution in the half-space above the plasmonic zone-plate. Measured (c) and simulated (d) phase map in the xz-plane above the zone plate where the main ($z \approx 100$ µm) and subsidiary ($z \approx 50$ µm, $z \approx 25$ µm) focal points are clearly distinguishable close to the zero radial distance, adapted from [136].

left hand helicity). Such a system allows any phase distribution in the sample plane to be encoded into orientation of these antennas[3].

As the coherence-controlled holographic microscope is designed to work with non-polarized light and the efficiency of the geometrical phase metasurface is low, we have done some modification to the CCHM setup to make characterization of these metasurfaces possible. Fig. 7.7 shows the modified setup.

The object arm of the microscope was modified by addition of a linear polariser and quarter wave plane in the illuminator part, which together create left handed circularly polarized light for the sample illumination. In the detection part, we have added another quarter wave plate followed by a linear polariser in a such configuration that suppresses the driving left handed light leaving only the right handed light created by studied metasurface. The reference arm had to be modified as well by a linear polariser oriented in such way to match with the expected polarization of the microscope diffraction grating. The last part was a neutral density filter, which helped to match the intensity in the object arm in order to enhance the contrast of the interference stripes observed by a camera.

[3] based on A. Faßbender, J. Babocký, P. Dvořák, V. Křápek, and S. Linden, APL Photonics 3, 110803 (2018).

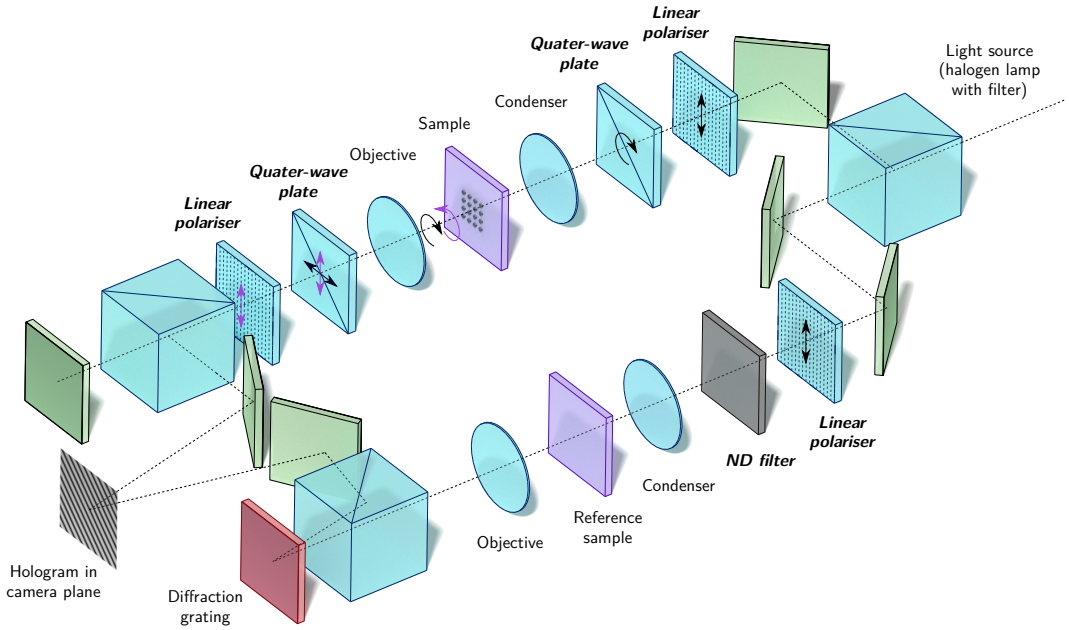

Figure 7.7 Coherence-controlled holographic microscope setup modified for the geometrical phase based metasurface characterization, added components are highlighted by the bold text

To test our imaging setup, we used a sample provided by our colleagues from the University in Bonn, which was a Laugerre-Gaussian geometrical phase metasurface producing an optical vortex beam out of a Gaussian beam and consisting of antennas providing phase differences in the full $0 - 2\pi$ range. Fig. 7.8 shows the quantitative phase image obtained by the CCHM. As we can see, in contradiction to our expectation, the phase distribution does not cover the full 2π range but it is limited to 1 rad. This indicates that due to adjustment imperfections and depolarization inside the microscope some of the driving field leaks into the resulting signal, creating once again the total field image. In this case, we have decided to try to reconstruct the scattered field only. From the phasor diagram (fig. 7.5a) we can see that the total field is a vector addition of the driving field and the scattered field. Luckily, where there is no metasurface, the measured image is the driving field alone. In such a situation it is possible to acquire the background image, reconstruct its hologram as usual, and create complex amplitude data out of the compensated phase and amplitude images. The subtraction of such a complex amplitude image of the metasurface total field and a background image (driving field image) provides a complex amplitude of the scattered field only from which the phase of the scattered field can be simply extracted. Fig. 7.9 shows the reconstructed scattered field of the inspected metasurface. Now it is obvious, that the observed image displays the scattered field only covering the whole 2π range.

In conclusion, we have demonstrated that with a small modification of the CCHM setup, it is possible to analyse the phase profile of metasurfaces based on the geometrical phase principle and reconstruct the scattered field out of the total field image, thanks to the fact the digital holographic microscopy provides complete holographic information about the observed sample.

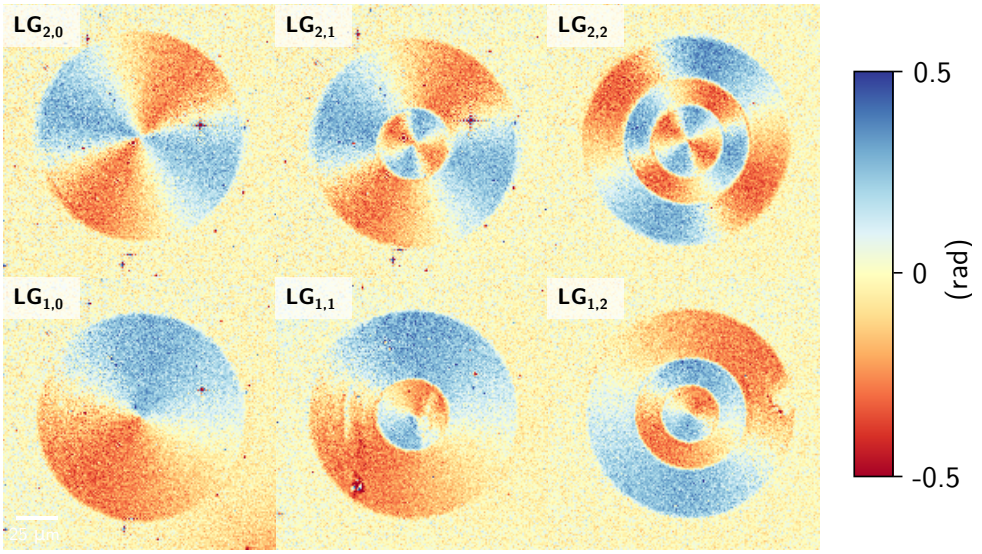

Figure 7.8 The raw (total field) phase images of the geometrical phase metasurface observed by CCHM, the indexes mark the corresponding Laugerre-Gaussian mode

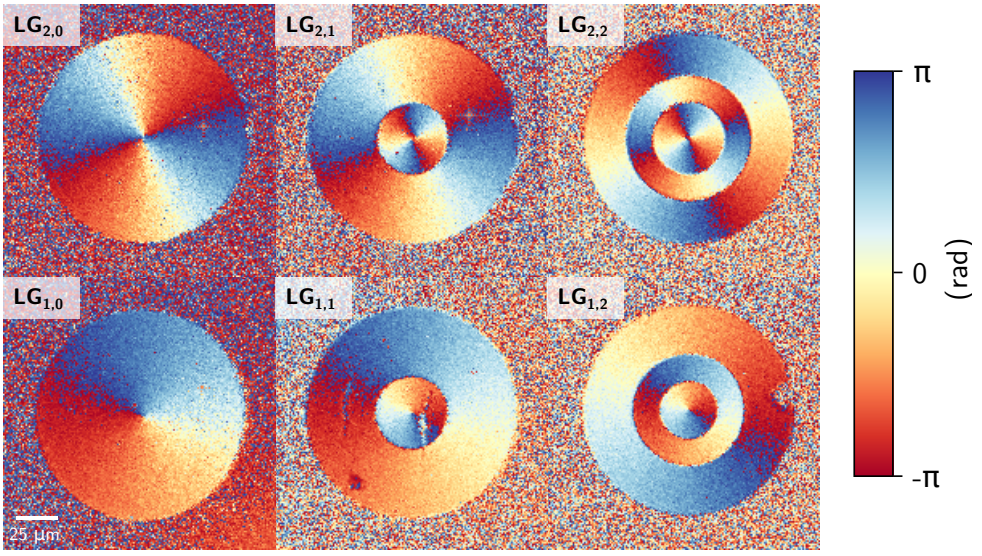

Figure 7.9 The reconstructed scattered field phase metasurface images, the indexes mark the corresponding Laugerre-Gaussian mode

7.3 Characterization of plasmonic metasurfaces using Quantitative 4G Optical microscopy

As the characterization of geometric phase metasurfaces using Coherence controlled holographic microscopy is quite complicated for the next experiments [141], we have switched to the Quantitative 4G optical microscope (Q4GOM) that was recently developed by our colleague Petr Bouchal [142]. The microscope is currently implemented as an add-on module for a conventional reflection optical microscope (see fig. 7.10). The light entering

the optical system passes through a linear polariser and quarter wave plate which produces circularly polarized light. Such a light then illuminates the sample surface, which in our case produces circularly polarized light with opposite helicity to the driving field. Both beams (driving and scattered) travel through the same optical path to the add-on module, where they are separated by a liquid crystal based metasurface diffracting the right handed and left handed polarized light into two different directions. Both beams are then converted to linearly polarized light using a linear polariser and targeted towards a camera, where they interfere in off-axis configuration in the similar way as in the Coherence-controlled Holographic microscope. The driving field serves as the reference and the scattered light from the sample as the signal. As both beams travel the same optical path, the interference is perfectly adjusted with no need to do any complicated optical path matching between the signal and reference arm as in the case of CCHM. The recorded hologram can be than numerically reconstructed using standard off-axis hologram reconstruction methods[4].

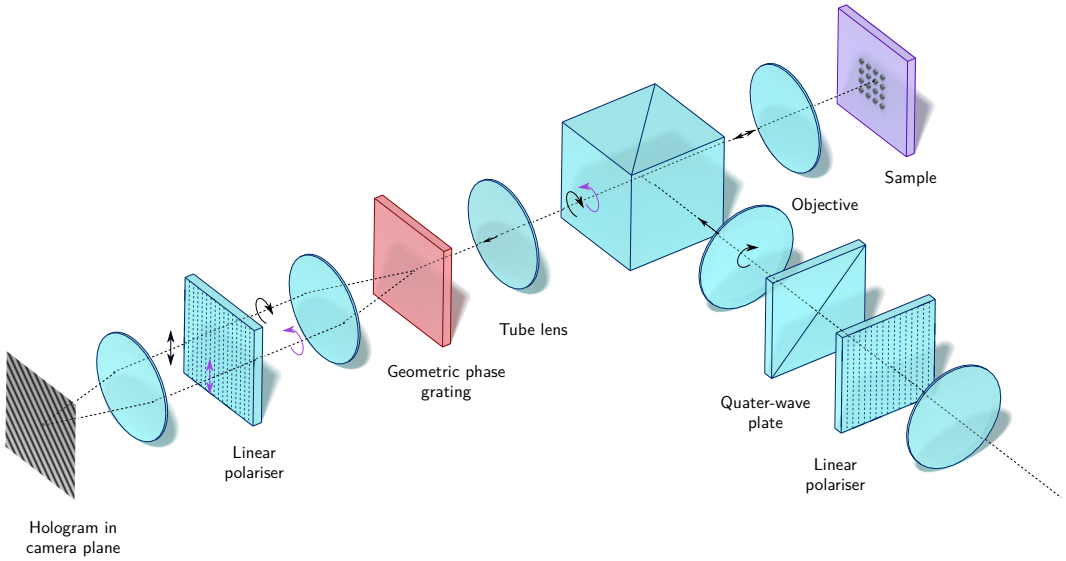

Figure 7.10 The Quantitative 4G Optical microscope

As the first experiment we have decided to start with a simple benchmark sample – arrays of dipolar plasmonic nanorods (width 80 nm, length 200 nm and thickness 30 nm) on a silicon substrate covered by a golden mirror layer and SiO_2 spacer (see fig 7.11a,b,c). The orientation of the nanorods was chosen according to the geometrical phase theory in order to produce phase shifts in the whole 2π range. The sample fabrication started by evaporation of 200 nm thick golden layer, that serves as a mirror. The fabrication followed by evaporation of a 110 nm thick SiO_2 spacer that should provide a dielectric transparent substrate for the nanorods. The nanorods were fabricated using electron beam lithography. In order to increase the resolution, we have switched to a 125 nm thick

[4] based on P. Bouchal, P. Dvořák, J. Babocký, Z. Bouchal, F. Ligmajer, M. Hrtoň, V. Křápek, A. Faßbender, S. Linden, R. Chmelík, and T. Šikola, Nano Lett. 19, 1242 (2019).

layer of the CSAR 62 resist (Allresist AR-P 6200.07, 4000 rpm). As the underlying SiO_2 layer is not conductive, and even small charging could lead to beam placement errors, we have covered the sample by the Electra 92 conductive polymer (Allresist AR-PC-5090). All structures were proximity corrected using the GenISys Beamer software and exposed using the Tescan Mira SEM with the Raith Elphy lithographic system. The beam energy was set to 30 keV, the base exposure dose was 110 µC/µm^2. Samples were developed in an amyl-acetate developer (Allresist AR 600-546) for 60 s and rinsed in isopropyl alcohol for 30 s. The fabrication was finished by deposition of a 3 nm Ti adhesion layer, 30 nm Au, and lift-off in Dioxolane (Allresist AR-P 600−71).

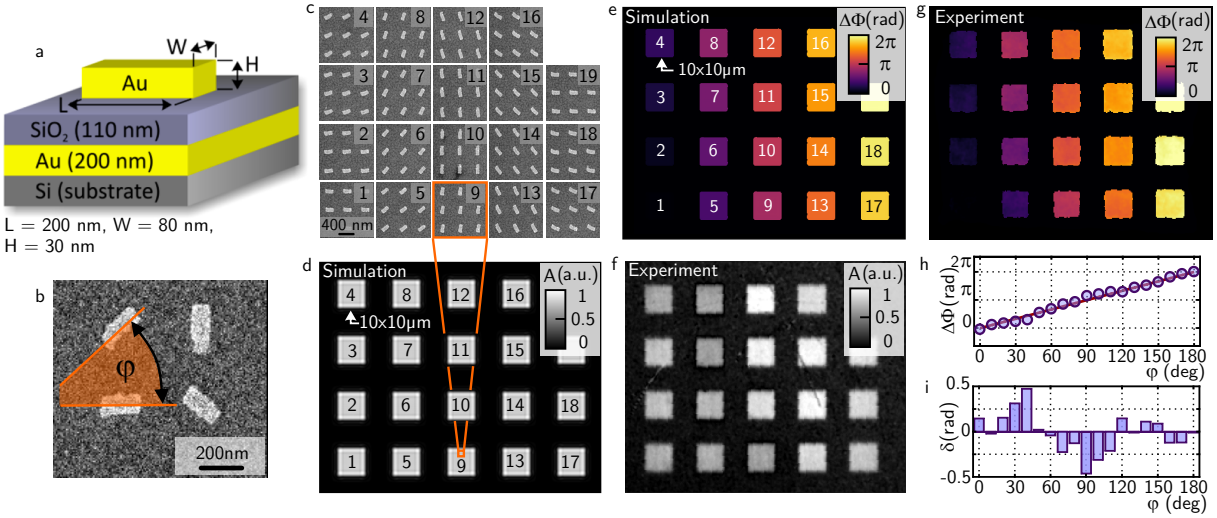

Figure 7.11 Phase imaging of the benchmark sample. (a) Schematic illustration of a single nanoantenna. (b) SEM image of the nanoantennas with varying angular orientation. (c) Enlarged parts of SEM images showing the orientation of the nanoantennas in individual areas of the benchmark test. (d) Simulation of the amplitude of light scattered by the benchmark sample. (e) Simulation of the phase response of the benchmark sample. (f) Amplitude and (g) phase image of the benchmark test restored from correlation records acquired by Q4GOM. (h) Theoretical dependence of the geometric phase on the rotation angle of nanoantennas (solid line) and values of the phase measured in individual square areas of the benchmark test (circles). (i) Differences between theoretical dependence and values of the phase measured in individual square areas of the benchmark test, adapted from [142].

The fabricated sample was imaged by Q4GOM using the Nikon 10×, NA = 0.3 objective. Fig. 7.11 shows the reconstructed amplitude (f) and phase (g) image. We can see, that according to our expectations, the phase delay increases linearly with the antenna angle φ. During the processing of experimental data, the background noise in the phase image was suppressed by a binary mask created from the measured amplitude. One of the largest advantages of the Q4GOM, is that it measures directly the phase difference between the driving and scattered field making the result interpretation straightforward without the need for any complex processing. Our experimental results were compared with numerical FDTD calculations shown in fig. 7.11d,e. Fig. 7.11h displays the dependence of the observed phase $\Delta\Phi$ on the antenna orientation φ, that was extracted from the acquired

images together with the model (solid line). Fig. 7.11i shows the difference between the model values and the values measured by the microscope. The biggest deviations of the measured phase from the theoretical values occur for the nanoantenna angles $\varphi = 40°$ and 90° and correspond to 0.5 rad. We assume that the deviations have their origin in manufacturing imperfections and sensitivity of the metasurface to a polarization ellipticity of the driving field rather than in the measurement accuracy.

The next experiment focused on exploration of the lateral resolution achievable by the Q4GOM for the metasurface characterization. Several special metasurfaces for its characterization consisting of binary gratings filled by nanorod antennas that produce the zero ($\varphi = 0°$) and π ($\varphi = 90°$) phase shifts in the neighbouring stripes were fabricated. The spatial frequency varied from 179 lines/mm to 1250 lines/mm. Fig. 7.12 shows the images of the gratings with a spatial frequency 364 lines/mm (a,b,c) and 883 lines/mm (d,e,f). The gratings were imaged by Nikon 10×, NA=0.3 (a, d) and Nikon 100×, NA=0.9 (b, e) objectives. Fig. 7.12 c, f shows the cross section profiles of the imaged phase grating. It is evident, that the insufficient resolution of the 10× objective resulted in the errors in the phase image with higher periodicity, while the 100× high NA objective managed to correctly display the observed sample. The experiments using low- and high-spatial frequency metasurface gratings prove that Q4GOM allows the quantitative measurement of the phase realized with the high aperture objective, while keeping the highest demands on the ground-truth accuracy of the phase image.

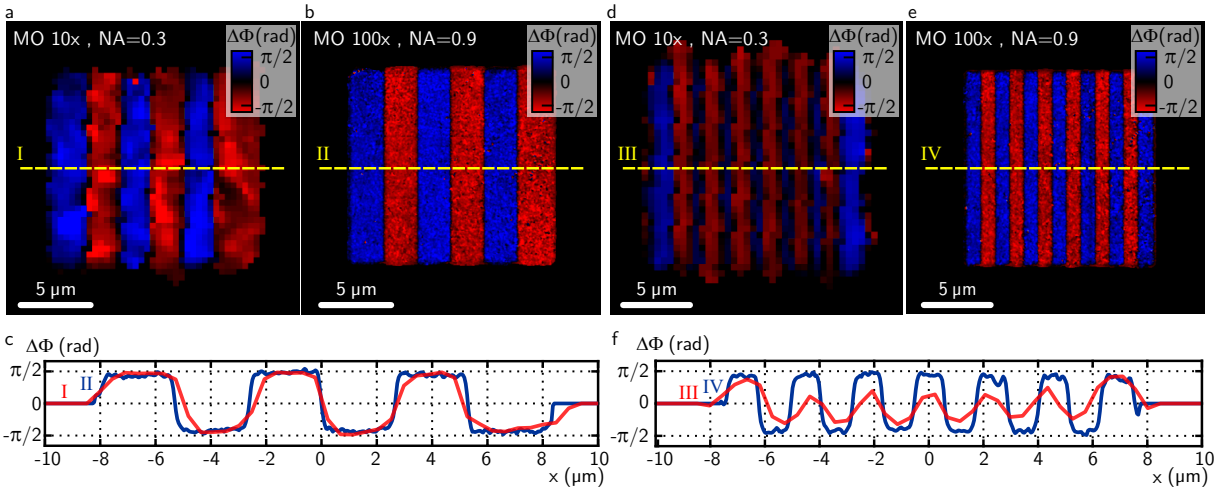

Figure 7.12 Phase imaging of metasurface gratings. (a) Color-coded phase image of low frequency grating (364 lines/mm) obtained with the MO 10×, NA = 0.3. (b) The same as in (a) but for the MO 100×, NA = 0.9. (c) Cross-section phase profiles along the dashed lines I and II. (d) Color-coded phase image of high spatial frequency grating (833 lines/mm) obtained with the MO 10×, NA = 0.3. (e) The same as in (d) but for the MO 100×, NA = 0.9. (f) Cross-section phase profiles along the dashed lines III and IV, adapted from [142].

In order to probe the technique sensitivity down to a single nanoantenna, we have fabricated another sample consisting of single nanoantenas placed in a 2.5x2.5 μm^2 grid. In such a configuration, every antenna acts itself without any influence from surrounding

antennas. Fig. 7.13a shows a SEM image of the test sample. Antennas in the grid are chosen in two orientations in order to the produce $-\pi/2$ and $\pi/2$ phase shift. Fig. 7.13b, c shows the amplitude and phase image of the sample. We can clearly observe from the amplitude image, that the sensitivity is sufficient to collect scattered light from a single nanoantenna. In the phase image, it is possible to clearly distinguish between the $-\pi/2$ and $\pi/2$ nanoantennas, even more the histogram displayed in fig. 7.13 e shows sharp peaks at $-\pi/2$ and $\pi/2$.

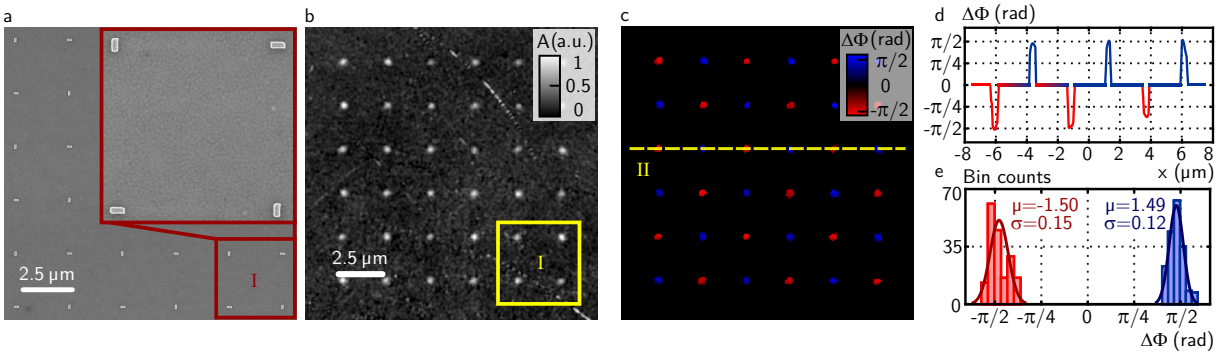

Figure 7.13 Phase imaging demonstrating the sensitivity to individual nanoantennas. (a) SEM image of an nanoantenna array used as a sample. (b) Amplitude of light scattered by individual nanoantennas reconstructed from the correlation records. (c) Color-coded phase altered by individual nanoantennas. (d) Cross-section phase profile along the dashed line in (c). (e) Histograms of the alternating phase set by the individual nanoantennas using normal distribution fitting, adapted from [142].

In the last experiments we have used the Q4GOM to image the geometrical phase metasurfaces previously studied by CCHM. Fig. 7.14 shows the reconstructed amplitude and phase images of the metasurface. We can clearly observe, that the Q4GOM together with 100× objective has resolution capable of imaging the plasmonic metasurface, where the single pixels forming the metasurface are clearly distinguishable.

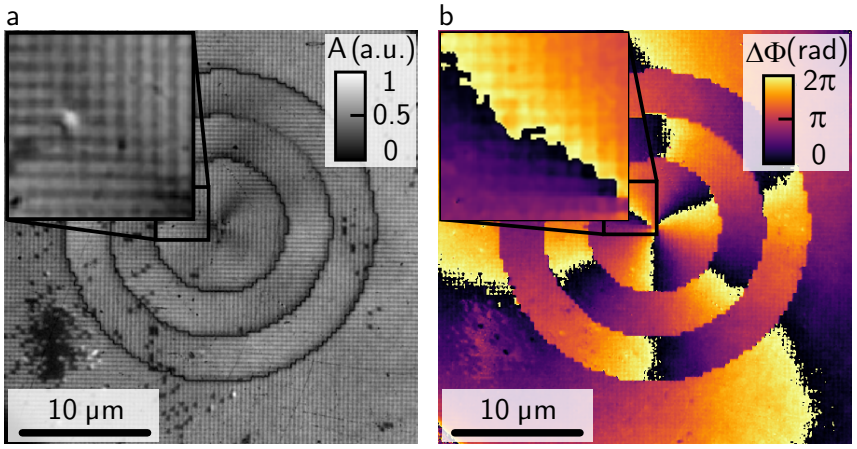

Figure 7.14 (a) Amplitude and (b) phase high-resolution images of vortex metastructures by Q4GOM, adapted from [142]

In conclusion, these experiments have proved, that even the Q4GOM has some limitations (need for polarized light), it outperforms CCHM in characterization of geometric phase metasurfaces providing unprecedented lateral resolution with perfect filtering of the driving field.

8 Conclusions

The thesis began with brief introduction into the theoretical background of plasmonics, describing some of the basic models for light-matter interaction that are used for classical materials. The introduction is followed by a section where surface plasmon-polaritons were described both as propagating waves along an infinitely long metal-dielectric interface and as eigen-modes of a metallic nanoparticle resonator. The chapter finished by overview of applications in the industry, where the plasmonic effects found their use.

The third chapter of the thesis focussed on the methods for plasmonic nanostructure fabrication, describing commonly available nanofabrication methods suitable for plasmonic nanostructure prototyping and industrial mass production. The special care was dedicated to Electron Beam Lithography as it is up to now the most widespread nanofabrication method in research and it was used in almost all experiments described in this thesis.

The fourth chapter (last chapter of the introductory part of the thesis) summarizes the techniques that can be used for plasmonic nanostructure characterization, especially for characterization of their optical properties. It shows, that plasmonic nanostructures can be characterized in many modalities, with each one revealing a part of their optical effects and that the complete characterization usually involves combination of results obtained by many techniques. The chapter especially highlights the quantitative phase imaging techniques as they are the key concept for experiments described in this thesis.

The fifth chapter focused on the development in the field of Variable-pressure Electron Beam Lithography [128]. We have shown that although this technique was previously demonstrated only for small patterns, it can be easily scaled-up to provide a robust and stable fabrication technique capable of a long-running exposures for the large-area structure fabrication. We have also demonstrated the replacement of traditionally used water vapors by nitrogen atmosphere simplifies the process allowing easier pressure control. The chapter continues with description of research in the field of structural colouring where we have demonstrated some of the basic concepts that can be used, and addressed some of the common problems that arise from fabrication of plasmonic nanostructures with resonances in the visible range [129].

The chapter dedicated to the fabrication of plasmonic nanoantennas in the THz range showed up that even when the critical dimensions of the fabricated structures are not too small, a special care and wise exposure strategy has to be taken in order to perform the patterning in a reasonable time and get expected results. In this chapter, an add-on for KLayout software allowing customized placement of individual write fields was presented together with its demonstration for periodic structures fabrication.

The last chapter focuses on the plasmonic metasurface characterisation using quantitative phase microscopy techniques. At first we have successfully demonstrated wide-field phase imaging of the plasmonic metasurfaces for the first time using Coherence-controlled Holographic Microscopy [136]. We have also presented a simple 2D flat plasmonic metasurface lens and successfully demonstrated the measurement of 3D phase distribution of the field above the lens surface. Our experiments continued with modification of

the Coherene-controlled Holographic Microscopy setup which allowed characterization of state-of-the-art plasmonic metamaterials based on the geometrical phase concept [138]. In the last experiments, we have demonstrated applications of brand-new Quantitative 4G Optical Microscopy for the geometrical phase metasurface characterization that outperforms all currently known techniques of plasmonic metasurface characterization by its unprecedented lateral resolution allowing imaging of the individual metasurface building blocks [141].

In conclusion, we have demonstrated that far-field Quantitative phase imaging techniques are one of the most promising techniques for plasmonic metasurface characterization, that open new possibilities for an easy check-up of fabricated structures, although there is still a lot of space for further development and integration of these techniques to standard metasurface nanofabrication workflow.

A Custom parametric cell design in KLayout software

The parametric cells (PCell) is a system in the KLayout editor which allows the user to design own special shapes defined by a set of parameters. The KLayout then runs an user script which generates the required geometry from these parameters. This chapter briefly comments on how such parametric cells can be created and used.

The geometry of each parametric cell can be defined in two ways: graphically using some guiding shapes (points, polygons, paths) that can be visually edited in the editor workspace or by numeric parameters. In the following example, we will describe the definition of a diabolo (see fig. A.1) cell used in chapter 6. When we look at the diabolo cell, its graphical definition is done by two points: the bridge handle, which controls the length and width of the bridge, and wing handle, controlling the wing length and angle. The diabolo can also be defined numerically by specifying the following parameters:

- b_l – bridge length
- b_w – bridge width
- w_l – wing length
- α – wing angle.

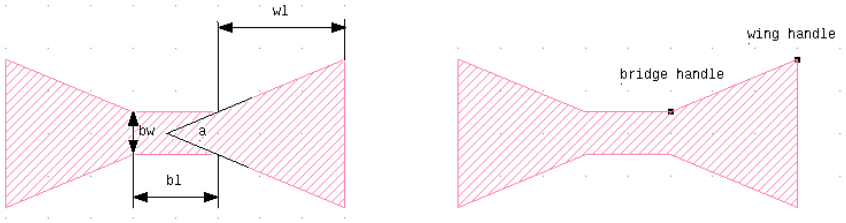

Figure A.1 Definition of diabolo PCell by numerical parameters (left), guiding shapes (right)

In order to make the calculations easier, we suppose the diabolo to be placed in the center of the cell's coordinate system meaning the $[0, 0]$ point being in the bridge center.

At the beginning we import the `pya` module containing the basic KLayout API together with a standard `math` module

```
import math
import pya
```

Each PCell in the KLayout is defined as a subclass of `PCellDeclarationHelper` class

```
class Diabolo(pya.PCellDeclarationHelper):
```

The main task in the class constructor is definition of the PCell parameters and their default values, we start with the numeric ones (b_l, b_w, w_l and α)

```
  def __init__(self):
    super(Diabolo, self).__init__()
    self.param("bl", self.TypeDouble, "Bridge length", default = 0.1)
    self.param("bw", self.TypeDouble, "Bridge width", default = 0.1)
    self.param("wl", self.TypeDouble, "Wing length", default = 0.1)
    self.param("a", self.TypeDouble, "Wing angle", default = 45)
```

Following with the parameter 'Layer' defining the layer, where the geometry should be generated, we have chosen LAYER 1 DATATYPE 0 as a default value

```
    self.param("l", self.TypeLayer, "Layer", default = pya.LayerInfo(1,
0))
```

Next parameters are the graphic handles, that are used for graphical editing (bridge handle and wing handle – see fig. A.1)

```
    self.param("hb", self.TypeShape, "", default = pya.DPoint(0.05,
0.05))
    self.param("hw", self.TypeShape, "", default = pya.DPoint(0.15,
0.09142135623730951))
```

For every numeric parameter we define one hidden parameter, which will be used in the `coerce_parameters_impl` method

```
    self.param("bl_", self.TypeDouble, "Bridge length", default = 0.1,
hidden = True)
    self.param("bw_", self.TypeDouble, "Bridge width", default = 0.1,
hidden = True)
    self.param("wl_", self.TypeDouble, "Wing length", default = 0.1,
hidden = True)
    self.param("a_", self.TypeDouble, "Wing angle", default = 45, hidden
= True)
```

The next method `display_text_impl` should provide text description that is shown when the cell contents are not drawn. We will assemble simple description from parameters

```
  def display_text_impl(self):
    return "Diabolo(bl=" + str('%.3f' % self.bl) + ",bw=" + ('%.3f' %
self.bw) +  ",wl=" + ('%.3f' % self.wl) + ",angle=" + ('%.3f' % self.a)
+")"
```

The method `coerce_parameters_impl` is called by the KLayout editor anytime the PCell parameters are changed expecting to make them consistent. At the beginning, we make sure dimensions are not negative

```
  def coerce_parameters_impl(self):
    if self.bl < 0:
      self.bl *= -1
```

```
    if self.bw < 0:
      self.bw *= -1
    if self.wl < 0:
      self.wl *= -1
```

In the next step we have to determine, if the PCell was modified by a numeric input or by handle movement. In order to achieve this, we check if numeric parameters are equal hidden ones. When the user changes numeric parameters, they will be different, but when he changes the handle, they will be the same

```
    if self.bl != self.bl_ or self.bw != self.bw_ or self.wl != self.wl_
or self.a != self.a_:
```

In the case numeric parameters were changed, we have to calculate a new position of the handle and copy new numeric values to hidden parameters

```
      # bridge handle
      hbx = self.bl/2
      hby = self.bw/2
      # wing handle
      hwx = hbx + self.wl
      hwy = hby + self.wl * math.tan(math.radians(self.a/2))
      # assemble handle objects
      self.hb = pya.DPoint(hbx, hby)
      self.hw = pya.DPoint(hwx, hwy)
      # copy values to hidden params
      self.bl_ = self.bl
      self.bw_ = self.bw
      self.wl_ = self.wl
      self.a_ = self.a
```

In case the handle was moved, we have to calculate new numeric parameters from the handle position

```
    else:
      hbx = abs(self.hb.x)
      hby = abs(self.hb.y)
      hwx = abs(self.hw.x)
      hwy = abs(self.hw.y)
      self.bl = self.bl_ = hbx * 2
      self.bw = self.bw_ = hby * 2
      self.wl = self.wl_ = hwx - hbx
      self.a = self.a_ = 2 * math.degrees(math.atan((hwy - hby)/self.wl))
```

The `can_create_from_shape_impl` is used by the KLayout when the user wants to convert some standard object to PCell to determine if the object can be converted, for the simplicity we assume, that no object can be converted to diabolo

```
  def can_create_from_shape_impl(self):
    return False
```

Methods `parameters_from_shape_impl` and `transformation_from_shape_impl` are used for the conversion, in our case, we leave them empty

```
  def parameters_from_shape_impl(self):
    return None

  def transformation_from_shape_impl(self):
    return None
```

The `produce_impl` method is the core method of our PCell, which is called by the KLayout to generate the geometry of the PCell. At the beginning, we get the value of the database unit stored by UNITS record as the dimensions of constructed objects are in database units, while our input is in µm, we also calculate $\tan\frac{\alpha}{2}$ as it will be needed later

```
  def produce_impl(self):
    dbu = self.layout.dbu
    tg = math.tan(math.radians(self.a/2))
```

In the next step we calculate a list of points, that represents our diabolo

```
    pts = []
    pts.append(pya.Point(pya.DPoint((-self.bl/2)/dbu, (self.bw/2)/dbu)))
    pts.append(pya.Point(pya.DPoint((-self.bl/2-self.wl)/dbu,
(self.bw/2+self.wl*tg)/dbu)))
    pts.append(pya.Point(pya.DPoint((-self.bl/2-self.wl)/dbu,
(-self.bw/2-self.wl*tg)/dbu)))
    pts.append(pya.Point(pya.DPoint((-self.bl/2)/dbu, -(self.bw/2)/dbu)))
    pts.append(pya.Point(pya.DPoint((self.bl/2)/dbu, -(self.bw/2)/dbu)))
    pts.append(pya.Point(pya.DPoint((self.bl/2+self.wl)/dbu,
(-self.bw/2-self.wl*tg)/dbu)))
    pts.append(pya.Point(pya.DPoint((self.bl/2+self.wl)/dbu,
(self.bw/2+self.wl*tg)/dbu)))
    pts.append(pya.Point(pya.DPoint((self.bl/2)/dbu, (self.bw/2)/dbu)))
```

In the last step, we create a new polygon representing the diabolo, and we insert it into the PCell shape list

```
    self.cell.shapes(self.l_layer).insert(pya.Polygon(pts))
```

In order to access the PCell in the KLayout, we have to create a PCell library, insert the PCell into the library, and register the library in the KLayout. This library script should be then marked as run at startup to have the library available

```
class Plasmonics(pya.Library):
```

```
  def __init__(self):
    self.description = "Plasmonic structures"
    self.layout().register_pcell("Diabolo", Diabolo())
    self.register("Plasmonics")

Plasmonics()
```

References

[1] S.A. Maier, *Plasmonics: Fundamentals and Applications* (Springer Science & Business Media, 2007).

[2] M. Fox, *Optical Properties of Solids*, no. v. 3, 2nd ed ed. (Oxford University Press, Oxford; New York, 2010).

[3] P. Drude, Zur Elektronentheorie Der Metalle, *Annalen der Physik* **306**(3), 566-613 (1900).

[4] Sellmeier, Zur Erklärung der abnormen Farbenfolge im Spectrum einiger Substanzen, *Annalen der Physik und Chemie* **219**(6), 272-282 (1871).

[5] H.A. Lorentz, *Versuch Einer Theorie Der Electrischen Und Optischen Erscheinungen in Bewegten Körpern* (Cambridge University Press, Cambridge, 2013).

[6] W.L. Barnes, Surface Plasmon–Polariton Length Scales: A Route to Sub-Wavelength Optics, *Journal of Optics A: Pure and Applied Optics* **8**(4), S87-S93 (2006).

[7] A. Otto, Excitation of Nonradiative Surface Plasma Waves in Silver by the Method of Frustrated Total Reflection, *Zeitschrift für Physik A Hadrons and nuclei* **216**(4), 398-410 (1968).

[8] E. Kretschmann and H. Raether, Notizen: Radiative Decay of Non Radiative Surface Plasmons Excited by Light, *Zeitschrift für Naturforschung A* **23**(12), (1968).

[9] M. Pelton and G.W. Bryant, *Introduction to Metal-Nanoparticle Plasmonics* (Wiley: Science Wise Publishing, Hoboken, New Jersey, 2013).

[10] H. Fröhlich, *Theory of Dielectrics: Dielectrics Constant and Dielectric Loss*, 2nd ed ed. (Clarendon Press, Oxford, 1986).

[11] G. Mie, Beiträge Zur Optik Trüber Medien, Speziell Kolloidaler Metallösungen, *Annalen der Physik* **330**(3), 377-445 (1908).

[12] P. Biagioni, J.S. Huang, and B. Hecht, Nanoantennas for Visible and Infrared Radiation, *Reports on Progress in Physics* **75**(2), 024402 (2012).

[13] C.F. Bohren and D.R. Huffman, *Absorption and Scattering of Light by Small Particles* (Wiley-VCH Verlag GmbH, Weinheim, Germany, 1998).

[14] M. Agio and A. Alù, *Optical Antennas* (Cambridge University Press, 2013).

[15] A. Kristensen, J.K.W. Yang, S.I. Bozhevolnyi, S. Link, P. Nordlander, N.J. Halas, and N.A. Mortensen, Plasmonic Colour Generation, *Nature Reviews Materials* **2**(1), 16088 (2017).

[16] K. Kumar, H. Duan, R.S. Hegde, S.C.W. Koh, J.N. Wei, and J.K.W. Yang, Printing Colour at the Optical Diffraction Limit, *Nature Nanotechnology* **7**(9), 557-561 (2012).

[17] S.J. Tan, L. Zhang, D. Zhu, X.M. Goh, Y.M. Wang, K. Kumar, C.W. Qiu, and J.K.W. Yang, Plasmonic Color Palettes for Photorealistic Printing with Aluminum Nanostructures, *Nano Letters* **14**(7), 4023-4029 (2014).

[18] M. Miyata, H. Hatada, and J. Takahara, Full-Color Subwavelength Printing with Gap-Plasmonic Optical Antennas, *Nano Letters* **16**(5), 3166-3172 (2016).

[19] H. Jiang and B. Kaminska, Scalable Inkjet-Based Structural Color Printing by Molding Transparent Gratings on Multilayer Nanostructured Surfaces, *ACS Nano* **12**(4), 3112-3125 (2018).

[20] X. Duan, S. Kamin, and N. Liu, Dynamic Plasmonic Colour Display, *Nature Communications* **8** 14606 (2017).

[21] P. Genevet, F. Capasso, F. Aieta, M. Khorasaninejad, and R. Devlin, Recent Advances in Planar Optics: From Plasmonic to Dielectric Metasurfaces, *Optica* **4**(1), 139 (2017).

[22] H.H. Hsiao, C.H. Chu, and D.P. Tsai, Fundamentals and Applications of Metasurfaces, *Small Methods* **1**(4), 1600064 (2017).

[23] F. Aieta, P. Genevet, M.A. Kats, N. Yu, R. Blanchard, Z. Gaburro, and F. Capasso, Aberration-Free Ultrathin Flat Lenses and Axicons at Telecom Wavelengths Based on Plasmonic Metasurfaces, *Nano Letters* **12**(9), 4932-4936 (2012).

[24] N. Yu, F. Aieta, P. Genevet, M.A. Kats, Z. Gaburro, and F. Capasso, A Broadband, Background-Free Quarter-Wave Plate Based on Plasmonic Metasurfaces, *Nano Letters* **12**(12), 6328-6333 (2012).

[25] C.M. Soukoulis, S. Linden, and M. Wegener, Negative Refractive Index at Optical Wavelengths, *Science* **315**(5808), 47-49 (2007).

[26] V.M. Shalaev, W. Cai, U.K. Chettiar, H.K. Yuan, A.K. Sarychev, V.P. Drachev, and A.V. Kildishev, Negative Index of Refraction in Optical Metamaterials, *Optics Letters* **30**(24), 3356 (2005).

[27] Y. Zhang, X. Yang, and J. Gao, Twisting Phase and Intensity of Light with Plasmonic Metasurfaces, *Scientific Reports* **8**(1), 4884 (2018).

[28] J.N. Anker, W.P. Hall, O. Lyandres, N.C. Shah, J. Zhao, and R.P. Van Duyne, Biosensing with Plasmonic Nanosensors, In Nanoscience and Technology, pp.. 308-319 (Co-Published with Macmillan Publishers Ltd, UK, 2009).

[29] J. Homola, S.S. Yee, and G. Gauglitz, Surface Plasmon Resonance Sensors: Review, *Sensors and Actuators B: Chemical* **54**(1-2), 3-15 (1999).

[30] S. Schultz, D.R. Smith, J.J. Mock, and D.A. Schultz, Single-Target Molecule Detection with Nonbleaching Multicolor Optical Immunolabels, *Proceedings of the National Academy of Sciences* **97**(3), 996-1001 (2000).

[31] J. Yguerabide and E.E. Yguerabide, Light-Scattering Submicroscopic Particles as Highly Fluorescent Analogs and Their Use as Tracer Labels in Clinical and Biological Applications, *Analytical Biochemistry* **262**(2), 137-156 (1998).

[32] E.J. Blackie, E.C.L. Ru, and P.G. Etchegoin, Single-Molecule Surface-Enhanced Raman Spectroscopy of Nonresonant Molecules, (2009).

[33] A. Kinkhabwala, Z. Yu, S. Fan, Y. Avlasevich, K. Müllen, and W.E. Moerner, Large Single-Molecule Fluorescence Enhancements Produced by a Bowtie Nanoantenna, *Nature Photonics* **3**(11), 654-657 (2009).

[34] B. Sepúlveda, P.C. Angelomé, L.M. Lechuga, and L.M. Liz-Marzán, LSPR-Based Nanobiosensors, *Nano Today* **4**(3), 244-251 (2009).

[35] S.S. Aćimović, M.A. Ortega, V. Sanz, J. Berthelot, J.L. Garcia-Cordero, J. Renger, S.J. Maerkl, M.P. Kreuzer, and R. Quidant, LSPR Chip for Parallel, Rapid, and Sensitive Detection of Cancer Markers in Serum, *Nano Letters* **14**(5), 2636-2641 (2014).

[36] K. Lodewijks, W. Van Roy, G. Borghs, L. Lagae, and P. Van Dorpe, Boosting the Figure-Of-Merit of LSPR-Based Refractive Index Sensing by Phase-Sensitive Measurements, *Nano Letters* **12**(3), 1655-1659 (2012).

[37] J.W. Stewart, G.M. Akselrod, D.R. Smith, and M.H. Mikkelsen, Toward Multispectral Imaging with Colloidal Metasurface Pixels, *Advanced Materials* **29**(6), 1602971 (2017).

[38] Calma company, *GDSII Stream Format Manual* (Calma company, 1987).

[39] R. Sproull and R. Lyon, *The Caltech Intermediate Form for LSI Layout Description*, (1980).

[40] SEMI International Standards, *SEMI P39-0416 - Specification for OASIS - Open Artwork System Interchange Standard* (SEMI International Standards, 2016).

[41] A.J. Reich, K.H. Nakagawa, and R.E. Boone, OASIS vs. GDSII Stream Format Efficiency, In 23rd Annual BACUS Symposium on Photomask Technology (International Society for Optics and Photonics, 2003).

[42] M. Köfferlein, *KLayout*, (2018).

[43] P. Rai-Choudhury, *Handbook of Microlithography, Micromachining, and Microfabrication. Volume 1: Microlithography* (SPIE PRESS, 1997).

[44] M.A. Mohammad, T. Fito, J. Chen, S. Buswell, M. Aktary, M. Stepanova, and S.K. Dew, Systematic Study of the Interdependence of Exposure and Development Conditions and Kinetic Modelling for Optimizing Low-Energy Electron Beam Nanolithography, *Microelectronic Engineering* **87**(5), 1104-1107 (2010).

[45] W. (Walter) Hu, K. Sarveswaran, M. Lieberman, and G.H. Bernstein, Sub-10 Nm Electron Beam Lithography Using Cold Development of Poly(Methylmethacrylate), *Journal of Vacuum Science & Technology B: Microelectronics and Nanometer Structures Processing, Measurement, and Phenomena* **22**(4), 1711-1716 (2004).

[46] L.Y.M. Tobing, L. Tjahjana, and D.H. Zhang, Large Contrast Enhancement by Sonication Assisted Cold Development Process for Low Dose and Ultrahigh Resolution Patterning on ZEP520A Positive Tone Resist, *Journal of Vacuum Science & Technology B* **30**(5), 051601 (2012).

[47] I. Zailer, J.E.F. Frost, V. Chabasseur-Molyneux, C.J.B. Ford, and M. Pepper, Crosslinked PMMA as a High-Resolution Negative Resist for Electron Beam Lithography and Applications for Physics of Low-Dimensional Structures, *Semiconductor Science and Technology* **11**(8), 1235 (1996).

[48] S. Yasin, D.G. Hasko, and H. Ahmed, Comparison of MIBK/IPA and Water/IPA as PMMA Developers for Electron Beam Nanolithography, *Microelectronic Engineering* **61-62** 745-753 (2002).

[49] M. Schirmer, B. Büttner, F. Syrowatka, G. Schmidt, T. Köpnick, and C. Kaiser, Chemical Semi-Amplified Positive E-Beam Resist (CSAR 62) for Highest Resolution, In 29th European Mask and Lithography Conference (International Society for Optics and Photonics, 2013).

[50] S. Thoms and D.S. Macintyre, Investigation of CSAR 62, a New Resist for Electron Beam Lithography, *Journal of Vacuum Science & Technology B* **32**(6), 06FJ01 (2014).

[51] Allresist GmbH, *Negative E-Beam Resists AR-N 7520*, (2017).

[52] A.E. Grigorescu and C.W. Hagen, Resists for Sub-20-Nm Electron Beam Lithography with a Focus on HSQ: State of the Art, *Nanotechnology* **20**(29), 292001 (2009).

[53] D. Meyerhofer, Characteristics of Resist Films Produced by Spinning, *Journal of Applied Physics* **49**(7), 3993-3997 (1978).

[54] M. Corp., *PMMA Data Sheet*, (2001).

[55] A.P. Blanchard-Dionne and M. Meunier, Electron Beam Lithography Using a PMMA/P(MMA 8.5 MAA) Bilayer for Negative Tone Lift-off Process, *Journal of Vacuum Science & Technology B* **33**(6), 061602 (2015).

[56] M. Rooks, *EBPG Hardware Tour*, https://nano.yale.edu/ebpg-hardware-tour (2017).

[57] MAPPER Lithography B.V., *Mapper Technology*, https://mapper.nl/technology/ (2017).

[58] V. Kolařík, F. Matějka, B. Lencová, S. Kokrhel, M. Horáček, T. Radlička, M. Urbánek, and L. Daněk, Writing System with Shaped Electron Beam, *Fine Mechanics and Optics* **53**(1), 11-16 (2008).

[59] A.A. Tseng, K. Chen, C.D. Chen, and K.J. Ma, Electron Beam Lithography in Nanoscale Fabrication: Recent Development, *IEEE Transactions on Electronics Packaging Manufacturing* **26**(2), 141-149 (2003).

[60] T.H.P. Chang, Proximity Effect in Electron-beam Lithography, *Journal of Vacuum Science and Technology* **12**(6), 1271-1275 (1975).

[61] S.J. Wind, Proximity Correction for Electron Beam Lithography Using a Three-Gaussian Model of the Electron Energy Distribution, *Journal of Vacuum Science & Technology B: Microelectronics and Nanometer Structures* **7**(6), 1507 (1989).

[62] C.H. Liu, New Parametric Point Spread Function Calibration Methodology for Improving the Accuracy of Patterning Prediction in Electron-Beam Lithography, *Journal of Micro/Nanolithography, MEMS, and MOEMS* **11**(1), 013009 (2012).

[63] Raith GmbH., *NanoSuite Software Reference Manual*, (2011).

[64] L. Stevens, R. Jonckheere, E. Froyen, S. Decoutere, and D. Lanneer, Determination of the Proximity Parameters in Electron Beam Lithography Using Doughnut-Structures, *Microelectronic Engineering* **5**(1), 141-150 (1986).

[65] S.V. Dubonos, B.N. Gaifullin, H.F. Raith, A.A. Svintsov, and S.I. Zaitsev, Evaluation, Verification and Error Determination of Proximity Parameters α, β and ν in Electron Beam Lithography, *Microelectronic Engineering* **21**(1), 293-296 (1993).

[66] M. Parikh, Self-consistent Proximity Effect Correction Technique for Resist Exposure (SPECTRE), *Journal of Vacuum Science and Technology* **15**(3), 931-933 (1978).

[67] H. Eisenmann, T. Waas, and H. Hartmann, PROXECCO–Proximity Effect Correction by Convolution, *Journal of Vacuum Science & Technology B: Microelectronics and Nanometer Structures Processing, Measurement, and Phenomena* **11**(6), 2741-2745 (1993).

[68] M. Parikh, Calculation of Changes in Pattern Dimensions to Compensate for Proximity Effects in Electron Lithography, *Journal of Applied Physics* **51**(1), 705-709 (1980).

[69] L.E. Ocola, D.J. Gosztola, D. Rosenmann, and G. Lopez, Automated Geometry Assisted Proximity Effect Correction for Electron Beam Direct Write Nanolithography, *Journal of Vacuum Science & Technology B* **33**(6), 06FD02 (2015).

[70] C. Nien, L.C. Chang, J.H. Ye, V.C. Su, C.H. Wu, and C.H. Kuan, Proximity Effect Correction in Electron-Beam Lithography Based on Computation of Critical-Development Time with Swarm Intelligence, *Journal of Vacuum Science & Technology B* **35**(5), 051603 (2017).

[71] G.G. Lopez, M. Azadi, M.G. Metzler, N. Belic, and U. Hofmann, Isofocal Dose Based Proximity Effect Correction Tolerance to the Effective Process Blur, *Journal of Vacuum Science & Technology B* **35**(6), 06G505 (2017).

[72] S. Babin, S. Borisov, and E. Patyukova, Simulation of Dose Variation and Charging Due to Fogging in Electron Beam Lithography, *Journal of Vacuum Science & Technology B* **31**(6), 06F411 (2013).

[73] J. Joo, B.Y. Chow,, and J.M. and Jacobson*, Nanoscale Patterning on Insulating Substrates by Critical Energy Electron Beam Lithography, (2006).

[74] B.D. and Myers and V.P. Dravid, Variable Pressure Electron Beam Lithography (VP-eBL): A New Tool for Direct Patterning of Nanometer-Scale Features on Substrates with Low Electrical Conductivity, (2006).

[75] N. Yao, *Focused Ion Beam Systems: Basics and Applications*, 1 edition ed. (Cambridge University Press, 2007).

[76] G. Hlawacek, V. Veligura, van Gastel Raoul, and B. Poelsema, Helium Ion Microscopy, *Journal of Vacuum Science & Technology B* **32**(2), 020801 (2014).

[77] S. Bauerdick, L. Bruchhaus, P. Mazarov, A. Nadzeyka, R. Jede, J. Fridmann, J.E. Sanabia, B. Gila, and B.R. Appleton, Multispecies Focused Ion Beam Lithography System and Its Applications, *Journal of Vacuum Science & Technology B* **31**(6), 06F404 (2013).

[78] J.S. Huang, V. Callegari, P. Geisler, C. Brüning, J. Kern, J.C. Prangsma, X. Wu, T. Feichtner, J. Ziegler, P. Weinmann *et al.*, Atomically Flat Single-Crystalline Gold Nanostructures for Plasmonic Nanocircuitry, *Nature Communications* **1** 150 (2010).

[79] O. Scholder, K. Jefimovs, I. Shorubalko, C. Hafner, U. Sennhauser, and G.L. Bona, Helium Focused Ion Beam Fabricated Plasmonic Antennas with Sub-5 Nm Gaps, *Nanotechnology* **24**(39), 395301 (2013).

[80] L. Pastewka, R. Salzer, A. Graff, F. Altmann, and M. Moseler, Surface Amorphization, Sputter Rate, and Intrinsic Stresses of Silicon during Low Energy Ga+ Focused-Ion Beam Milling, *Nuclear Instruments and Methods in Physics Research Section B: Beam Interactions with Materials and Atoms* **267**(18), 3072-3075 (2009).

[81] C. Haverkamp, K. Höflich, S. Jäckle, A. Manzoni, and S. Christiansen, Plasmonic Gold Helices for the Visible Range Fabricated by Oxygen Plasma Purification of Electron Beam Induced Deposits, *Nanotechnology* **28**(5), 055303 (2017).

[82] Orsay Physics, *What Is FIB?*, (2019).

[83] R. Garcia, A.W. Knoll, and E. Riedo, Advanced Scanning Probe Lithography, *Nature Nanotechnology* **9**(8), 577-587 (2014).

[84] Y.R. Ma, C. Yu, Y.D. Yao, Y. Liou, and S.F. Lee, Tip-Induced Local Anodic Oxidation on the Native SiO_2 Layer of Si(111) Using an Atomic Force Microscope, *Physical Review B* **64**(19), 195324 (2001).

[85] R.D. Piner, J. Zhu, F. Xu, S. Hong, and C.A. Mirkin, "Dip-Pen" Nanolithography, *Science* **283**(5402), 661-663 (1999).

[86] SwissLitho AG, *SwissLitho AG*, https://swisslitho.com/ (2018).

[87] P. Paul, A.W. Knoll, F. Holzner, and U. Duerig, Field Stitching in Thermal Probe Lithography by Means of Surface Roughness Correlation, *Nanotechnology* **23**(38), 385307 (2012).

[88] C. Neuber, H.W. Schmidt, P. Strohriegl, A. Ringk, T. Kolb, A. Schedl, V. Fokkema, M.G.A. van Veghel, M. Cooke, C. Rawlings *et al.*, Tailored Molecular Glass Resists for Scanning Probe Lithography, In Advances in Patterning Materials and Processes XXXII (International Society for Optics and Photonics, 2015).

[89] J.F. de Marneffe, B.T. Chan, M. Spieser, G. Vereecke, S. Naumov, D. Vanhaeren, H. Wolf, and A.W. Knoll, Conversion of a Patterned Organic Resist into a High Performance Inorganic Hard Mask for High Resolution Pattern Transfer, *ACS Nano* **12**(11), 11152-11160 (2018).

[90] F. Holzner, C. Kuemin, P. Paul, J.L. Hedrick, H. Wolf, N.D. Spencer, U. Duerig, and A.W. Knoll, Directed Placement of Gold Nanorods Using a Removable Template for Guided Assembly, *Nano Letters* **11**(9), 3957-3962 (2011).

[91] H. Wolf, C. Rawlings, P. Mensch, J.L. Hedrick, D.J. Coady, U. Duerig, and A.W. Knoll, Sub-20 Nm Silicon Patterning and Metal Lift-off Using Thermal Scanning Probe Lithography, *Journal of Vacuum Science & Technology B* **33**(2), 02B102 (2014).

[92] R. Garcia, A.W. Knoll, and E. Riedo, Advanced Scanning Probe Lithography, *Nature Nanotechnology* **9**(8), 577-587 (2014).

[93] A. Pirati, R. Peeters, D. Smith, S. Lok, A. Minnaert, van Noordenburg Martijn, J. Mallmann, N. Harned, J. Stoeldraijer, C. Wagner *et al.*, Performance Overview and Outlook of EUV Lithography Systems, In O.R. Wood and E.M. Panning (Eds.) SPIE Advanced Lithography (San Jose, California, United States, 2015).

[94] A. Pirati, R. Peeters, D. Smith, S. Lok, van Noordenburg Martijn, van Es Roderik, E. Verhoeven, H. Meijer, A. Minnaert, van der Horst Jan-Willem *et al.*, EUV Lithography Performance for Manufacturing: Status and Outlook, In E.M. Panning and K.A. Goldberg (Eds.) SPIE Advanced Lithography (San Jose, California, United States, 2016).

[95] I. Fomenkov, D. Brandt, A. Ershov, A. Schafgans, Y. Tao, G. Vaschenko, S. Rokitski, M. Kats, M. Vargas, M. Purvis *et al.*, Light Sources for High-Volume Manufacturing EUV Lithography: Technology, Performance, and Power Scaling, *Advanced Optical Technologies* **6**(3-4), (2017).

[96] L. Li, X. Liu, S. Pal, S. Wang, C.K. Ober, and E.P. Giannelis, Extreme Ultraviolet Resist Materials for Sub-7 Nm Patterning, *Chemical Society Reviews* **46**(16), 4855-4866 (2017).

[97] H. Degans, *Press Release - Imec and ASML Enter Next Stage of EUV Lithography Collaboration*, (2018).

[98] H. Schift, Nanoimprint Lithography: An Old Story in Modern Times? A Review, *Journal of Vacuum Science & Technology B: Microelectronics and Nanometer Structures Processing, Measurement, and Phenomena* **26**(2), 458-480 (2008).

[99] L.J. Guo, Nanoimprint Lithography: Methods and Material Requirements, *Advanced Materials* **19**(4), 495-513 (2007).

[100] X. Cheng and L. Jay Guo, One-Step Lithography for Various Size Patterns with a Hybrid Mask-Mold, *Microelectronic Engineering* **71**(3-4), 288-293 (2004).

[101] I. Brodie and J.J. Muray, *The Physics of Micro/Nano-Fabrication* (Springer US, Boston, MA, 1992). (OCLC: 864076570)

[102] Dr. Eberl MBE-Komponenten GmbH, *Electron Beam Evaporator EBV*, (2018).

[103] T. Šikola, *Modification of Surfaces and Deposition of Thin Films by Ion Beams; In situ Analysis of Surfaces and Thin Films*, (Habilitation Thesis). Technical University of Brno, Brno (1998).

[104] H.R. Kaufman, J.J. Cuomo, and J.M.E. Harper, Technology and Applications of Broad-beam Ion Sources Used in Sputtering. Part I. Ion Source Technology, *Journal of Vacuum Science and Technology* **21**(3), 725-736 (1982).

[105] H. Jansen, H. Gardeniers, M. de Boer, M. Elwenspoek, and J. Fluitman, A Survey on the Reactive Ion Etching of Silicon in Microtechnology, *Journal of Micromechanics and Microengineering* **6**(1), 14-28 (1996).

[106] L. Reimer, *Scanning Electron Microscopy: Physics of Image Formation and Microanalysis* (2010).

[107] B.L. Thiel and M. Toth, Secondary Electron Contrast in Low-Vacuum/environmental Scanning Electron Microscopy of Dielectrics, *Journal of Applied Physics* **97**(5), 051101 (2005).

[108] D.C. Joy and C.S. Joy, Low Voltage Scanning Electron Microscopy, *Micron* **27**(3-4), 247-263 (1996).

[109] Springer Berlin Heidelberg, *Scanning Probe Microscopy* (Springer Berlin Heidelberg, New York, NY, 2015).

[110] J.F. Watts and J. Wolstenholme, *An Introduction to Surface Analysis by XPS and AES* (J. Wiley, Chichester, West Sussex, England ; New York, 2003).

[111] D. Shindō and T. Oikawa, *Analytical Electron Microscopy for Materials Science* (Springer, Tokyo ; Berlin, 2002). (OCLC: ocm50738825)

[112] J.C. Russ, *Fundamentals of Energy Dispersive X-Ray Analysis: Butterworths Monographs in Materials* (Butterworth-Heinemann, 2013).

[113] Petr Dvořák, Filip Ligmajer, Tomáš Šamořil, Martin Hrtoň, Robert Klement, Marek Tuček, Jiří Spousta, and Tomáš Šikola, Application of Reflective Optical Spectroscopy for Experimental Studies of Plasmonic Nanostructures, *Fine Mechanics and Optics* **59**(6-7), 162-164 (2014).

[114] B.C. Smith, *Fundamentals of Fourier Transform Infrared Spectroscopy*, 2nd ed ed. (CRC Press, Boca Raton, FL, 2011).

[115] J. Kauppinen and J. Partanen, *Fourier Transforms in Spectroscopy*, 1st ed ed. (Wiley-VCH, Berlin ; New York, 2001). (OCLC: ocm45541959)

[116] T.W.H. Oates, H. Wormeester, and H. Arwin, Characterization of Plasmonic Effects in Thin Films and Metamaterials Using Spectroscopic Ellipsometry, *Progress in Surface Science* **86**(11-12), 328-376 (2011).

[117] I. Sersic, C. Tuambilangana, and A. Femius Koenderink, Fourier Microscopy of Single Plasmonic Scatterers, *New Journal of Physics* **13**(8), 083019 (2011).

[118] M.K. Kim, Principles and Techniques of Digital Holographic Microscopy, *Journal of Photonics for Energy* 018005 (2010).

[119] P. Marquet, B. Rappaz, P.J. Magistretti, E. Cuche, Y. Emery, T. Colomb, and C. Depeursinge, Digital Holographic Microscopy: A Noninvasive Contrast Imaging Technique Allowing Quantitative Visualization of Living Cells with Subwavelength Axial Accuracy, *Optics Letters* **30**(5), 468 (2005).

[120] J. Balvan, A. Krizova, J. Gumulec, M. Raudenska, Z. Sladek, M. Sedlackova, P. Babula, M. Sztalmachova, R. Kizek, R. Chmelik *et al.*, Multimodal Holographic Microscopy: Distinction between Apoptosis and Oncosis, *PLOS ONE* **10**(3), e0121674 (2015).

[121] T. Zikmund, L. Kvasnica, M. Týč, A. Křížová, J. Čolláková, and R. Chmelík, Sequential Processing of Quantitative Phase Images for the Study of Cell Behaviour in Real-Time Digital Holographic Microscopy: SEQUENTIAL PROCESSING OF QUANTITATIVE PHASE IMAGES, *Journal of Microscopy* **256**(2), 117-125 (2014).

[122] T. Xi, J. Di, X. Guan, Y. Li, C. Ma, J. Zhang, and J. Zhao, Phase-Shifting Infrared Digital Holographic Microscopy Based on an All-Fiber Variable Phase Shifter, *Applied Optics* **56**(10), 2686 (2017).

[123] P. Kolman and R. Chmelík, Coherence-Controlled Holographic Microscope, *Optics Express* **18**(21), 21990-22004 (2010).

[124] T. Slabý, P. Kolman, Z. Dostál, M. Antoš, M. Lošťák, and R. Chmelík, Off-Axis Setup Taking Full Advantage of Incoherent Illumination in Coherence-Controlled Holographic Microscope, *Optics Express* **21**(12), 14747-14762 (2013).

[125] T. Kreis, Digital Holographic Interference-Phase Measurement Using the Fourier-Transform Method, *JOSA A* **3**(6), 847-855 (1986).

[126] Gatan, Inc., *Eels.Info*, (2019).

[127] T. Coenen, E.J.R. Vesseur, A. Polman, and A.F. Koenderink, Directional Emission from Plasmonic Yagi–Uda Antennas Probed by Angle-Resolved Cathodoluminescence Spectroscopy, *Nano Letters* **11**(9), 3779-3784 (2011).

[128] J. Babocký, P. Dvořák, F. Ligmajer, M. Hrtoň, T. Šikola, J. Bok, and J. Fiala, Patterning Large Area Plasmonic Nanostructures on Nonconductive Substrates Using Variable Pressure Electron Beam Lithography, *Journal of Vacuum Science & Technology B* **34**(6), 06K801 (2016).

[129] P. Binková, *Industrial Applications of Optical Nanoantennas*, (Bachelor's thesis). Brno University of Technology, Brno (2018).

[130] J. Babocký, *Shape Library for KLayout GDSII Editor*, (2018).

[131] International Organization for Standardization, *ISO/IEC 21778:2017 Information Technology – The JSON Data Interchange Syntax*, (2017).

[132] W.Y. Chen, C.H. Lin, and W.T. Chen, Plasmonic Phase Transition and Phase Retardation: Essential Optical Characteristics of Localized Surface Plasmon Resonance, *Nanoscale* **5**(20), 9950-9956 (2013).

[133] R.A. Deshpande, I.M. Akhmedzhanov, D.V. Baranov, E.M. Zolotov, and S.I. Bozhevolnyi, Rapid Characterization of Metasurface Unit Cells Using Scanning Differential Heterodyne Microscopy, In 2018 12th International Congress on Artificial Materials for Novel Wave Phenomena (Metamaterials) (IEEE, Espoo, 2018).

[134] T. Neuman, P. Alonso-González, A. Garcia-Etxarri, M. Schnell, R. Hillenbrand, and J. Aizpurua, Mapping the near Fields of Plasmonic Nanoantennas by Scattering-Type Scanning near-Field Optical Microscopy: Mapping the near Fields of Plasmonic Nanoantennas, *Laser & Photonics Reviews* **9**(6), 637-649 (2015).

[135] S.D. Gennaro, Y. Sonnefraud, N. Verellen, P. Van Dorpe, V.V. Moshchalkov, S.A. Maier, and R.F. Oulton, Spectral Interferometric Microscopy Reveals Absorption by Individual Optical Nanoantennas from Extinction Phase, *Nature Communications* **5**(1), 3748 (2014).

[136] J. Babocký, A. Křížová, L. Štrbková, L. Kejík, F. Ligmajer, M. Hrtoň, P. Dvořák, M. Týč, J. Čolláková, V. Křápek *et al.*, Quantitative 3D Phase Imaging of Plasmonic Metasurfaces, *ACS Photonics* **4**(6), 1389-1397 (2017).

[137] TESCAN Brno, s.r.o., *Q-PHASE: Quantitative Label-Free Imaging Cytometry*, (2017).

[138] A. Faßbender, J. Babocký, P. Dvořák, V. Křápek, and S. Linden, Invited Article: Direct Phase Mapping of Broadband Laguerre-Gaussian Metasurfaces, *APL Photonics* **3**(11), 110803 (2018).

[139] S. Pancharatnam, Generalized Theory of Interference, and Its Applications: Part I. Coherent Pencils, *Proceedings of the Indian Academy of Sciences - Section A* **44**(5), 247-262 (1956).

[140] M.V. Berry, Quantal Phase Factors Accompanying Adiabatic Changes, *Proceedings of the Royal Society A: Mathematical, Physical and Engineering Sciences* **392**(1802), 45-57 (1984).

[141] P. Bouchal, P. Dvořák, J. Babocký, Z. Bouchal, F. Ligmajer, M. Hrtoň, V. Křápek, A. Fabender, S. Linden, R. Chmelík *et al.*, High-Resolution Quantitative Phase Imaging of Plasmonic Metasurfaces with Sensitivity down to a Single Nanoantenna, *Nano Letters* **19**(2), 1242-1250 (2019).

[142] P. Bouchal, L. Štrbková, Z. Dostál, R. Chmelík, and Z. Bouchal, Geometric-Phase Microscopy for Quantitative Phase Imaging of Isotropic, Birefringent and Space-Variant Polarization Samples, *Scientific Reports* **9**(1), 3608 (2019).

List of publications

This thesis is based on the following publications

- Babocký, J.; Dvořák, P.; Ligmajer, F.; Hrtoň, M.; Šikola, T.; Bok, J.; Fiala, J. Patterning Large Area Plasmonic Nanostructures on Nonconductive Substrates Using Variable Pressure Electron Beam Lithography. *Journal of Vacuum Science & Technology B* 2016, 34 (6), 06K801. https://doi.org/10.1116/1.4966959.

- Babocký, J.; Křížová, A.; Štrbková, L.; Kejík, L.; Ligmajer, F.; Hrtoň, M.; Dvořák, P.; Týč, M.; Čolláková, J.; Křápek, V.; Kalousek, R.; Chmelík, R.; Šikola, T. Quantitative 3D Phase Imaging of Plasmonic Metasurfaces. *ACS Photonics* 2017, 4 (6), 1389–1397. https://doi.org/10.1021/acsphotonics.7b00022.

- Faßbender, A.; Babocký, J.; Dvořák, P.; Křápek, V.; Linden, S. Invited Article: Direct Phase Mapping of Broadband Laguerre-Gaussian Metasurfaces. *APL Photonics* 2018, 3 (11), 110803. https://doi.org/10.1063/1.5049368.

- Bouchal, P.; Dvořák, P.; Babocký, J.; Bouchal, Z.; Ligmajer, F.; Hrtoň, M.; Křápek, V.; Faßbender, A.; Linden, S.; Chmelík, R.; Šikola, T. High-Resolution Quantitative Phase Imaging of Plasmonic Metasurfaces with Sensitivity down to a Single Nanoantenna. *Nano Lett.* 2019, 19 (2), 1242–1250. https://doi.org/10.1021/acs.nanolett.8b04776.